INVESTIGATIONS OF ELECTROMAGNETIC METHODS APPLIED TO THE IN-RIVER AND NEAR-RIVER ENVIRONMENT ALONG THE MURRAY RIVER, AUSTRALIA

Michael A. Hatch

Geology and Geophysics, School of Earth and Environmental Sciences
University of Adelaide, Adelaide, SA 5005 Australia

This thesis submitted in fulfilment of the requirements for the
Doctor of Philosophy in the Faculty of Sciences

March 2011

TABLE OF CONTENTS

LIST OF FIGURES 4
LIST OF TABLES 11
ABSTRACT 12
DECLARATION 14
ACKNOWLEDGEMENTS 15
1 INTRODUCTION 17
1.1 Thesis Development and Motivation 17
1.2 Overview 18
2 A COMPARATIVE STUDY OF IN-RIVER GEOPHYSICAL TECHNIQUES FOR DEFINING VARIATIONS IN RIVERBED SALT LOAD AS AN AID TO MANAGING RIVER SALINISATION 24
2.1 Summary 24
2.2 Introduction 25
2.3 Study area and hydrogeology 26
2.4 Methods 29
2.4.1 In-river TEM: NanoTEM 30
2.4.2 In-river resistivity: Blue Eel 31
2.4.3 Airborne electromagnetics: RESOLVE FDHEM 33
2.4.4 In-stream coring 34
2.5 Results 35
2.5.1 River conditions 35
2.5.2 Conductivity-depth sections and borehole data 35
2.5.3 Borehole data 39
2.6 Comparisons 42
2.6.1 Conductivity-depth section comparison 42
2.6.2 Shallow data comparison 43
2.6.3 Shallow sediment plot comparison 44
2.6.4 Comparison with river EC measurements 45
2.7 Discussion 47
2.7.1 System resolution 47
2.8 Conclusions 49

3 THE IMPORTANCE OF THE LOSS TANGENT AND WAVENUMBER: IMPLICATIONS FOR VELOCITY AND SKIN DEPTH OF LOW-FREQUENCY GPR AND HIGH-FREQUENCY EMI SURVEYS 54
3.1 Summary 54
3.2 Introduction 54
3.3 Theoretical background 57
3.3.1 Dispersion considerations 59
3.4 Theoretical implications 60
3.4.1 Bounds: Quasi-static, low-loss and the transition band 60
3.4.2 Transition band behaviour 67
3.5 Results 68
3.5.1 GPR: Phase velocity 68
3.5.2 EMI: Skin depth and phase velocity 70
3.5.3 Field example 70
3.6 Conclusions 73
4 COMBINED PROCESSING AND INTERPRETATION OF GROUND PENETRATING RADAR AND HIGH-RESOLUTION TIME DOMAIN ELECTROMAGNETICS IN A CONDUCTIVE SETTING 77
4.1 Summary 77
4.2 Introduction 78
4.3 Study area 78
4.4 Geophysical data acquisition and processing 79
4.4.1 Time domain EM: NanoTEM 79
4.4.2 Ground penetrating radar: GPR 83
4.5 Discussion 88
4.5.1 Comparison of low-loss processing with full-solution processing 91
4.5.2 Analysis of the conductivity properties of the GPR-determined surface layer .. 93
4.5.3 Varying permittivity 97
4.5.4 Using simpler estimates of conductivity distribution 99
4.6 Conclusions 105
5 INTERPRETATION OF AIRBORNE AND GROUND GEOPHYSICAL SYSTEMS OVER CONDUCTIVE GROUND 110
5.1 Summary 110
5.2 Introduction 110

5.3 Geological setting 112
5.4 Geophysical data acquisition and processing 113
5.4.1 Airborne electromagnetics 113
5.4.2 Towed TEM....114
5.4.3 Ground penetrating radar....115
5.5 Results 117
5.6 Discussion 133
5.6.1 Expected EMI response....133
5.6.2 Expected GPR response....135
5.6.3 Interpretation....136
5.7 Conclusions 138
6 THESIS SUMMARY AND CONCLUSIONS....140
6.1 Review by chapter 140
6.2 Overall 143
6.3 Further research 146
APPENDIX A: DISPERSION REVISITED 149
REFERENCES 162

LIST OF FIGURES

Figure 2.1. Groundwater salinity of the Lower Murray Basin, south-central Australia. The location of the study area is indicated with a red polygon. The TDS of seawater is approximately 35,000 mg/L (Murray Darling Basin Commission, 2002). 27

Figure 2.2. Schematic representation of the hydrogeology of the study area. Vertical wavy blue arrows indicate recharge to groundwater systems, primarily linked to irrigation. Horizontal blue arrows indicate regional groundwater flow directions..... 27

Figure 2.3. Map indicating the reach of the river surveyed with the various techniques. The yellow line indicates the location of depth sections shown in Figure 2.6. The depth sections shown in Figure 2.7 are for the reach marked by the red line. 30

Figure 2.4. Schematic diagram of the in-river TEM rig. 31

Figure 2.5. Schematic diagram of the in-river DC resistivity rig. 33

Figure 2.6. Depth sections of complete data runs: (a) interpolated lithology; (b) borehole TDS converted to EC; (c) inverted in-river TEM data; (d) inverted in-river resistivity data; (e) inverted FDHEM data. The vertical axis is depth below river surface in metres. The horizontal axis is distance along river in metres. Water depth is indicated on the in-river TEM and in-river resistivity sections (c and d) with a grey line. Water depth as measured during the in-river TEM survey is superimposed in black for comparison purposes on (e) (FDHEM data set). 37

Figure 2.7. Depth sections of the smaller comparison stretch of the river: (a) inverted in-river TEM data; (b) inverted in-river resistivity data; (c) inverted FDHEM data. The vertical axis is depth below river surface in metres. The horizontal axis is distance along river in metres. Water depth (as measured at the time of each survey) is indicated on the in-river TEM and in-river resistivity sections (a, b) with a grey line. Water depth as measured during in-river TEM survey is superimposed in black for comparison purposes on (c) (FDHEM data set). 38

Figure 2.8. Contoured river-bottom data. These data were taken from layer immediately below the measured water depth from each inverted data set: (a) in-river resistivity; (b) in-river TEM; (c) FDHEM. The 6.6- to 9.3-m depth layer was used for the FDHEM. The main underlying image is an air photo image showing regional land use and patterns. The intermediate background image is the 6.62- to 9.28-m depth slice taken from the 2006 regional FDHEM survey collected in this area. 40

Figure 2.9. Comparison of geophysical results with drilling logs for two boreholes: (a) results for borehole Sun06RC; (b) results for borehole Sun09RC. Logged lithology and downhole

sampled TDS results (converted to EC) have been plotted against results from geophysical techniques. The vertical axis is depth below river bottom in metres. 41

Figure 2.10. Comparison of geophysical results with ROR EC measurements: (a) ROR compared with in-river DC resistivity; (b) ROR compared with in-river TEM; (c) ROR compared with FDHEM. Results from each geophysical survey are shown in blue; 2001 ROR EC results are shown in red. The horizontal axis is distance along the river and river km. The right vertical axis is change in river EC in mS/m. The left vertical axis is conductivity in mS/m. 46

Figure 3.1. Comparison of the ratio of the attenuation term and the phase term of the wavenumber to loss tangent. When $\alpha/\beta \rightarrow 1$, $\alpha \rightarrow \beta$ and conditions are dominated by conduction currents. When $\alpha/\beta \rightarrow 0$, $\alpha \rightarrow 0$ and conditions are dominated by displacement currents. The darker shaded area on the left side of the plot indicates the combinations of conductivity, frequency and permittivity for which the loss tangent is <0.01, and conditions are predominantly low-loss (as defined in the text). The lightly shaded area on the right side of the plot indicates the combinations of conductivity, frequency and permittivity for which the loss tangent is >216 and conditions are predominantly quasi-static (as defined in the text). 62

Figure 3.2. Comparison of approximate low-loss and quasi-static velocities (Equations 3.4 and 3.6) to true values (Equation 3.9). Loss tangent increases with decreasing frequency and dielectric permittivity and with increasing conductivity. Parameter ranges where low-loss estimate error is less than 5% are highlighted in dark grey. Parameter ranges where quasi-static estimate error is less than 5% are highlighted in light grey. The boxed, cross hatched area shows the range of parameters where approximate solutions deviate from exact solutions by 0.5% or more. The numbers at the top of the plot define zones where low-loss conditions prevail, where quasi-static conditions prevail, and where transition band conditions prevail, as defined in the text. 63

Figure 3.3. Comparison of approximate low-loss and quasi-static velocities (Equations 3.4 and 3.6) to true values (Equation 3.9). a) permittivity is fixed at 5, and frequency is fixed at 25 MHz. Conductivity is allowed to vary. b) permittivity is fixed at 5, and conductivity is fixed at 10mS/m (100 ohm-m). Frequency is allowed to vary. c) conductivity is fixed at 10 mS/m (100 ohm-m), and frequency is fixed at 25 MHz. Permittivity is allowed to vary. The black arrows on each plot show the direction in which the loss tangent increases. Parameter ranges where low-loss estimate error is less than 5% are highlighted in dark grey. Parameter ranges where quasi-static estimate error is less than 5% are highlighted in light grey. Cross hatched area shows range of parameters where approximate solutions deviate from exact

solutions by 0.5% or more. The numbers at the top of each plot define zones where low-loss conditions prevail, where quasi-static conditions prevail, and where transition band conditions prevail, as defined in the text. 65
Figure 3.4. Loss tangent calculated for conductivities ranging from 0.001 mS/m (1M ohm-m) to 1000 mS/m (1 ohm-m) and frequencies ranging from 1000 Hz to 1000 MHz. In a) dielectric permittivity is set to 5, and in b) dielectric permittivity is set to 40. The lightly shaded area at the top of each plot indicates the combinations of conductivity and frequency for which the loss tangent is >103 and conditions are predominantly quasi-static. The darker shaded area at the bottom indicates the combinations of conductivity and frequency for which the loss tangent is <0.2 and conditions are predominantly low-loss. The unshaded zone in the centre of each plot is the transition band. The sloped solid lines indicate conductivities and frequencies for which the loss tangent =1. The heavy vertical lines indicate test conditions described in text (i.e. f=25 MHz, conductivities range from 10 to 1000 mS/m). 66
Figure 3.5. a) relative signal strength after one wavelength and wavelengths per skin depth plotted against loss tangent. b) relative signal strength after one wavelength and wavelengths/skin depth plotted against conductivity. Permittivity = 5, f = 25 MHz. c) relative signal strength after one wavelength and wavelengths/skin depth plotted against conductivity. Permittivity = 40, f = 25 MHz. Shading scheme for all plots is the same as in Figure 3.2. 69
Figure 3.6. Example depth sections of GPR and towed-TEM over 2 km stretch. a) GPR data processed using low-loss assumptions and permittivity = 11. b) GPR data processed using velocities calculated based on the conductivity information from the TEM data set. c) inverted TEM data set. The vertical axis is elevation in metres. The horizontal axis is distance along profile in metres. Highly conductive features in TEM section and breaks in GPR data at approximately stations 10600, 10840 and 11090 are bridges (i.e. cultural features). Basic hydrogeological interpretation is highlighted on the TEM section. The location of the regionally determined water table is indicated with a grey line on the TEM section..... 72
Figure 4.1. Location of the study area in southeastern Australia highlighted on the location map with a red polygon. The Murray River is the boundary between New South Wales and Victoria, as well as for the offset section of South Australia. The areal extent of the floodplains around the Murray is highlighted with green stippling. The underlying image is of regional groundwater salinity. The TDS of seawater is approximately 35,000mg/L (Murray Darling Basin Commission, 2002). 80
Figure 4.2. Equipment used for ground component of this study. a) schematic diagram of towed TEM system; b) photo of GPR rig on site. 80

Figure 4.3. Comparison between conductivity depth sections for: a) discrete; and b) smooth-model inversion results from the TEM. The vertical axis is elevation in metres. The horizontal axis is distance along profile in metres. 82
Figure 4.4. Schematic diagram of near-surface interactions for GPR system where the receiving and the transmitting antennae are separated by 4 m. For a reflector at 0.5 m depth, the signal actually travels 4.12 m from the surface to the reflector and back to the surface (dashed line). This arrives only 2.4 ns later than the direct wave, making resolution of shallow features difficult. 87
Figure 4.5. Geometric corrections for deeper layers are complicated by differences in layer velocity refracting the travel path. The ray paths need to be approximated using Snell's law. 87
Figure 4.6. Calculating surface layer conductivity from GPR. The time from transmitter turn-on to the arrival of the air-wave is indicated with dotted stippling. The air-wave is indicated with cross-hatching. The conductivity of the top layer from the TEM is 314 mS/m (3.2 ohm-m). The calculated velocity is 2.75×10^7 m/s (based on Equation 4.3) so the ground-wave arrival should occur at 145 ns. Setting the conductivity to approximately 60 mS/m (17 ohm-m) for this layer sets the start time for the ground-wave correctly. 90
Figure 4.7. a) GPR data processed using low-loss assumptions and permittivity = 11; b) GPR data processed using velocities calculated based on the conductivity information from the TEM data set; c) inverted TEM data set. The vertical axis is elevation in metres. The horizontal axis is distance along profile in metres. Highly conductive features in the TEM section and breaks in the GPR data at approximately stations 10600, 10840 and 11190 are bridges (i.e. cultural features). Basic hydrogeological interpretation is highlighted on the TEM section. The location of the regionally determined water table is indicated with a grey line on the TEM section. 92
Figure 4.8. Depth sections of towed-TEM and GPR for the Lindsay River data set from km 8 to 12. a) GPR data with top of 1st major reflector highlighted in black; b) TEM data inverted using the discrete-layer inversion, with the top layer information derived from the GPR data; c) TEM data inverted using the discrete-layer inversion; d) TEM data inverted using the smooth-model inversion. The vertical axis is elevation in metres. The horizontal axis is distance along profile in metres. Permittivity is set to 11. 94
Figure 4.9. Forward modelled (a) and inverted (b) TEM response for five scenarios. All models were run for a two-layer model, with the surface layer extending to a depth of 3 m and the bottom layer set to 1000 mS/m (1 ohm-m). Surface layer conductivities were set to 333

mS/m (3 ohm-m), 167 mS/m (6 ohm-m), 111 mS/m (9 ohm-m), 83 mS/m (12 ohm-m) and 67 mS/m (15 ohm-m). 96
Figure 4.10. Borehole conductivity log for Bore B7928, located at approximately station 3640 on the Lindsay River line, compared with TEM smooth-model and discrete-layer inversion results at that station. GPR-derived surface layer conductivity is shown also for comparison. Approximate depth to water table indicated with black triangle. 98
Figure 4.11. Comparison of GPR results when permittivity is varied for Lindsay River data set, km 8 to 12: a) permittivity is set to 3; and b) permittivity is set to 20. The vertical axis is elevation in metres. The horizontal axis is distance along profile in metres. 100
Figure 4.12. a) Phase velocity and b) loss tangent calculated for four conductivities, varying permittivity from 1 to 35. Low-loss conditions are highlighted in grey. 101
Figure 4.13. Comparison of TEM results when permittivity is varied for Lindsay River data set, km 8 to 12: a) inverted TEM data where the conductivity of the top layer is GPR-derived and the permittivity is set to 3; b) inverted TEM data where the conductivity of the top layer is GPR-derived and the permittivity is set to 20; and c) inverted TEM data without surface layer GPR. In all cases, the vertical axis is elevation in metres. The horizontal axis is distance along profile in metres. 102
Figure 4.14. Conductivity variation plotted against permittivity. Phase velocity is fixed at 5.34×10^7 m/s. 103
Figure 4.15. GPR depth sections for the Lindsay River data set from km 8 to 12 where the data were processed using three different methods to estimate conductivity conditions: a) GPR data processed using the full set of TEM data (same as Figure 4.8a); b) GPR data processed using averaged TEM data to simulate LIN-based terrain conductivity meter data; and c) GPR data processed using a single estimate (200 mS/m) for conductivity. In all cases permittivity was set to 11. Basic hydrogeological interpretation is highlighted on Figure 4.15a. 104
Figure 5.1. Groundwater salinity of the study area in south-central Australia, highlighted on the location map with a red polygon. RMC AEM data grid is shown in grey. The areal extent of the floodplains around the Murray are highlighted with green stippling. The Murray River is the boundary between New South Wales and Victoria, as well as for the offset section of South Australia. The TDS of seawater is approximately 35,000 mg/L (Murray Darling Basin Commission, 2002). 113
Figure 5.2. Equipment used for ground component of this study: a) schematic diagram of towed TEM system; and b) photo of GPR rig on site. 115

Figure 5.3. Detailed view of Lindsay Island transect. The underlying image is a false colour image showing regional land use and patterns. Line location is shown using 6-m depth slice of inverted TEM data. Distances along line and borehole locations are also shown. 118
Figure 5.4. Detailed view of Potterwalkagee Creek transect. The underlying image is a false colour image showing regional land use and patterns. Line location is shown using 6-m depth slice of inverted TEM data. Distances along line and borehole locations are also shown. 119
Figure 5.5. Detailed view of Walpolla Island transect. The underlying image is a false colour image showing regional land use and patterns. Line location is shown using 6-m depth slice of inverted TEM data. Distances along line and borehole locations are also shown. 120
Figure 5.6. Depth section comparison of GPR, towed TEM and FDHEM for entire Lindsay Island data set: (a) processed GPR data; (b) inverted, towed TEM data with top layer information supplied by GPR; (c) inverted towed TEM data; (d) inverted FDHEM data; and e) inverted FDHEM, showing approximately the top 60 m. The vertical axis is elevation in metres. The horizontal axis is distance along profile in metres. Regional water level is indicated on each section with a grey line. Flushed zones are identified on the GPR section. Basic hydrogeological interpretation is highlighted on the FDHEM section (d). Location of the top of the capillary fringe based on GPR information is indicated on the GPR section with a black line..... 122
Figure 5.7. Depth section comparison of GPR, towed TEM and FDHEM for Lindsay Island data set, from station 3200 to 4200: (a) processed GPR; (b) inverted TEM data with top layer information supplied by GPR; (c) inverted TEM data; and (d) inverted FDHEM data. The vertical axis is elevation in metres. The horizontal axis is distance along profile in metres. Regional water level is indicated on each section with a grey line. Bore logs are superimposed on all sections, with depth to watertable indicated with a blue line, and approximate top of the capillary fringe with a red line. Flushed zones are identified on the GPR section. Basic hydrogeological interpretation is highlighted on the FDHEM section. Location of the top of the capillary fringe based on GPR information is indicated on the GPR section with a black line..... 123
Figure 5.8. Depth section comparison of GPR, towed TEM and FDHEM for Lindsay Island data set, from 6340 to 7340: (a) processed GPR; (b) inverted TEM data with top layer information supplied by GPR; (c) inverted TEM data; and (d) inverted FDHEM data. The vertical axis is elevation in metres. The horizontal axis is distance along profile in metres. Regional water level is indicated on each section with a grey line. Bore logs are superimposed on all

sections, with depth to watertable indicated with a blue line, and approximate top of the capillary fringe with a red line. Flushed zones are identified on the GPR section. Basic hydrogeological interpretation is highlighted on the FDHEM section. Location of the top of the capillary fringe based on GPR information is indicated on the GPR section with a black line. 124

Figure 5.9. Depth section comparison of GPR, towed TEM and FDHEM for Lindsay Island data set, from 14800 to 15800: (a) processed GPR; (b) inverted TEM data with top layer information supplied by GPR; (c) inverted TEM data; and (d) inverted FDHEM data. The vertical axis is elevation in metres. The horizontal axis is distance along profile in metres. Regional water level is indicated on each section with a grey line. Simplified bore logs are superimposed on all sections, with depth to watertable indicated with a blue line, and approximate top of the capillary fringe with a red line. Flushed zones are identified on the GPR section. Basic hydrogeological interpretation is highlighted on the FDHEM section. Location of the top of the capillary fringe based on GPR information is indicated on the GPR section with a black line. 125

Figure 5.10. Depth section comparison of GPR, towed TEM and FDHEM for entire Potterwalkagee Creek data set: (a) processed GPR; (b) inverted TEM data with top layer information supplied by GPR; (c) inverted TEM data; and (d) inverted FDHEM data. The vertical axis is elevation in metres. The horizontal axis is distance along profile in metres. Regional water level is indicated on each section with a grey line. Simplified bore logs are superimposed on all sections, with depth to watertable indicated with a blue line, and approximate top of the capillary fringe with a red line. Flushed zones are identified on the GPR section. Basic hydrogeological interpretation is highlighted on the FDHEM section. Location of the top of the capillary fringe based on GPR information is indicated on the GPR section with a black line. 126

Figure 5.11. Comparison plot of GPR, towed TEM and FDHEM for entire Walpolla Island data set: (a) processed GPR; (b) inverted TEM data with top layer information supplied by GPR; (c) inverted TEM data; and (d) inverted FDHEM data. The vertical axis is elevation in metres. The horizontal axis is distance along profile in metres. Regional water level is indicated on the each section with a grey line. No bore logs were available for 4E-1or 4B-5, but groundwater depth and conductivity information was. This is superimposed on the sections at their approximate locations. The blue line on the 4B-5 marker indicates the water table location. Flushed zones are identified on the GPR section. Basic hydrogeological

interpretation is highlighted on the FDHEM section. Location of the top of the capillary fringe based on GPR information is indicated on the GPR section with a black line. 127
Figure 5.12. Detailed logs of bores presented in Figures 5.7 to 5.9. On each log, water table depth is indicated with a blue line. Where original bore logs supplied information about where moisture was encountered during drilling, this depth is indicated with a dashed red line. This depth is interpreted as the approximate depth to the top of the capillary fringe. The black line indicates the depth to the top of the capillary fringe, as interpreted from the GPR data. Note that the full log for B7928 extends to 50-m depth. 128
Figure 5.13. Borehole conductivity log for Bore B7928 located at approximately station 3700 on Lindsay River line compared with the TEM smooth-model inversion sounding and the FDHEM smooth-model inversion for the nearest station (<30 m). The TEM conductivities diverge significantly from the borehole conductivities at depth. Approximate depth to water table indicated with black triangle. 130
Figure 5.14. Image comparing inverted regional FDHEM data set, depth slice at 5- to 10-m depth, with 6-m depth slice of ground TEM data set as overlay. 131
Figure 5.15. Image comparing map of derived tree health with 6-m depth slice of ground TEM data set as overlay. 132
Figure 5.16. Image comparing derived map of flush zone location and thickness based on FDHEM inverted data set with 6 m depth slice of ground TEM data set as overlay. Location along TEM data track of flush zones interpreted from ground TEM and GPR have been super-imposed. 134

LIST OF TABLES

Table 2.1. Comparison of shallowest level conductivity and river EC at recording location 414204. 29
Table 2.2. River level at recording location 413002. 36
Table 3.1. Permittivity effects on RMT data. 70

ABSTRACT

In the last decade more than 2500 km of the Murray River in southeastern Australia and its surrounding floodplains have been surveyed using a variety of geophysical techniques to assess the environmental impact of changing salinity conditions along the river. These have included a combination of ground-based and airborne electromagnetic (EM) techniques. Along the Murray River, particularly in the lower reaches, the near-surface conductivity ranges from being moderately resistive to highly conductive, with groundwater conductivities approaching that of seawater in many areas. Such conditions present challenges for the application of most EM techniques, particularly as the signal attenuates rapidly resulting in little signal penetration. For all EM and DC-resistivity techniques, careful selection of frequency range and/or system geometry is therefore necessary to collect information over depth ranges of interest. An understanding of tradeoffs between frequency range and/or system geometry, resolution, and penetration depth is arguably critical to technique selection at the outset of the survey, and to the application of appropriate data processing and interpretation procedures post-survey. This thesis examines and evaluates a number of geophysical techniques for their suitability in characterising the shallow subsurface beneath and adjacent to the Murray River.

Results for three inductively and galvanically based geophysical techniques used to collect data in the in-river setting are compared over the same stretch of river. Two are variations on ground-based systems, adapted to collect data nearly continuously while being towed behind a boat. These are a time domain EM (TEM) system and a DC-resistivity system. The third is a high-resolution, helicopter-based, airborne EM (AEM) system. In this study, the AEM system was demonstrated to provide a similar horizontal resolution as that provided by river-based systems. In addition, although the river-based techniques were able to image to depths of approximately 20 m, the AEM system was able to image to approximately 25 m depth in highly conductive areas, and to approximately 60 m depth in more resistive areas. The AEM system was also able to collect data over floodplains adjacent to the river, providing contextual information where needed.

A new methodology for processing ground penetrating radar (GPR) data collected over conductive ground is developed. As part of this development, the transition band in the EM spectrum is defined, using the loss tangent to define parameter boundaries. In the transition band (ranging from approximately 110 kHz to 57 MHz for typical soil conditions), both conductive and displacement currents are important as conduction mechanisms, and need to be accounted for when calculating phase velocity and skin depth. Data from three 25 MHz GPR traverses, varying in length from less than 3 km to more than 16 km, were collected over conductive

floodplains. These data are processed using this new methodology, and interpreted in conjunction with ground TEM data. After processing, the GPR is able to provide useful information about the depth to the top of the capillary fringe, as well as the location of near-surface flush zones. This information correlates well with other data sets collected in conjunction with the GPR.

DECLARATION

This work contains no material which has been accepted for the award of any other degree or diploma in any university or other tertiary institution to Michael A. Hatch and, to the best of my knowledge and belief, contains no material previously published or written by another person, except where due reference has been made in the text.

I give consent to this copy of my thesis when deposited in the University Library, being made available for loan and photocopying, subject to the provisions of the Copyright Act 1968.

The author acknowledges that copyright of published works contained within this thesis (as listed below) resides with the copyright holder(s) of those works. I also give permission for the digital version of my thesis to be made available on the web, via the University's digital research repository, the Library catalogue, and also through web search engines, unless permission has been granted by the University to restrict access for a period of time.

List of publications

Chapter 2 has been published as: Hatch, M., Munday, T., Heinson, G., 2010, A comparative study of "in-river" geophysical techniques for defining variations in riverbed salt load as an aid to managing river salinization, Geophysics, 75, 4, pages WA 135-147.

ACKNOWLEDGEMENTS

Thank you to my wife and chief-editor, Karin, who has always inspired me in my continuing education. I could not have done this without you.

Thank you to my supervisors Graham Heinson and Tim Munday, who were kind enough to take me on and give me free rein (sometimes to their frustration).

Thank you:
Volmer Behrens and Andrew Fitzpatrick. You were collaborators on a number of the projects that were started at the beginning of this PhD. More of that work needs to be written up.

To my colleagues at the University of Adelaide. For some great talks, sometimes even about science. Stephan Thiel, Rachel Maier, Graham Baines, Jared Peacock, and Robert Dart.

To the people that I worked with at Geoscience Australia. I enjoyed my chance to work with you in Canberra, and appreciate the information and advice that you have provided since. Ken Lawrie, Ross Brodie, Jon Clarke, K. P. Tan, and John Wilford.

Kelly Keates for your support for all of these years.

Scott MacInnes for challenging me.

Ken Zonge for starting me down the geophysical road.

Andrew Telfer and Barry Porter for your enthusiasm for the dark art of geophysics as applied to your river.

Esben Auken for your support and software.

Gary Fallon and Terry Ritchie of GRS for giving me such a great deal for the use of their NanoTEM system.

Brian Barrett, David Allen, and Phil Mill for providing support during various rounds of this research.

Sam (with help from our dogs Zero and Libby) for trying to get me fit.

Thank you to all of the groups that have provided financial support for these projects. These include the Australian government for an APA scholarship, the South Australian Department for Water, the Murray-Darling Basin Authority, the Lower Murray Darling Catchment Management Authority, Goulburn-Murray Water, and the New South Wales Department of Natural Resources.

There are many others who supported me and my work at various times. I will never remember everyone. I nevertheless thank you as well.

1 INTRODUCTION

1.1 Thesis Development and Motivation

The main aim of this research was to investigate the use of near-surface geophysical techniques to characterise the electrical properties of the sediments under the Murray River and its floodplains, primarily to help understand their value for informing the hydrogeology and therefore floodplain and river management of the region. More specifically, the intent of the research was to assess several different geophysical methods for improving knowledge of surface water - groundwater interactions and spatial patterns in groundwater salinity in these environments. All of the work presented here was done with the intention that the methods and approaches would be extended to other river systems, both in Australia and globally.

The research has posed a number of questions, many of which are fundamental to most sub-disciplines of applied geophysics. These questions include:

1) Are the data being processed and modelled appropriately so that depths to features are interpreted correctly?
2) Is the information provided accurate, or are the processing approximations in highly conductive conditions masking the true response?
3) What is the geological and/or hydrogeological significance of the information provided by the geophysical survey?
4) To what depth does the technique provide useful information? Not only is this a question of how deep the technique can "see", but in defining the shallow limit as well. Additionally, the vertical resolution of the system is also of interest.
5) How large is the lateral footprint of the system being evaluated?

For the Murray River and adjacent floodplains, geophysical methods need to address the following additional, specific hydrogeological issues:

i. Is the technique able to help workers understand the connections between surface water and groundwater?
ii. Is the technique able to locate zones of relatively fresher water, both perched and flushed, within the regionally saline groundwater?
iii. Is the technique both precise and accurate enough that data sets collected at different times may be compared, thereby allowing, for example, investigators to examine the effectiveness and efficiency of engineering schemes designed to freshen aquifers in the vicinity of the river and/or floodplain?

A related aim in this research was to examine electromagnetic (EM) behaviour in the "transition band" of the EM spectrum. The transition band is defined here as the frequency band in the EM spectrum between the low frequency end, where conductivity currents dominate, and EM response is measured via electromagnetic induction (EMI), and the high frequency end, where displacement currents dominate, and EM signal propagates as waves, as with ground penetrating radar (GPR).

These two aims were linked when Geoscience Australia, with funding from the River Murray Corridor AEM project (Lawrie et al., 2008), provided the opportunity to collect high-resolution TEM and GPR data over salt-affected floodplains of the Murray River, east of Mildura, Victoria. Three traverses of TEM and 25 MHz GPR data were collected in early 2008. The intent was to process the TEM and the GPR data sets separately, ultimately comparing the output scale of both with the AEM data set collected over the same area in 2007. As the GPR data were not collected under low-loss conditions, the standard phase velocity equation, based on the low-loss approximation, was not appropriate to convert GPR two-way travel time data to true depths. A new methodology was needed to process these data, which was developed as part of this thesis.

1.2 Overview

This thesis consists of six chapters. The first is this introduction, and the last is a summary. Each of the middle four chapters has been written as a stand-alone article, that has either been published, submitted or is intended for publication in peer-reviewed journals. A review of all of the chapters follows.

Chapter 1: Introduction

Chapter 1 outlines the motivation for this research, and reviews the thesis organisation.

Chapter 2: A comparative study of in-river geophysical techniques for defining variations in riverbed salt load as an aid to managing river salinisation

Published in Geophysics (Hatch et al., 2010), Chapter 2 is a comparison of electrical geophysical techniques, each run over the same test area on the Murray River. Over the last few years a number of electrical geophysical techniques have been developed to characterise conductivity structure under bodies of water (Butler, 2009). These techniques have been run at several locations around the world, but have not been rigorously compared. This chapter compares results collected over a stretch of the Murray River upstream from Mildura, Victoria, for

an in-stream TEM system, an in-stream DC-resistivity system, and a helicopter-based AEM system. Vertical and horizontal resolution, depth of investigation, and lateral footprint are examined for each system. These are evaluated both from theoretical considerations and model comparisons, and the results are correlated with available borehole and river salinity data.

Chapter 3: The importance of the loss tangent and wavenumber: Implications for velocity and skin depth of low-frequency GPR and high-frequency EMI surveys

In Chapter 3 the "transition band" is defined. This chapter highlights the loss tangent as the primary tool to define whether a given EM data set has been collected under strictly quasi-static conditions where conduction currents predominate; strictly low-loss conditions where displacement currents predominate; or in the transition band where neither dominates, but both have influence on how the fields behave. Nearly all GPR data are collected at frequencies greater than 10 MHz where it is usually assumed that conductive currents are much smaller than displacement currents, and therefore the effects of conductive currents may be ignored in the relevant phase velocity equations that are used to convert GPR two-way travel time data to true depths, i.e. phase velocity based on the low-loss approximation. In this chapter it is shown that for an average "soil" (Reynolds, 1997), where the relative dielectric permittivity is 16 and the conductivity is 10 mS/m (100 ohm-m), the transition band ranges from approximately 110 kHz to 57 MHz. GPR data collected at less than 57 MHz are likely to be in the transition band.

Annan (1996) states that when the loss tangent is greater than 1 conditions tend to be quasi-static, and that when the loss tangent is less than 1 conditions tend to be low-loss, with the loss tangent equal to 1 marking the transition from one set of conditions to the other. This chapter proposes that in the transition band, neither dominates, and both conduction and displacement currents have significant influence over EM behaviour. The transition band is then defined, based on calculation errors for phase velocity. For the high-frequency, displacement-current dominant case, velocities calculated over a range of conditions based on the full-solution equation are compared against those based on the low-loss phase velocity equation (Ward and Hohmann, 1991; Annan, 2005a). The same is done for the low-frequency, conduction-current dominant case, where the full-solution phase velocity is compared with the quasi-static phase velocity (Ward and Hohmann, 1991).

For data sets collected under transition band conditions Stratton's (1941) solution of the wavenumber equation is proposed as the basis for calculating skin depth, phase velocity and other important parameters used to characterise EM data. The full solution is used, rather than

basing skin depth on the quasi-static version of the wavenumber equation or basing GPR phase velocity on the low-loss version of the wavenumber equation.

Chapter 4: Combined processing and interpretation of ground penetrating radar and high-resolution time domain electromagnetics in a conductive setting

Chapter 4 outlines a procedure for processing GPR data collected under transition band conditions, based on the full solution to the wavenumber equation set out in Chapter 3. As there is a conductivity term in this equation, conductivity information about the study area must be known and included. Most of this chapter concentrates on using layer-conductivities from the inverted TEM data sets that were collected with the GPR data sets as the basis for calculating phase velocities for each GPR sounding. These phase velocities are then used to convert GPR two-way travel time data to true depths. Two methods are also outlined and analysed based on simpler approaches to estimate the conductivity structure of the ground.

As an extension of the GPR processing using inverted TEM conductivities to calculate phase velocity, a method for estimating surface layer conductivity from the GPR data alone is derived. Interestingly, the GPR-derived surface layer conductivities are more resistive than the TEM-derived surface layer conductivities. This discrepancy is explored in this chapter, as it has direct effect on the determination of the thickness of the surface layer, which affects the GPR processing results.

In Chapter 4 it is also recognised that the system geometry, specifically the separation between the transmitter and the receiver, as a significant source of depth conversion error if not accounted for when processing these GPR data.

Chapter 5: Interpretation of airborne and ground geophysical systems over conductive ground

In chapter 5 the processing scheme outlined in Chapter 4 is used to process three GPR traverses collected as part of the River Murray Corridor AEM project that was the original motivation for this work. The processed GPR data are presented, as sections, with inversion results from TEM and AEM data collected over the same traverses. These three data sets are compared against each other, to analyse differences in scale and depth of penetration between the ground-based data sets and the AEM. All three data sets are then interpreted together.

Chapter 6: Thesis summary and conclusions

Chapter 6 is a review chapter, including a short synthesis of the major outcomes of this research. It concludes by suggesting a number of questions that arise from this thesis that may be of interest to researchers in the future.

Chapter 2

A comparative study of in-river geophysical techniques for defining variations in riverbed salt load as an aid to managing river salinisation

M. A. Hatch, T. Munday, G. Heinson

Geology and Geophysics, School of Earth and Environmental Sciences
University of Adelaide, Adelaide, SA 5005 Australia

Geophysics 2010: accepted paper

STATEMENT OF AUTHORSHIP

A comparative study of in-river geophysical techniques for defining variations in riverbed salt load as an aid to managing river salinisation

Geophysics 2010: accepted paper

Hatch, M. A. (Candidate)
Sourced and interpreted data, wrote manuscript and acted as corresponding author.

I hereby certify that the statement of contribution is accurate

Signed . .....*Date* 27 March 2011

Munday T.
Supervised development of work, helped in data interpretation and manuscript evaluation

I hereby certify that the statement of contribution is accurate and I give permission for the inclusion of the paper in the thesis

Signed ....*Date* 27th March 2011

Heinson. G.
Provided critical evaluation

I hereby certify that the statement of contribution is accurate and I give permission for the inclusion of the paper in the thesis

Signed ... .*Date* 28/3/2011

2 A COMPARATIVE STUDY OF IN-RIVER GEOPHYSICAL TECHNIQUES FOR DEFINING VARIATIONS IN RIVERBED SALT LOAD AS AN AID TO MANAGING RIVER SALINISATION

This chapter is published as: Hatch, M., Munday, T., Heinson, G., 2010, A comparative study of "in-river" geophysical techniques for defining variations in riverbed salt load as an aid to managing river salinization, Geophysics, 75, 4, pages WA 135-147.

2.1 Summary

Increased interest in the character of sediments at the base of waterways, for managing river salinisation, has led to the application of several geophysical techniques for collecting information from this zone. These in-stream methods are based on established ground and airborne electrical and electromagnetic technologies including: towed transient-electromagnetic; towed direct-current resistivity array systems; and frequency-domain helicopter electromagnetic systems. Although these systems are individually successful, a systematic examination of their relative effectiveness for identifying variations in substrate conductivity for a common stretch of a river remains lacking. We have compared results obtained from data collected using three in-stream geophysical techniques for a common stretch of the Murray River in southeastern Australia. The Murray River is an important water resource for drinking and agricultural purposes. Data from these surveys were acquired to locate areas of significant salt water accession to the Murray from a saline regional groundwater system that discharges into it. The three methods indirectly inform on those reaches that most likely contribute to higher salt loads in the river, and they do this through the identification of a conductive substrate (a gaining reach). For a 25-km stretch of the river the methods identified similar variations in the conductivity structure of sediment substrate, although differences were observed in the modelled response relating to intrinsic differences between each system, including the sampling interval and resolution. The helicopter electromagnetic (EM) system is capable of acquiring hundreds of kilometres of data in a day, under any river flow condition, from near the river surface to depths in excess of 60 m. The two other techniques require safe river flow conditions for acquisition, with as much as 50 river km of data per day possible. The ground-based methods had enhanced lateral and vertical resolving capabilities relative to the helicopter EM system, but their depth of investigation was less (usually only 20 m).

2.2 Introduction

Many studies have examined the application of hydrogeophysical methods to characterise the sedimentary substrate of river and/or lake sediments. Auken et al. (2006) provide an overview of recent developments in near-surface geophysical techniques, and Butler (2009) examines trends in the development and application of waterborne electrical and electromagnetic methods for the subbottom mapping of resistivity/conductivity. Goldman et al. (1995; 2004) and Hurwitz et al. (1999) discuss the application of transient electromagnetic (TEM) methods to the detection of shallow brines under the Sea of Galilee in Israel. Barrett et al. (2005) and Telfer et al. (2005) report on the development of a continuously sampling shallow TEM system used on the Murray River in South Australia.

Snyder et al. (2002), Allen and Merrick (2003), and Kelly et al. (2009) report on the development of similar continuously sampling resistivity profiling systems to characterise the conductivity of riverbeds sediment systems in both the United States and Australia. Amidu and Dunbar (2007) report on the development of the same sort of system to characterise salinity variation in the water column of a reservoir. Paine et al. (2006; 2009), and Fitzpatrick et al. (2007b) describe the use of helicopter electromagnetic (EM) systems to identify the location of saline groundwater systems discharging through riverbed sediments into river systems. The former describes results from a study along the Colorado River in the United States, while the latter presents data and results from a study along the Murray River in Australia.

Although these electrical and electromagnetic methods have been deployed with varying degrees of success, there has been no systematic assessment of their relative merits for understanding substrate properties. In part this reflects the absence of examples where surveys with different geophysical systems have been conducted for a common stretch of a river or body of water. In the mapping of substrate salinity and for understanding the links between surface water and groundwater, the absence of comparative studies has made it more difficult to make an informed decision on the best approach to adopt, or to understand, in advance, of the possible outcomes should a particular system and procedure be deployed.

This study attempts to address this deficiency, through the direct comparison of the results for a common stretch of river from commonly used geophysical techniques: specifically two ground-based systems, an in-river resistivity technique and an in-river TEM technique, along with a frequency-domain helicopter electromagnetic (FDHEM) system. The techniques compared in this study were designed for near-surface investigation. They have also been applied extensively along the Murray River (and other river systems in Australia) for substrate

characterisation, and they have been used at different times to collect data over the same stretch of river, thereby making a comparative analysis possible.

A direct comparison of data sets was facilitated through the use of a common approach to their display and scaling. Data from the three techniques are compared for a common stretch of the Murray River, near the town of Mildura in southeastern Australia (Figure 2.1). In this case study, the comparison was undertaken with the specific intent of assessing the suitability of these data for characterising riverbed conductivity as a surrogate for pore-water salinity. In particular, we were concerned to assess suitability for identifying zones, or reaches where there was believed to be potentially significant salt flux into the river sourced from a highly saline groundwater system which underlies much of the Lower Murray Basin in south-eastern Australia (Figure 2.1).

2.3 Study area and hydrogeology

The Murray Basin is an intracratonic basin that covers an area of approximately 300,000 square km, and is filled with mostly undeformed Cenozoic carbonate and terrigenous sedimentary rocks that make up the main hydrogeological units (Brown and Stephenson, 1991). A schematic representation of the hydrogeology of the study area is illustrated in Figure 2.2. For the purposes of this study the units of primary interest on the floodplain (immediately adjacent to and under the river) is the near-surface Coonambidgal and Monoman Formations (Brown and Stephenson, 1991; Telfer et al., 2004). These represent the sediments of the currently active floodplain.

The Coonambidgal, an upwardly fining sandy-to-clay unit, was formed in a lower energy stage of the system and overlies the coarser, sandier Monoman sequence. The Monoman is, for much of the river, the main sedimentary unit in the zone immediately adjacent to and beneath the Murray River, and it was deposited as the relatively fast flowing Murray cut a trench through the older sediments of the basin. Along the base of the river, a more recent, alluvial unit is recognised. This unit is made up of silts and sands that are transported and deposited by the present-day river system.

For the highlands areas adjacent to the floodplains, the Woorinen Sands, the Blanchetown Clay, and the Upper Loxton-Parilla Sands comprise the main sedimentary units. Wind-deposited Woorinen Sands overlie the locally discontinuous Blanchetown Clay, which acts as an aquitard, influencing the rate of groundwater recharge from irrigation and rainfall across the region. The Loxton-Parilla Sands unit is the major aquifer adjacent to and beneath the Murray

NOTE:
This figure is included on page 27 of the print copy of the thesis held in the University of Adelaide Library.

Figure 2.1. Groundwater salinity of the Lower Murray Basin, south-central Australia. The location of the study area is indicated with a red polygon. The TDS of seawater is approximately 35,000 mg/L (Murray Darling Basin Commission, 2002).

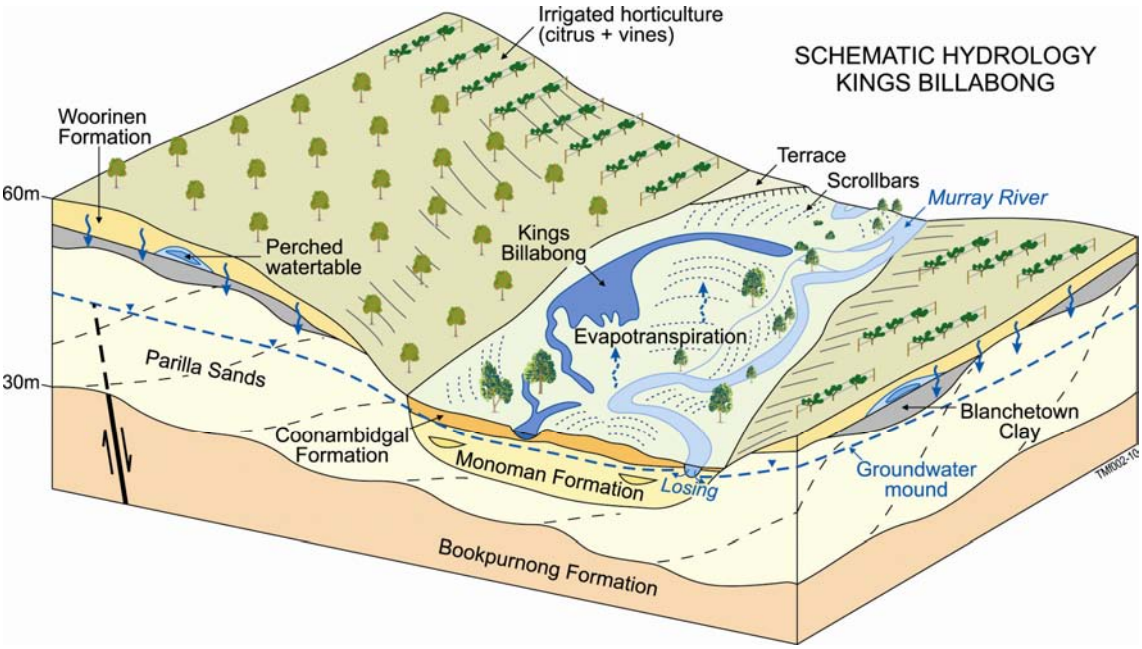

Figure 2.2. Schematic representation of the hydrogeology of the study area. Vertical wavy blue arrows indicate recharge to groundwater systems, primarily linked to irrigation. Horizontal blue arrows indicate regional groundwater flow directions.

River system. The Woorinen sits unconformably over the Blanchetown Clay, which sits unconformably over the Parilla Sands.

The Murray River is the natural discharge point for the regional groundwater system, as indicated by the groundwater flow arrows in Figure 2.2. The river is also the main source of water for the city of Adelaide in South Australia and other smaller towns along its course. It is also the primary source of water for irrigation-based agriculture, which has been developed along its course. Consequently, the mitigation of saline groundwater discharge to the river is critical. Locating potential discharge zones along the river is an important part of managing the level of groundwater discharge and in particular the salt load of the river and it is for this purpose that in-stream geophysical techniques have been used. The techniques also have a role in the ongoing monitoring of the river system, primarily to determine the effectiveness of salt interception strategies (Forward, 2004) that have been developed at various locations along the Murray.

Of primary importance in the process of locating potential discharge zones along the Murray is the identification of river reaches that are gaining (in particular, gaining saline water). Fetter (2001) discusses gaining and losing streams mainly in terms of local climate. In humid areas, with relatively high rainfall and shallow groundwater, a typical stream is likely to be gaining. In arid areas, with lower rainfall and therefore lower groundwater levels, a typical stream is likely to be losing.

In the Murray Basin, with its arid climate, and an often shallow, highly saline groundwater system, discharge to the river is regulated in part by the floodplains immediately adjacent to the river. Their influence is such that gaining and losing (the lateral and downward flux of fresh river water into underlying sediments) conditions change frequently along the river, and are difficult to recognise without careful analysis. Groundwater levels are often above river level, which normally lead to gaining river conditions. However, a combination of evaporative and evapotranspirative processes operating across the floodplain removes a great deal of water from the system, especially during the warm summer months. The consequence is that the floodplain is often a net loser of water (Telfer et al., 2004). When the floodplain is sufficiently large, and these processes are sufficiently rapid, the river will lose water to the floodplain. When the floodplain is small or these processes are too slow, the river will gain water from the floodplain (and the groundwater system that feeds it).

Although geophysical techniques cannot directly measure the flux of water from a groundwater system into a river (or vice versa), they can detect variations in the quality of the groundwater primarily because of its high solute content. Therefore electrical techniques in particular can detect zones in the subsurface that are close to the base of the river and relatively

conductive. In the Murray Basin, nearly all of the groundwater entering the river is saline and therefore conductive. Much of it is greater than 5000 μS/cm (i.e., 500 mS/m or 0.5 ohm-m), as shown in Figure 2.1. In contrast, the river water is relatively fresh, with an electrical conductivity (EC) commonly between 100 and 500 μS/cm (i.e., 10 to 50 mS/m or 100 to 20 ohm-m), as shown in Table 2.1 (EC as used in this study refers to an electrical conductivity measurement of a fluid using an EC meter). Consequently, enough contrast exists between these two fluids to make detection of the saline groundwater relatively easy. Telfer et al. (2005) and Tan et al. (2007) note strong correlations between the location of zones that are more conductive immediately below the river base and gaining stretches of the river (specifically, zones gaining saline groundwater). Telfer et al. (2005) report that zones immediately under the base of the river, where observed electrical conductivities were greater than approximately 330 mS/m (3 ohm-m), were correlated with known gaining stretches of the river.

In this study, we focus on the acquisition of geophysical data for a common stretch of the Murray River in southeastern Australia, making a direct comparison of their results relatively straightforward. Between 2004 and 2006 two ground surveys and one airborne survey were undertaken from approximately river km 895 to 920, (between Kings Billabong and Red Cliffs, along the Victorian and New South Wales State border - Figure 2.3).

2.4 Methods

The three in-stream techniques examined here include two ground-based systems (a fast-sampling TEM system, and a direct current (DC) resistivity system) and an FDHEM system. A comparison of each data set is based on analysis of results using the algorithms and inversions that are used routinely in the processing of that data set. In addition, these results are compared with bore data acquired using an in-stream drilling technique that recovers continuous core in unconsolidated sediments.

Table 2.1. Comparison of shallowest level conductivity and river EC at recording location 414204.

NOTE:
This table is included on page 29 of the print copy of the thesis held in the University of Adelaide Library.

Source: Data from Department of Sustainability and Environment (2010)



Figure 2.3. Map indicating the reach of the river surveyed with the various techniques. The yellow line indicates the location of depth sections shown in Figure 2.6. The depth sections shown in Figure 2.7 are for the reach marked by the red line.

2.4.1 In-river TEM: NanoTEM

The in-river TEM system used for this survey work was Zonge Engineering's NanoTEM system. This inductive, electromagnetic geophysical system was developed in the early 1990s as a fast-sampling geophysical tool for near-surface investigations. The data acquired for this study were collected in February 2004. A 7.5 x 7.5-m transmitter/receiver frame was towed 12 m behind a small boat, collecting data at discrete time intervals. The outside of the frame was set up as the transmitting antenna, with a single turn of wire attached to the frame. The 2.5 x 2.5-m receiving antenna was mounted in the centre and was also made of a single turn of wire (Figure 2.4). Data were collected and recorded in a near-continuous mode, every 4 s, stacking 64 cycles

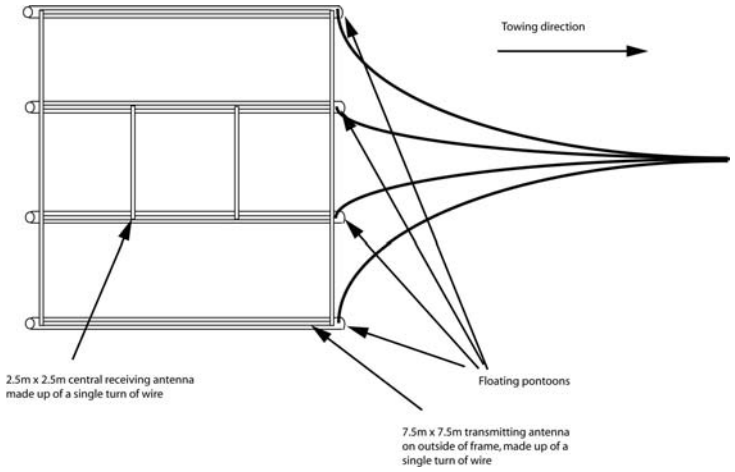

Figure 2.4. Schematic diagram of the in-river TEM rig.

for 2 s at a repetition rate of 32 Hz. At 7 km/h on the river, data were recorded at approximately 8-m intervals. A Global Positioning System (GPS) unit linked to a depth sounder was used to collect information on location and water depths coincident with EM data acquisition.

Following acquisition, the three data sets (TEM decays, GPS locations, and water depth) were combined and the TEM data set inverted using a 1D smooth-model layered-earth inversion – Zonge Engineering's STEMINV routine. The results were then stitched and presented as a conductivity-depth section. The 1D model assumption used for this inversion is valid in sub-horizontal, layered sedimentary settings that are encountered in the study area, where it produces results that are only slightly distorted by 2D or 3D effects that could be induced by marked changes in substrate topography, faults, fractures, or other short-wavelength geological phenomena.

The STEMINV smooth-model inversion generates an initial model from a half-space resistivity calculated from averaged late-time resistivity for each time window (Spies and Eggers, 1986). An averaged resistivity for a given sounding is then used to calculate an approximate representative depth based on dispersion-depth type calculations (Jones, 1983; Spies, 1989). This maximum depth is then divided into many thin layers with fixed thicknesses. Although the final resistivity distribution for a given sounding is different from the starting model, the initial starting depth is usually a reasonable estimate of the depth of investigation for a given sounding (where 1D model assumptions hold).

2.4.2 In-river resistivity: Blue Eel

The in-stream resistivity system used in this study was the Groundwater Imaging Blue Eel DC Resistivity array (Allen and Merrick, 2003). The Blue Eel is a floating galvanic resistivity array (156 m long) towed behind a small boat. It combines a single pair of transmitting electrodes

and eight receiving electrodes (Figure 2.5). In this study, data acquired in March of 2004 were analysed. The transmitting electrodes were spaced 16 m apart and towed approximately 12 m behind the boat. The eight receiving electrodes (i.e., seven receiving electrode pairs) were spaced at distances increasing by powers of two, starting 1 m behind the farthest transmitting electrode. The spacing between the seven receiving electrodes was 1 m for the first pair, 2 m for the second, 4 m for the third, 8 m for the fourth, 16 m for the fifth, 32 m for the sixth and 64 m for the seventh (Figure 2.5). Data were collected every 4 s, stacking eight signal cycles for 2 s at 4 Hz. The boat averaged 10 km/h on the river, and at that speed data were collected at approximately 12-m intervals along the river. The GPS locations and water-depth data were collected at the same time. Transmitter currents for this survey, using a battery powered transmitter, were generally below 0.5 A (Allen, 2007).

When looked at in terms of standard, dipole-dipole resistivity terminology, the first three receiving dipoles are all less than n=0.5, and the fourth receiving dipole is similar to n=0.5. The fifth receiving dipole is equivalent to n=1, the sixth is a combination of n=2 and 3, and the last receiving dipole is a combination of n= 4 to 8. The receiving dipoles are set up this way to ensure that high-resolution shallow data can be recorded together with good quality data at greater depths, given the relatively weak transmitter currents (Allen and Merrick, 2003). Amidu and Dunbar (2007) use the same strategy in their reservoir study. As the river water is relatively resistive, on the order of 10 mS/m or 100 ohm-m, higher transmitter currents could not be generated without resort to the use of large generators or banks of batteries. The limited size of the survey craft employed for the survey did not permit this.

As with the in-stream TEM described earlier, the receiver data, GPS locations, and water depths were combined and the resistivity data then inverted. Instead of a smooth-model inversion, these data were inverted using a discrete-layer-type of 1D inversion (Allen and Merrick, 2007). This inversion routine uses a small number of layers to represent the subsurface, with the ability to show abrupt changes in the subsurface (as might be seen at the base of the river/sediment interface) more accurately than minimum-structure, smooth-model inversions (such as STEMINV, described previously). It sets a number of layers at the start, based on the number of data dipoles that are collected and is, therefore, usually fixed at five to seven layers, for which both thickness and conductivity are allowed to vary. This inversion routine sets the depth to which it inverts by using a set of standardised effective depths (based on the transmitter and receiver electrode configuration) assigned to each receiving electrode pair (Roy and Apparao, 1971; Allen and Merrick, 2007). Apparent resistivity is then calculated for each electrode pair using standard equations for apparent resistivity (Telford et al., 1976). These are

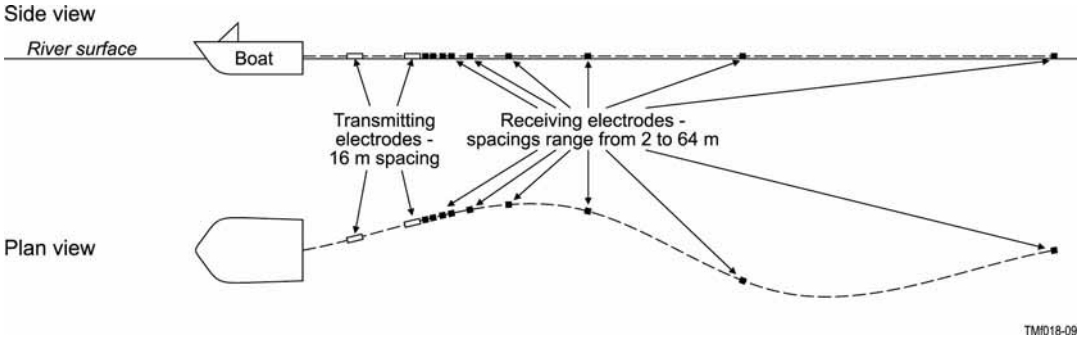

Figure 2.5. Schematic diagram of the in-river DC resistivity rig.

then assigned to each layer as the starting model resistivity for the blocky inversion.

Although the number of layers is not allowed to vary in this inversion, layer resistivity and thickness are. Consequently there is variation from the starting model total depth as the inversion progresses. Nevertheless, in this predominantly 1D environment, the initially assigned total depth does not vary greatly from the starting model, with most of the observed variation occurring in the conductivity parameters. Variation between layers is not required to vary smoothly with depth (Allen and Merrick, 2007). This interpretation approach has been used extensively for surveys undertaken along the Murray River and in associated waterways.

2.4.3 Airborne electromagnetics: RESOLVE FDHEM

The airborne electromagnetic (AEM) data for the study area were acquired using Fugro Airborne Surveys RESOLVE FDHEM system. For the RESOLVE system, the transmitting and receiving antennas are housed in a bird slung approximately 30 m below a helicopter. Terrain and obstacle permitting, the bird is flown at an elevation of 30 m above the ground at a speed of 120 to 130 km/h. For this survey, data were collected at six frequencies: 383, 1845, 3263, 8120, 39,620 and 136,400 Hz. Five of the six receiver-transmitter/frequency coil pairs in the bird collect data in the horizontal coplanar orientation, with the 3263 Hz coils set to read in the vertical coaxial orientation (D. G. Garrie, 2006, Fugro Airborne Surveys Corp. RESOLVE survey 06055).

During data acquisition, 10 soundings were recorded every second, generating a spatial sample of approximately 3 m. For this survey, conducted in October of 2006, the helicopter was equipped with the FDHEM system, a GPS system, two altimeters, as well as a system to record variations in the Earth's magnetic field (D. G. Garrie, 2006, Fugro Airborne Surveys Corp. RESOLVE survey 06055).

The quantity of data recorded in a typical day for an FDHEM survey is significantly larger than that for the other two techniques reviewed in this study. Normal data preprocessing usually involves at least two stages of drift correction and spatial filtering to remove predominantly

spheric noise (D. G. Garrie, 2006, Fugro Airborne Surveys Corp. RESOLVE survey 06055), and then inversion. For this study the RESOLVE FDHEM data were inverted using a holistic inversion developed by Brodie and Sambridge (2006). This inversion routine produces quasi-3D conductivity models, based on a computationally efficient 1-D forward modelling algorithm, and is similar to the spatially constrained inversion of Viezzoli et al. (2008; 2009). The holistic inversion uses the raw, uncalibrated, uncorrected data and then combines all of the data processing and inversion into one large, simultaneously solved inversion problem (Brodie and Sambridge, 2006).

This routine treats all of the variables that are difficult to control for, but that contribute to the drift corrections that the normal processing takes care of, and solves for them by making them unknowns in the inversion routine. This is partially accounted for by treating the data as a spatial whole, by regularizing a consistent grid over the spatial extent of the data set. By doing this, the program takes advantage of interfrequency and spatial coherence in the data sets. The result is an inverted conductivity model that is both laterally and vertically smooth. For single-line data sets (like the one examined in this study), spatial coherence is determined in the along-line direction, because there is no crossline information.

2.4.4 In-stream coring

Vibrocoring is a drilling technique that is designed to collect complete samples in unconsolidated environments like those encountered in this study. The technique relies principally on the gravity fall of a vibrating hollow-core barrel assembly to liquefy the unconsolidated sands and clays through which the core barrel is travelling. Core collected in the hollow stem is then extruding into sausage-shaped plastic bags. This technique has been one of the preferred methods for recovering continuous core in unconsolidated sediments commonly found across the floodplains of the Murray River. However, until recently, the technology has been generally limited to core recovery depths of 6 to 7 m. These limits are in large measure determined by the weight and power of the coring unit. Using a combination of developments, including the frequency modulation of the vibrating head, and changes to barrel and core catcher design, along with adjustments to the application of vacuum and air delivery, as much as 25 m of continuous uncontaminated, unconsolidated sediment core can now be recovered (K. P. Tan, personal communication, 2009).

As part of a larger study, cores were collected for 14 holes using a Vibracore rig mounted on a floating pontoon. A complete review of the results from this program is contained in an upcoming report (K. P. Tan, personal communication, 2009). Nine of the holes were located in

the river between river km 895 and 920 and are pertinent to the analysis of the geophysical data sets discussed here.

Riverbed core and contained fluids were collected in a plastic sausage-shaped bag. These were then sampled at 0.5- to 1-m intervals and the samples were lithologically logged, and the contained pore-water extracted and sampled for total dissolved salts (TDS). Laser grain-size analysis was also performed on a subset of samples. It is important to note that TDS values were chemically measured, instead of being estimated from the fluid EC. Figure 2.3 shows the locations of these holes in the study area.

2.5 Results

To aid the comparative interpretation of the three data sets from each of the geophysical methods we examined the inverted data using a common display and unit representation. Those data analysed here are from the reach of the Murray River shown in Figure 2.3.

2.5.1 River conditions

Given that data from the three techniques were acquired during a three-year time frame, we sought to understand whether river conditions were significantly different during that period. In part, the intent was to determine whether changing conditions might have to be considered as a factor affecting the observed conductivity structure. The Murray River is a highly regulated system with river levels controlled by a series of locks that are present at regular intervals through its lower reaches.

Table 2.2 details river gauge levels measured at recording site 413002 which is located at approximately river km 936 (Figure 2.3), approximately 16 km upstream of the upstream end of the stretch examined here. Recording site 414204 (used for Table 2.1) is located within the reach studied, but river level information has only been collected there since January 2005. Available data indicate that river levels through the study area were relatively stable, varying less than 0.2 m over the time spanned by the three test surveys. Therefore, we believe that the results from the different surveys should reflect relatively constant river conditions.

2.5.2 Conductivity-depth sections and borehole data

Stitched conductivity-depth sections for each of the three data sets are presented in Figure 2.6 for the full reach studied (see Figure 2.3 for the location). A schematic geological section compiled from borehole data is presented also (Figure 2.6a). The main lithological units identified in this figure include “Qa, river-bed”, referring to recent river-bed deposits, which are

Table 2.2. River level at recording location 413002.

NOTE:
This table is included on page 36
of the print copy of the thesis held in
the University of Adelaide Library.

Source: Data from NSW Water Information (2010)

primarily sands to sandy silts. These sediments overlie the older alluvial sequence Monoman Formation (labelled as "Qa, Fm" in Figure 2.6), a predominantly sandy unit under the river. This sequence is seen along the entire extent of the Murray Trench and overlies the Parilla Sands (labelled as "Tps" in Figure 2.6). As noted earlier, the Parilla Sands is the major aquifer unit adjacent to and beneath the Murray River system.

Figure 2.6b shows results (expressed in EC units and represented as a coloured bar) from chemical analysis of pore-water samples extracted from cores collected in the Vibracore drilling program, completed in March 2007. The salinity of pore-water samples expressed as TDS in mg/L were converted to EC in mS/m by using the following approximation (this conversion procedure is in common use, see for example Spies and Woodgate (2004)).

$$EC = \frac{TDS}{6} \quad (2.1)$$

The modelled conductivity for the riverbed sediments derived from the in-river TEM run is shown in Figure 2.6c. Figures 2.6d and 2.6e show the modelled conductivities for the in-river DC resistivity and FDHEM surveys, respectively. Water-depth information as collected during the in-river TEM and the in-river resistivity surveys is shown on their respective sections as a grey line. For the purposes of interpretation, we have added the water depth measured during the in-river TEM survey to the FDHEM conductivity-depth section (as indicated by the black line).

In Figure 2.7, we present a more detailed comparison of data from the three technologies for a 6-km subset (see Figure 2.3 for the location), corresponding to the reach between stations 9000 and 15000. Figure 2.7a shows the results for the in-river TEM run, Figure 2.7b shows the results for the in-river resistivity run, and Figure 2.7c shows the results for the FDHEM run.

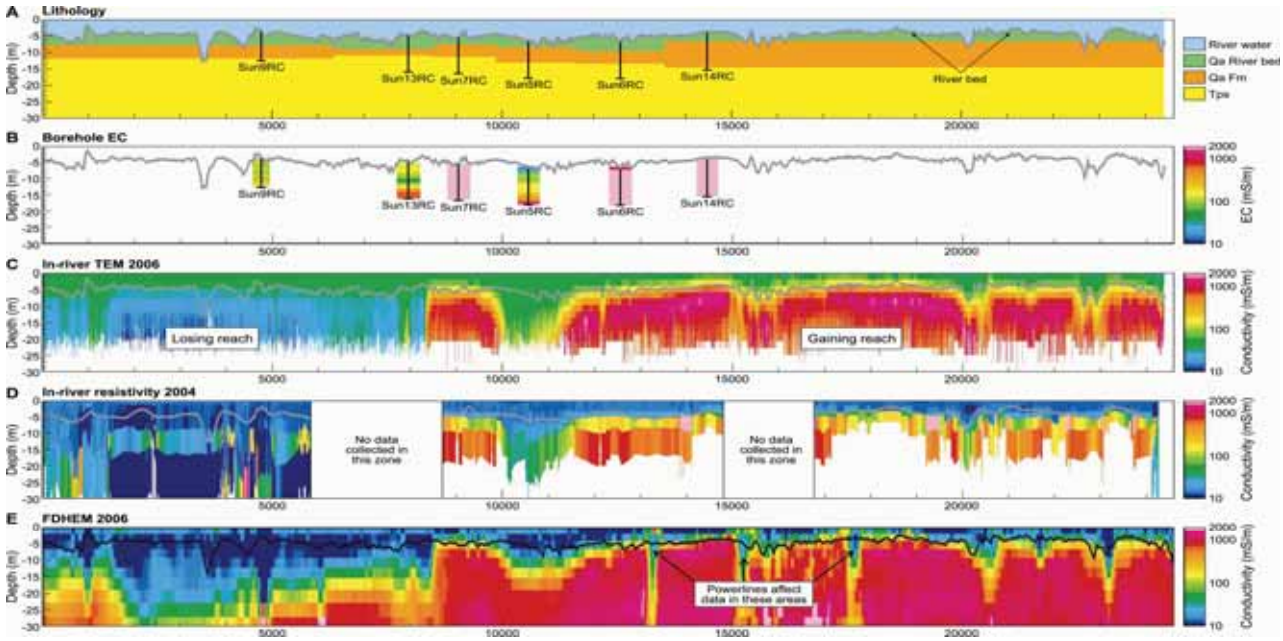

Figure 2.6. Depth sections of complete data runs: (a) interpolated lithology; (b) borehole TDS converted to EC; (c) inverted in-river TEM data; (d) inverted in-river resistivity data; (e) inverted FDHEM data. The vertical axis is depth below river surface in metres. The horizontal axis is distance along river in metres. Water depth is indicated on the in-river TEM and in-river resistivity sections (c and d) with a grey line. Water depth as measured during the in-river TEM survey is superimposed in black for comparison purposes on (e) (FDHEM data set).

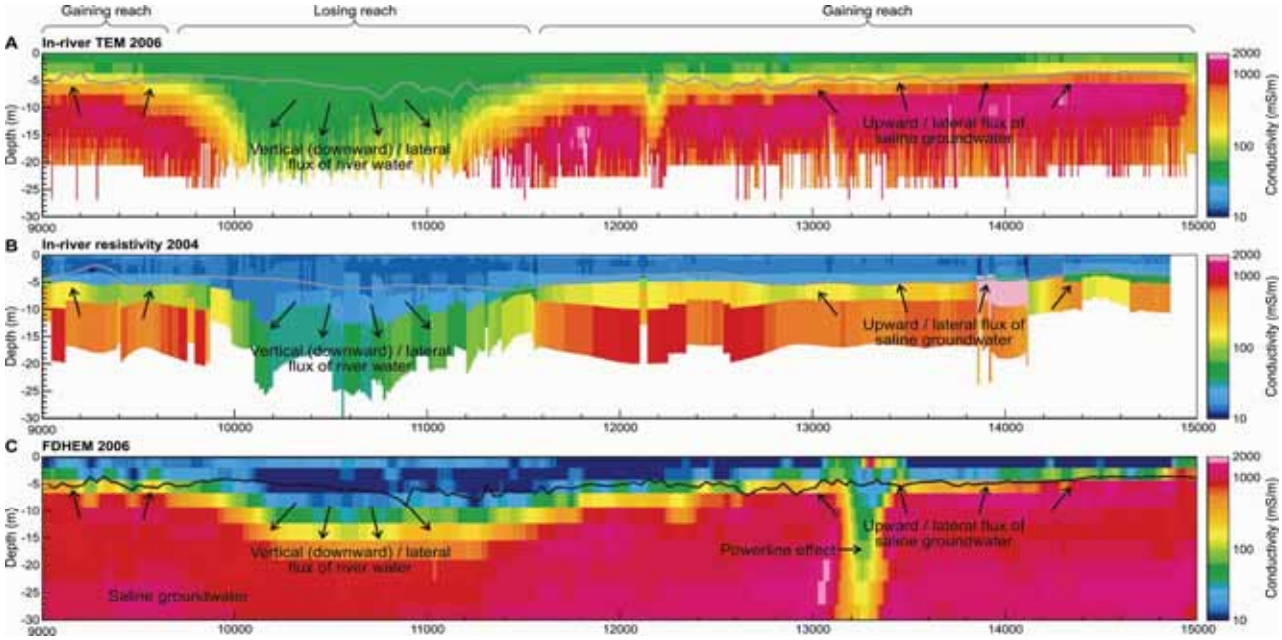

Figure 2.7. Depth sections of the smaller comparison stretch of the river: (a) inverted in-river TEM data; (b) inverted in-river resistivity data; (c) inverted FDHEM data. The vertical axis is depth below river surface in metres. The horizontal axis is distance along river in metres. Water depth (as measured at the time of each survey) is indicated on the in-river TEM and in-river resistivity sections (a, b) with a grey line. Water depth as measured during in-river TEM survey is superimposed in black for comparison purposes on (c) (FDHEM data set).

Spatial patterns of riverbed resistivity

Of primary interest on in-steam surveys for salinity mapping are the observed spatial patterns of sediment conductivity immediately beneath the base of the river. An examination of these model parameters with a spatial perspective permits a qualitative correlation between the observed conductivity, the proximity to irrigation areas, and other possible drivers of salinity variation along the river. This technique has been used successfully in previous investigations (Barrett et al., 2005; Telfer et al., 2005). Conductivity data from the layer immediately under the base of the river are displayed as a classified layer overlaid on an air photo of the study area. To allow comparison with regional conductivity patterns a 6.62- to 9.28-m depth slice (below ground surface) derived from an HEM survey, which the authors acquired, over the Sunraysia region in 2006 is used as an intermediate underlay. These data were also processed using the holistic inversion, and are presented using the same colour scale as the in-river geophysical data presented in this study.

For the in-river TEM and in-river DC resistivity data sets, conductivity information was extracted from the inverted data sets for the layer immediately below the river base. Water depth information cannot be collected during an AEM survey. Consequently an alternative layer was defined. Given that water depth is known to vary between 3 to 10 m along this stretch of river an interval conductivity map for the 6.6- to 9.3-m layer below the ground surface was extracted from the inverted FDHEM data. These data were then classified and displayed on the air photos in a manner similar to data from the other two ground techniques, as shown in Figures 2.8a-c.

2.5.3 Borehole data

The logged lithology and TDS values (presented as EC values) derived from the analysis of core for two in-river bores are plotted against the corresponding vertical conductivity structure determined for the in-river TEM, in-river resistivity, and the FDHEM techniques (Figure 2.9). Soundings closest to the bore location were used. For each plot, the vertical axis is presented as a depth below the river bottom (in metres). These plots do not show any information pertaining to the conductivity of the river itself. The horizontal scale for the geophysical data is shown in mS/m. For the FDHEM, the river bottom measurement used in presenting the results was approximated by using water depth as measured during the in-river TEM survey. Figure 2.9a shows results from drill hole Sun06RC, located in a relatively conductive stretch of the river (see Figure 2.3 for the location). Figure 2.9b shows results from drill hole Sun09RC, located in a relatively resistive stretch of the river (see Figure 2.3 for the location). These results are typical for the 10 drill holes tested on this stretch of river.

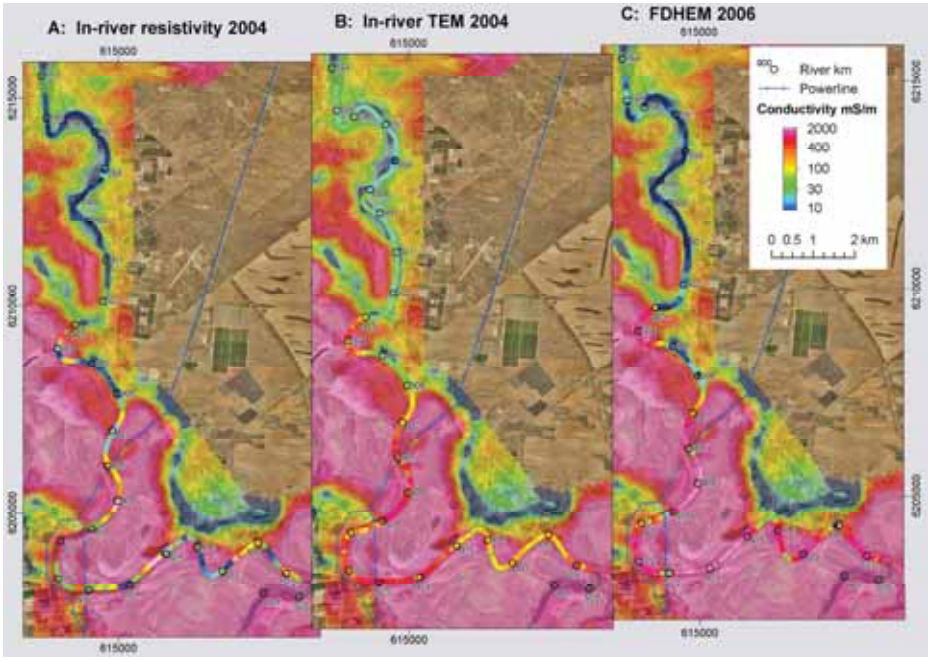

Figure 2.8. Contoured river-bottom data. These data were taken from layer immediately below the measured water depth from each inverted data set: (a) in-river resistivity; (b) in-river TEM; (c) FDHEM. The 6.6- to 9.3-m depth layer was used for the FDHEM. The main underlying image is an air photo image showing regional land use and patterns. The intermediate background image is the 6.62- to 9.28-m depth slice taken from the 2006 regional FDHEM survey collected in this area.

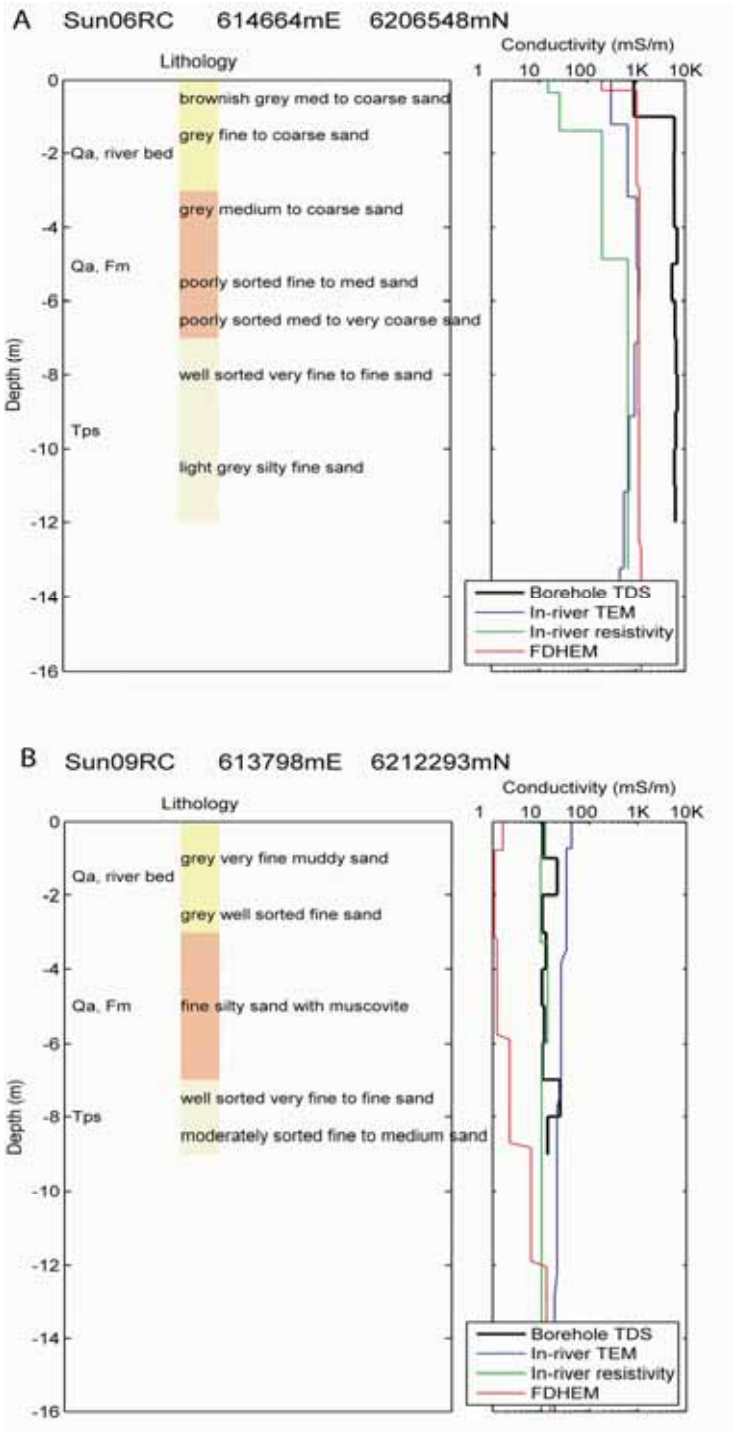

Figure 2.9. Comparison of geophysical results with drilling logs for two boreholes: (a) results for borehole Sun06RC; (b) results for borehole Sun09RC. Logged lithology and downhole sampled TDS results (converted to EC) have been plotted against results from geophysical techniques. The vertical axis is depth below river bottom in metres.

2.6 Comparisons

2.6.1 Conductivity-depth section comparison

An examination of the conductivity-depth sections (Figure 2.6c-e, and 2.7a-c) indicates that lateral variations in the observed conductivity structure defined by each technique are well correlated. All three techniques identify resistive and conductive zones at the base of the river, in similar locations, that are consistent with patterns observable in the FDHEM depth slice presented in Figure 2.8a-c. Conductive zones at the base of the river are interpreted as reaches where saline groundwater is either close to, or discharging directly into the river, i.e., where the river is gaining. Resistive zones imply the vertical flux of fresher river water into the adjacent or underlying sediments, referred to as losing reaches, although it may be more appropriate to describe them as hyporheic zones. Hyporheic zones are zones along a river or stream where there is a mixing of shallow groundwater and river water beneath and next to the riverbed, through a hyporheic, or through-flow process.

The sediments under the river are generally more resistive from station 0 to station 8500, suggesting that this stretch of the river is predominantly a losing reach. A contributing factor to the observed conductivity structure is the presence of irrigated land on the highland immediately to the east of the river. Downward recharge from excess irrigation water leading to the development of a groundwater mound could lower the saline groundwater system in this area. The relatively conductive zone observed at depth in the FDHEM data set (Figure 2.6e) from stations 2000 to 4000 suggests the presence of a deeper saline groundwater system. This is not seen in the results from either of the ground-based methods (Figures 2.6c and d). In this reach, there also could be some groundwater flow from west to east from the Kings Billabong floodplain (Figure 2.3, Figure 2.8a-c: west of the river between river km 898 and 902). Kings Billabong is a relatively fresh water body held at a slightly higher elevation (from 1 to 2 m) than the adjacent river to the east. This head difference might encourage some west-to-east flow as represented schematically in the hydrogeologic model shown in Figure 2.2.

An abrupt change occurs in the conductivity structure at station 8500 (river km 903) where the river takes on predominantly gaining conditions upstream of that point. The cause of this sudden change might be linked to a combination of geologic factors, most likely involving the influence of structural or sedimentary facies controls on groundwater discharge. This area is cut by a series of normal faults that propagate from the basement through the near-surface sediments (shown schematically in Figure 2.2). Facies changes associated with the Parilla Sands (a prograding beach-barrier sand sheet (Brown and Stephenson, 1991)) are common, and

the sharp change in conductivity could correspond to the presence of a more transmissive facies promoting the lateral flow of fresh water from Kings Billabong back into the river at this point.

From station 8500 to 10000, each of the three techniques defines a predominantly conductive stretch at the base of the river. We surmise that the saline groundwater system is likely to be discharging into the river in this reach. From station 10000 to approximately station 11500, the sediments directly beneath the river are again resistive, suggesting a smaller zone of hyporheic flow. This feature is described by Telfer et al. (2004) as being an area where an underlying clay unit (the Geera Clay – a member of the Murray Super-group that underlies the Parilla Sands and the Bookpurnong Formation) has been uplifted via basement faulting, and is acting as a "choke" for the saline groundwater system, preventing it from discharging into the river farther downstream. Telfer et al. (2004) also postulated that this could cause the river immediately upstream of this point to go from losing to gaining conditions. From station 11500 to the end of the section on the right (approximately station 24500) the sediments under the river are mostly conductive, again interpreted as a gaining reach.

Figure 2.6a shows the interpreted lithology, from the Vibracore bores drilled into the base of the river. The lack of correlation between the sedimentary layering and the observed conductivity structure supports observations (K.P Tan, personal communication, 2009; Tan et al., (2007)), that conductivity variations are primarily related to differences in the solute content of the pore water contained in the sediments. A comparison between the TDS values and modelled vertical conductivity structure for two boreholes (Figure 2.9) also supports this observation, indicating that the logged TDS values correlate with modelled variations in conductivity. These results are similar for the rest of the boreholes in the study area.

To evaluate the ability of the three techniques to resolve finer scale features conductivity-depth sections for a more limited section of the river were examined (Figure 2.7). A relatively small "resistive hole" centred around station 12200 is clearly resolved in the in-river TEM section but is not apparent in the FDHEM section and is difficult to define in the in-river resistivity section. This feature was noted in a later in-river TEM survey conducted in 2006, although its cause remains undetermined.

2.6.2 Shallow data comparison

Table 2.1 shows a comparison between river EC readings as measured at the Red Cliffs river monitoring site (414204, located at approximately 614026 mE, 6204550 mN, near river km 910.5, approximately station 15300 in Figure 2.6) and the conductivity information from layer 1 (i.e., the shallowest layer) in the inverted geophysical data sets. Data have historically been

collected from this site on a weekly to monthly basis. The values shown here have been interpolated to best match the date that the geophysical survey data were collected. Note that in-river DC resistivity data were not acquired at this exact location because there was a break in this data set, with the subsection shown in Figure 2.6d ending approximately 270 m upstream of this point. This is not likely to affect the quality of this comparison as the change in water salinity along the river is known to be quite gradual.

Results in Table 2.1 suggest that the in-river DC resistivity method is better at determining water resistivity than either the in-river TEM or the FDHEM. Nevertheless, the FDHEM appears to be affected by powerline noise at the monitoring site, and an examination of the shallowest data at stations 200 m up- and downstream of this location (i.e., away from the powerline) suggest that those FDHEM conductivities are closer to the measured value at the monitoring site than the FDHEM conductivities at the monitoring-site location.

It is worth noting that in resistive stretches of the river (e.g. Figure 2.7, near station 11000), none of the techniques resolve the depth of the river very well. This is attributed to the limited conductivity contrast between the river water and saturated river-bottom sediment, making resolution of this boundary particularly difficult. As the conductivity of the sediment-river interface is dominated by variations in the conductivity of the water, this observation accords with the modelled responses.

Our observations indicate that the in-river TEM is not as effective as the other two techniques in resolving the conductivity of the river in this area. However, the TEM data do define a subtle conductivity contrast at the base of the river and therefore resolve the depth of the water. The inverted FDHEM data set provides indicative values of water conductivity and the water depth in conductive settings. The absence of water-depth information of any type would render the FDHEM data more difficult to interpret, in these settings. We have not given consideration to the issues of bird swing or pitch in the inversion and interpretation of the FDHEM data, but we believe that the FDHEM results might be improved if these airborne system geometry issues were considered, and data acquisition strategies were developed with these issues in mind.

2.6.3 Shallow sediment plot comparison

The plan view maps describing the spatial variability of riverbed sediment-conductivity patterns are shown in Figure 2.8 for each of the three techniques. Overall, the three techniques provide comparable information over this stretch of the river, with the gaining and losing stretches identified. All three data sets correlate well in the more resistive part of the river to the north, with

the in-stream resistivity and FDHEM possibly representing a closer representation of the "true" shallow-sediment conductivity, based on the measured conductivity of the river water in that area (Table 2.1). In the gaining stretches to the south, a better correlation exists between the in-river TEM and the FDHEM. The in-stream resistivity data produces a more variable plot of riverbed sediment conductivity, and in places suggest the presence of losing reaches when both the FDHEM and TEM data suggest the river might, in fact, be gaining (see, for example between river km 907 and 908). We believe the discrete-layer inversion used in the interpretation of these data needs to be refined to improve the technique's ability to display consistently the conductivity structure under the river.

2.6.4 Comparison with river EC measurements

Results from each of the three geophysical techniques are compared with in-river measurements of river water EC (conductivity) and are presented in Figure 2.10. These data were collected as part of a program of Run-of-River (ROR) surveys performed along the Murray River on a regular basis by the South Australian Department of Water, Land and Biodiversity Conservation and its predecessors. The ROR surveys have been used to identify reaches of the river that are gaining salt from a discharging saline groundwater system. These reaches might warrant the development of salt interception schemes, as described by Forward (2004). This methodology has been in use on the Murray since the late 1980s (Porter, 1997, Run of River report; Porter and Branford, 2002, Run of River report; Porter and Rouse, 2006, Run of River report).

In an ROR survey, EC readings are collected at regular intervals (usually every kilometre) along the river, and the readings repeated during five days to allow averaging and trend removal. The contribution that a given kilometre makes to the total river salinity is estimated by averaging the readings at each kilometre, and then calculating the difference between adjacent kilometre readings. Figure 2.10 shows the results from an ROR survey that was run in December 2001. The ROR data are presented as a bar graph with the river EC data highlighted in red. Differenced river water EC measurements have been plotted against the sediment conductivities derived from the three techniques examined in this study. The plotted sediment-substrate conductivity values are from the layer in each inversion immediately beneath the riverbed, except for the FDHEM, where the interval conductivity from 6.6- to 9.3-m depth layer was used. The horizontal axis is distance in metres along the test stretch of the river (i.e., the

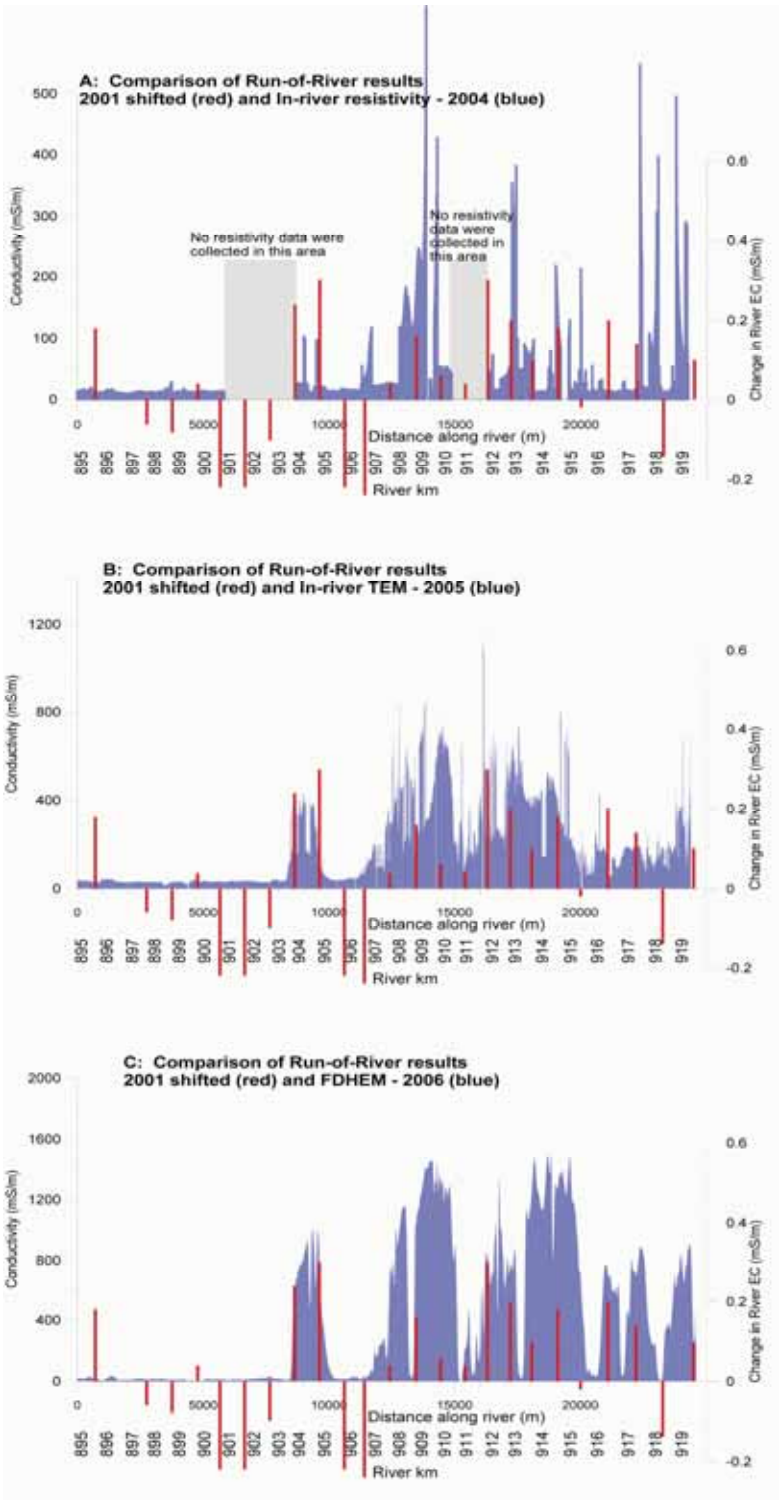

Figure 2.10. Comparison of geophysical results with ROR EC measurements: (a) ROR compared with in-river DC resistivity; (b) ROR compared with in-river TEM; (c) ROR compared with FDHEM. Results from each geophysical survey are shown in blue; 2001 ROR EC results are shown in red. The horizontal axis is distance along the river and river km. The right vertical axis is change in river EC in mS/m. The left vertical axis is conductivity in mS/m.

same as the horizontal axis in Figures 2.6 and 2.7), as well as river km. The left axis is a measure of the river water conductivity, and the right vertical axis indicates the relative change of river EC.

The location of the river EC data have been shifted in these plots 2 km upstream. This procedure is routinely undertaken to account for river flow and vertical mixing in the water column away from the actual sources of saline discharge into the base of the river. Identifying the source of the salt entrained in the river can vary, depending on the speed and "tortuosity" of the river in a given location (Telfer et al., 2004).

2.7 Discussion

Some of the differences in the observed conductivity structure defined for each of the three technologies for this stretch of the Murray River might relate to differences in the inversion algorithms. However, some of the variability is likely to stem also from differences in the nature of the systems used, and this is explored further here. Two of the techniques are inductive, specifically the towed EM and the helicopter EM, and one is galvanic. For the inductive methods, differences might arise from their mode of operation, namely that one operates in the frequency-domain (the FDHEM) and one in the time domain (the in-river TEM). Consequently variations in the depth of investigation, along with lateral and horizontal resolution, are to be expected. For this type of study, the comparison of the results over the same stretch of ground/river provides most of the pertinent information about differences in system response.

2.7.1 System resolution

Much of the system-resolution discussion that follows is based on analysis related to skin-depth type equations (Spies, 1989). It is recognised that the measure of depth of investigation and resolution involves integrating information about transmitter and receiver moment, system noise level, and external noise (Spies, 1989) and then evaluating the ability of the system to discriminate conductive bodies at depth (Beamish, 2004). The analysis in this section provides some simple, systematic comparison of the systems used in this study.

2.7.1.1 In-river TEM

TEM, being a time-domain based inductive technique, depends on the timing of the windows or gates that it samples, and how quickly the transmitter turns off for its shallow resolution. The strength of the transmitted signal and the system's intrinsic noise level determine its depth of investigation. Based on diffusion-depth type calculations (Jones, 1983; Spies, 1989), a system with a first window reading time of approximately 5.6 μs after transmitter turn-off, and a

noise floor of approximately 50 μV is most sensitive between 4- and approximately 20-m depth in conductive areas. In more resistive zones the shallow resolution is not as good, but depth penetration is increased. The depth limit is not fixed because the number of usable windows is variable, and is largely dependent on the noise floor of the system. It is interesting to note that the maximum depth, as calculated by the STEMINV algorithm for the data collected during this study, was similar for both resistive and conductive areas to about 20-m depth. The ability of the system to read to later times in conductive areas seems to compensate, at least partially, for the lack of penetration in these conductive areas.

Horizontal resolution for this type of system is very similar to the loop size (7.5 x 7.5 m) near the surface. Based on equivalent current filament approximations, the lateral resolution expands to an area approximately 45 x 45 m by the time the signal is at 20-m depth (Nabighian and Macnae, 1991).

2.7.1.2 In-river resistivity

The in-river DC resistivity system used here, being a galvanically based technique, depends on the spacing between the transmitting electrodes and the receiving electrodes to define its resolution, vertically as well as horizontally. The shallow resolution (and footprint) is set by the spacing between the transmitter electrode pair and the closest receiver pair. Similarly, deep resolution is related to the largest receiving electrode that collects usable data. This is an important distinction to make because data quality at large receiver spacing is directly proportional to the strength of the transmitter current and inversely proportional to the ground conductivity. If the ground is so conductive that at a given current the signal level from a receiving dipole is less than the noise limit of the receiver, it will not be used and the next closer/smaller dipole of data defines the depth limit of the system. Based on resistivity-sensitivity studies (Roy and Apparao, 1971; Allen, 2007), and the geometry of the in-river DC resistivity system's closest receiving pair, this system should start resolving information at a depth of approximately 0.25 m below the river surface. Depending on the number of receiver dipoles that collect usable data, depth of penetration for this type of system is limited to about 20 m (Allen, 2007).

The horizontal resolution for this type of system is very similar to the scale of the distance between the smallest receiving and transmitting electrodes, i.e., on the order of 17 m. It expands to an area similar to the distance between the furthest useable receiving and transmitting electrodes pairs, i.e., on the order of 80 m for the largest electrode spacing (Loke, 2001). These footprints are elliptically shaped, with the long axis parallel to the river/line, and the short axis

perpendicular to the river/line. It is worth observing that for this system, the depth of penetration is generally deeper in resistive parts of the river and shallower in conductive parts.

2.7.1.3 FDHEM

The FDHEM system used for this survey depends on a limited number of frequencies for its depth resolution. Beamish (2003; 2004) uses Ward's equations (1967) to calculate the electrical fields in homogeneous half-space earth from an elevated transmitting dipole and then maps the skin depth and footprint of the airborne system at a number of frequencies and ground conductivities based on those equations. His analyses are based on a slightly smaller range of frequencies than the FDHEM system used for this study; it is nevertheless enough information to allow the expected system response to be extrapolated.

From the work of Beamish (2004), for a conductive half space of 100 mS/m (10 ohm-m) (i.e., a relatively conductive environment), the FDHEM should resolve features from less than 4-m depth. A similar analysis suggests that the system should also be able to resolve features to a depth of approximately 20 m. As with the TEM system, the shallow estimate is deeper in more resistive ground. In addition, Beamish (2004) suggests that for a flying height of 30 m, the skin-depth of the transmitter should never extend past 20-m depth. Experience suggests that this limit is too low, and that in more resistive ground this system can collect information at significantly greater depths than these estimates; in practice, greater than 60 m is not uncommon.

The footprint (i.e., lateral resolution) of the FDHEM system is largest at the surface and becomes smaller with depth (Beamish, 2003). Therefore, we will estimate only the size of the footprint at the surface because this will define the maximum lateral resolution of the system. Again, Beamish analyses a slightly smaller range of frequencies than the FDHEM system using two representative half-space conductivities; it is nevertheless enough information to allow the expected system response to be extrapolated. Using figure 8 from Beamish (2003) the along-line footprint (i.e., short skin distance [SSD]), is on the order of 40 m across in a 1 to 100 mS/m half-space (10 to 1000 ohm-m). The across-line footprint, (i.e., long skin distance [LSD]) is on the order of 100 m across in the same half-space earth. Both of these estimates are made using the lowest FDHEM frequency (i.e., 385 Hz, the frequency with the largest footprint and the deepest penetration) at a flight height of 30 m.

2.8 Conclusions

Each of the three geophysical techniques examined produced comparable results in that they identified similar patterns and variations in the conductivity structure of the river-bed. By inference, they also mapped the same hydrogeological conditions as they varied along the river.

The primary focus of in-river surveys along the Murray River is on the sediments in the zone immediately beneath the river-bed, where a conductive response is commonly interpreted as a potential source of saline groundwater discharge into the river. Each of the three techniques resolved a similar riverbed conductivity structure and identified gaining sections, suggesting that all three could be used to map the location of sources of salt flux into the river. Although it was not possible to map water depth during the acquisition of the FDHEM data set, this was not regarded as a significant impediment to its wider application unless greater precision was required, such as when the effectiveness of engineered salinity remediation schemes is being evaluated.

The in-stream environment is sampled at intervals ranging from 3 to 20 m, with the highest lateral and vertical resolution obtained with the "ground" techniques. The ground-based in-stream methods provide information from near the river surface to depths of between 10 and 40 m below the surface. However, they are limited by their depth of penetration, making it difficult to effectively assess how the river and water in the underlying saturated sediments might interact with deeper, more regional groundwater systems. In contrast, the helicopter EM system provides information to a greater depth, and it has the added advantage of being able to readily acquire additional conductivity information along adjacent riverbanks and floodplains, thereby helping to elucidate processes linking the river and adjacent areas.

Ultimately the choice of technology to inform understanding of hydrogeological processes is dependent on a large number of factors, including (but not limited to) the resolution required for a given application, depth of investigation needed, rate of data acquisition, river conditions, and finally cost.

Chapter 3

The importance of the loss tangent and wavenumber: Implications for velocity and skin depth of low-frequency GPR and high-frequency EMI surveys

M. A. Hatch, G. Heinson, T. Munday, S. Thiel, K. Lawrie, J. Clarke, P. Mill

Geology and Geophysics, School of Earth and Environmental Sciences
University of Adelaide, Adelaide, SA 5005 Australia

Text in manuscript

STATEMENT OF AUTHORSHIP

The importance of the loss tangent and wavenumber: Implications for velocity and skin depth of low-frequency GPR and high-frequency EMI surveys

Text in manuscript

Hatch, M. A. (Candidate)
Developed concepts, wrote manuscript.

I hereby certify that the statement of contribution is accurate

Signed ... .*Date* 27 March 2011

Heinson, G.
Contributed to planning of article and provided critical evaluation

I hereby certify that the statement of contribution is accurate and I give permission for the inclusion of the paper in the thesis

Signed . .....*Date* 28/3/2011

Munday T.
Contributed to planning of article and provided critical evaluation.

I hereby certify that the statement of contribution is accurate and I give permission for the inclusion of the paper in the thesis

Signed .. ..*Date* 27th March 2011

Thiel, S.
Provided critical evaluation

I hereby certify that the statement of contribution is accurate and I give permission for the inclusion of the paper in the thesis

Signed ....*Date* 28/03/2011

Lawrie, K.
Provided funding for project and initial motivation for work to be performed.

I hereby certify that the statement of contribution is accurate and I give permission for the inclusion of the paper in the thesis

Signed ..... *Date* 28/3/11

Clarke, J.
Assisted with TEM data collection and initial discussions on data interpretation.

I hereby certify that the statement of contribution is accurate and I give permission for the inclusion of the paper in the thesis he

Signed ..... *Date* 28/3/11

Mill, P.
Collected GPR data for project and initial discussions on GPR data processing.

I hereby certify that the statement of contribution is accurate and I give permission for the inclusion of the paper in the thesis

Signed …… *Date…27 March 2011…*

3 THE IMPORTANCE OF THE LOSS TANGENT AND WAVENUMBER: IMPLICATIONS FOR VELOCITY AND SKIN DEPTH OF LOW-FREQUENCY GPR AND HIGH-FREQUENCY EMI SURVEYS

3.1 Summary

The full solution for the wavenumber equation in electromagnetic (EM) theory is available, but not routinely used when processing ground penetrating radar (GPR) data, or data from inductive EM (EMI) techniques. The wavenumber approach is important as it is used for the development of simple, but important, concepts such as skin depth and phase velocity, as well as being the basis for more complete interpretation of EM data sets. Approximations that make the solution simpler are common, and sufficiently accurate, provided that the underlying assumptions are not grossly violated. With the advent of lower-frequency GPR systems (25 MHz and below) and higher-frequency EMI systems (greater than 100 kHz) such approximations need to be re-examined. This paper reviews the full wavenumber expression and then compares phase velocity and skin depth equations based on approximations with equations for the same parameters based on the full solution. This comparison allows the conditions under which the assumptions are valid to be defined. For GPR surveys conducted under transition band conditions the full solution of the wavenumber equation may be used to more accurately calculate GPR phase velocity, so that depths to features may be estimated correctly. Information about the conductivity structure of the subsurface needs to be incorporated into the phase velocity calculation. Similarly, for high-frequency EMI surveys it becomes necessary to use information about the dielectric structure of the ground so that skin depths may be correctly calculated. The implications for further processing of both GPR and EMI survey data are important, as inclusion of this type of information may improve resolution of near-surface features.

3.2 Introduction

Ground penetrating radar (GPR) systems have been used routinely since the 1980's to image mostly electrically resistive geological terrains at relatively high frequencies (typically greater than 100 MHz). Applications include geological characterisation, including depth to bedrock, geomorphic characterisation, and the study of glacial environments (Davis and Annan, 1989; Nobes, 1999; Nobes et al., 2001; Taurisano et al., 2006; Barrett et al., 2008); civil engineering studies investigating the location of buried utilities and quality assessment of

concrete, etc. (Mellett, 1995; Robert, 1998; Grandjean et al., 2000); and aquifer characterisation in hydrogeological studies (al Hagrey and Muller, 2000; Ezzy et al., 2003; Brosten et al., 2009; Sassen et al., 2009). New GPR systems have been designed that use lower frequencies (10 MHz to 100 MHz) in an attempt to image deeper (Davis and Annan, 1989; Jol et al., 2002; Tallini et al., 2006; Tsoflias and Becker, 2008; Zeng et al., 2008; Franke and Utsi, 2009).

Electromagnetic induction (EMI) based conductivity surveys have been run routinely since Cagniard (1953) described the magneto-telluric method and Geonics introduced the VLF method in the mid 1960's (Paterson and Ronka, 1971). McNeill (1980) recognised the need for an EMI instrument that operated at typical engineering depths. New near-surface EMI systems are being designed to acquire the shallowest data possible and these systems operate at higher frequencies.

Several ground based frequency-domain electromagnetic (FDEM) systems are available that collect data at nearly 100 kHz (e.g. Aerophex Sensor Technology's Gem-2 system (http://www.aeroquestsensortech.com)). For airborne FDEM systems designed for shallow resolution, the highest frequency is approximately 140 kHz (e.g. Fugro Airborne Survey's RESOLVE system (Fitzpatrick et al., 2007b)). Radiomagnetotelluric (RMT) systems collect data at frequencies up to 250 kHz (Bastani and Pedersen, 2001; Kalscheuer et al., 2008). Time-domain electromagnetic (TEM) systems designed for near-surface characterisation, such as Zonge Engineering's NanoTEM system (Hatch et al., 2002) use a very short transmitter turnoff ramp (typically less than 2 microseconds) and collect data using a sampling rate of 1.2 microseconds. Assuming that the Nyquist frequency for this sampling rate is similar to the peak frequency of the system, this translates to a peak frequency of 416 kHz. The development of the VETEM system (Stewart et al., 1994; Pellerin et al., 1995) recognises that in order to characterise the very near surface, i.e. to 1 to 2 m depth, it is necessary to collect very early time TEM data (or very high frequency FDEM data) and that to process these data both conduction as well as displacement currents need to be accounted for. As hardware improves, it is anticipated that data will be collected at even higher frequencies (Sørensen et al., 2005).

For GPR, the equations that define phase velocity and attenuation (based on the wavenumber equation) are simplified when the system is operated in conditions where the combination of system frequency, ground dielectric permittivity and ground resistivity are high enough to allow the effects of conduction currents to be ignored (i.e. low-loss conditions). Similarly, for EMI techniques the equations that define skin depth and phase velocity (again based on the wavenumber equation) are much simplified when the system is operated in conditions where the combination of system frequency, ground dielectric permittivity and ground

resistivity are low enough that displacement current effects may be ignored (i.e. quasi-static conditions). The criterion for whether a GPR system is running under low-loss conditions, or an EMI system is running under quasi-static conditions, is dependent on whether the loss tangent (the ratio between the imaginary component and the real component of the wavenumber equation) is much less than 1 for the GPR system (Davis and Annan, 1989; Reynolds, 1997) or much greater than 1 for the EMI system (Ward and Hohmann, 1991; Christiansen et al., 2009).

Giroux and Chouteau (2010) discuss limitations in the use of the low-loss approximation in calculating dielectric permittivity and water content derived from GPR data. Huang and Fraser (2001; 2002) and Yin and Hodges (2005) recognise that EMI data collected using airborne systems are potentially affected by variations in dielectric permittivity. Yin and Hodges (2005) show that AEM apparent resistivities are affected when displacement currents are not accounted for over relatively resistive ground (>1000 ohm-m) at frequencies above 10 kHz. Similarly, Huang and Fraser (2001; 2002) describe a procedure for calculating magnetic permeability and dielectric permittivity from frequency-domain AEM data and then use these estimates to improve the quality of the apparent resistivity calculations. Kalscheuer et al. (2008) show that under relatively resistive conditions the inclusion of dielectric permittivity information when inverting RMT data affects the results significantly. In mining, the Radio Imaging Method (RIM) uses electromagnetic signal in the frequency range from 2.5 kHz to 15 MHz to image variations in attenuation rates between two bore holes with separation potentially greater than 100 m (Mahrer, 1995). It has been used to characterise coal seam beds (Stolarczyk et al., 1988) and conductive ore bodies (Thomson et al., 1992; Fullagar et al., 2000; Johnson et al., 2001). It is recognised that in this frequency range, RIM surveys may be operating under conditions where conduction currents or displacement currents may predominate, or where conditions are mixed. This does not appear to affect the interpretation of RIM results, as it is relative attenuation rates within a given survey area that is correlated with conductivity, and therefore the locations of faults and/or ore bodies. Johnson et al. (2001) explicitly model both conduction and displacement currents in an effort to improve results.

In this paper we review the derivation of the full solution of the wavenumber equation and the low-loss and quasi-static simplifications. We then look at how solutions to the wavenumber equation are used to estimate phase velocity and skin depth for simple EMI and GPR problems, and define ground conditions under which the low-loss and quasi-static equations may be used. Using this approach we define the transition band between the two methods where results from each may be improved by using full-solution formulations. The consequences of deriving information about the near surface are considered using hypothetical field examples, comparing

calculated parameters based on the approximations and the full solution. Finally, results are shown from a field example where coincident sets of low-frequency GPR and high-resolution TEM were collected over the same traverse and processed together.

3.3 Theoretical background

The solution for electric field strength, using Maxwell's equations and the constitutive relations, assuming plane wave, sinusoidal time-dependence in a homogeneous, isotropic earth (e.g. Ward and Hohmann (1991)) is:

$$E = E_0 e^{-i(kz-\omega t)} \tag{3.1}$$

where E is the electric field strength vector (V/m), E_0 is the initial electric field magnitude, z is depth (m), t is time (s), and ω is angular frequency (given by $2\pi f$, where f is frequency). The wavenumber, k, is defined as:

$$k = (\omega^2 \varepsilon\mu - i\omega\mu\sigma)^{\frac{1}{2}} = \beta - i\alpha \tag{3.2}$$

where μ is magnetic permeability (H/m), σ is electrical conductivity (S/m), and ε is dielectric permittivity (F/m). For convenience we note that ε is often expressed as $\varepsilon_0\varepsilon_r$, where ε_0 is the permittivity of free space (8.854 x 10^{-12} F/m) and ε_r is the (dimensionless) relative dielectric permittivity. For the remainder of this paper we refer to the relative dielectric permittivity as permittivity. Similarly, μ is often expressed as $\mu_0\mu_r$, where μ_0 is the magnetic permeability of free space (4π x 10^{-7} H/m) and μ_r is relative magnetic permeability. As μ_r is very close to one for many near-surface materials (Lazaro-Mancilla and Gomez-Trevino, 2000), we will assume that to be the case for this paper.

The terms α and β are the attenuation and phase terms (von Hippel, 1954) that need to be determined. Usually, simplifying assumptions are made to solve for α and β. For GPR, under low-loss conditions it is assumed that conduction currents are small, and therefore the $i\omega\mu\sigma$ term may be ignored (Ward and Hohmann, 1991; Annan, 2005a). Similarly for FDEM and TEM, Equation 3.2 is simplified by assuming that displacement currents are small and therefore the $\omega^2\varepsilon\mu$ term may be ignored (Ward and Hohmann, 1991; Christiansen et al., 2009). We will look at each of these separately and then present the more general solution.

For GPR, it is convenient to restate the square of the wavenumber as:
$k^2 = \mu\varepsilon\omega^2(1 - i\frac{\sigma}{\varepsilon\omega})$. The loss tangent is defined as:

$$\tan\theta = \frac{\sigma}{\varepsilon\omega} \tag{3.3}$$

When this is sufficiently small (i.e. $\tan\theta \ll 1$), the imaginary term approaches zero, and $k \cong \omega\sqrt{\mu\varepsilon}$. As this has no imaginary component, we know that $\alpha \cong 0$ (i.e. that there is very

little attenuation) and that $\beta \cong \omega\sqrt{\mu\varepsilon}$. These conditions are generally called low-loss and are discussed in more detail in this paper.

In general, phase velocity is defined as the velocity of any given phase (such as the trough) of a wave (Sheriff, 2002) and is given by: $v = \frac{\omega}{\beta}$ (Ward and Hohmann, 1991). For the low-loss case this reduces to the standard definition for phase velocity in GPR:

$$v = \frac{\omega}{\beta} = \frac{1}{\sqrt{\mu\varepsilon}} \tag{3.4}$$

The advantage of this assumption is that: a) the expressions for the wavenumber and phase velocity are simple; and b) the conductivity term (and therefore knowledge about the conductivity distribution in the earth) is not required.

For EMI techniques, it is convenient to write the square of the wavenumber as: $k^2 = \mu\sigma\omega(\frac{\omega\varepsilon}{\sigma} - i)$. The term $\frac{\omega\varepsilon}{\sigma}$ is the reciprocal of the loss tangent. In this case, as the loss tangent gets very large, the real part of the argument tends to zero, $k = \left(\frac{\omega\mu\sigma}{2}\right)^{\frac{1}{2}}(1 - i)$ and $\alpha = \beta = \left(\frac{\omega\mu\sigma}{2}\right)^{\frac{1}{2}}$.

Skin depth (δ) is defined as the depth at which the signal level drops to e^{-1} of its initial value. This occurs at the depth $1/\alpha$. From this analysis the standard definition of skin depth is given as:

$$\delta = \frac{1}{\alpha} = \sqrt{\frac{2}{\omega\mu\sigma}} \tag{3.5}$$

From the definition of phase velocity we also get:

$$v = \frac{\omega}{\beta} = \sqrt{\frac{2\omega}{\mu\sigma}} \tag{3.6}$$

By simplifying in this way we are able to define skin depth and phase velocity without having to know anything about the dielectric permittivity parameter (and therefore about the dielectric permittivity distribution in the earth).

As the frequency bandwidth of GPR and EMI techniques is extended there are situations where the system is operating in the transition band between low-loss and quasi-static conditions (i.e. where the loss tangent is no longer <<1 for the low-loss case, or >>1 for the quasi-static case). It then becomes necessary to use the more complete solution of the wavenumber equation to calculate appropriate values for skin depths and phase velocities. Stratton (1941), Al Hagrey and Muller (2000), Santamarina et al. (2005), Zeng et al. (2008), Kalscheuer et al. (2008), Blindow (2009) and, Giroux and Chouteau (2010) give the following solution:

$$\alpha = \omega \sqrt{\frac{\mu\varepsilon}{2}\sqrt{\left(1+\frac{\sigma^2}{\varepsilon^2\omega^2}\right)}-1} \quad (3.7)$$

and

$$\beta = \omega \sqrt{\frac{\mu\varepsilon}{2}\sqrt{\left(1+\frac{\sigma^2}{\varepsilon^2\omega^2}\right)}+1} \quad (3.8)$$

Phase velocity and skin depth are now given as:

$$v = \frac{\omega}{\beta} = \frac{1}{\sqrt{\frac{\mu\varepsilon}{2}\sqrt{\left(1+\frac{\sigma^2}{\varepsilon^2\omega^2}\right)}+1}} \quad (3.9)$$

$$\delta = \frac{1}{\alpha} = \frac{1}{\omega\sqrt{\frac{\mu\varepsilon}{2}\sqrt{\left(1+\frac{\sigma^2}{\varepsilon^2\omega^2}\right)}-1}} \quad (3.10)$$

In examining these equations it is apparent that knowledge about both the conductivity structure and permittivity structure of a survey area are needed to fully solve for phase velocity and skin depth.

3.3.1 Dispersion considerations

Up to now we have not included the likelihood that μ, ε and σ change with frequency and are therefore complex and dispersive. This is important as values for permittivity and conductivity given in most tables are based on measurements made at a single frequency or over a small range of frequencies. Fuller and Ward (1970), Olhoeft (1979a), Olhoeft (1998), Annan (1996) and others cover the issue of permittivity, conductivity and magnetic permeability variation with frequency in some detail so we review only a few points here.

Approaches like the Debye model (Debye, 1929) and the Cole-Cole model (Cole and Cole, 1941) for dielectric permittivity and the Pelton extension of the Cole-Cole model for conductivity (Pelton et al., 1978) allow researchers to understand how various electrical parameters change with frequency. All of these models require relatively good estimates of both the high-frequency and the DC limit for permittivity or conductivity as well as good estimates of the decay time constant to accurately predict permittivity or conductivity over a range of frequencies. Knight and Nur (1987) and Wensink (1993) measure dielectric behaviour over a large range of frequencies for a number of sandstones (Knight and Nur, 1987), and for a number of soils (Wensink, 1993), varying water content as well. Both conclude that permittivity varies with frequency and water content, although the mechanisms that are invoked to explain the variation are different. Again, the relationships described in these studies indicate general

behaviour of certain types of rocks, but are specifically useful only for the samples tested. It is important to understand that the effects that contribute to a permittivity value at a given frequency are cumulative, with dielectric contribution from higher frequency mechanisms adding to those at lower frequencies (von Hippel, 1954). This is consistent with the general observation that permittivity decreases with increasing frequency (Wensink, 1993; Santamarina et al., 2005).

More complete expressions for the loss tangent, α, and β, may be derived using complex terms for dielectric permittivity, magnetic permeability and/or conductivity. These can only be used when both the real and imaginary components of conductivity and dielectric permittivity are known, at the frequency of interest. As the frequency variation inherent in conductivity, dielectric permittivity and magnetic permeability are not well enough understood, for the purposes of this paper we continue to use the simpler expressions for the wavenumber (Equations 3.7 and 3.8) as the basis to derive other parameters, using only the available information at the frequency collected.

As a first pass, i.e. without considering the need to incorporate the imaginary parts of the relevant terms, it is worth commenting on the extent to which phase velocity and skin depth may be affected if dispersion is not accounted for. For the GPR case, it was noted earlier in this section that permittivity is usually inversely related to frequency. Examination of Equation 3.4 (phase velocity under low loss conditions) suggests that if estimates of dielectric permittivity are made in the lab at a relatively high frequency (e.g. at >100 MHz) and field measurements are made at lower frequencies (e.g. at <50 MHz), it is likely that the permittivity estimate for the field work will be too low, and therefore phase velocity and depth to features in a GPR section will be overestimated. Similarly, for the quasi-static case, Fuller and Ward (1970) review conductivity variation with frequency for “wet” and “dry” samples over the frequency range from 1 Hz to 1 MHz. They state that for wet samples, conductivity generally changes little with frequency (less than one order of magnitude), and for dry samples conductivity shows much more dispersive behaviour, and is generally inversely proportional to frequency. Nevertheless, over the range of frequencies that field measurements are made at it is likely that there would be little effect on the estimation of skin depth in either case.

3.4 Theoretical implications

3.4.1 Bounds: Quasi-static, low-loss and the transition band

Based on Maxwell’s equations EM fields propagate due to a combination of conduction and displacement currents. The practical problem is then to define the conditions under which

one or the other dominates, and define the transition band so that the correct equations may be used to define ground conditions. There are a number of ways to evaluate whether the quasi-static approximation or the low-loss approximation is appropriate or when the full solution is appropriate because we are in the transition band. We examine three here, starting with the most strict.

By examining when $\alpha \approx \beta$ (i.e. $\frac{\alpha}{\beta} \approx 1$) or when $\alpha \approx 0$ (i.e. $\frac{\alpha}{\beta} \approx 0$), and comparing these conditions against loss tangent, a range of loss tangents may be defined where displacement currents dominate ($\frac{\alpha}{\beta} \approx 1$) and where conduction currents dominate ($\frac{\alpha}{\beta} \approx 0$). In Figure 3.1, α and β are calculated using a frequency of 100 MHz, a permittivity of 5, and conductivity ranging from 0.1 mS/m to 100,000 mS/m (10,000 to 0.01 ohm-m). The ratio $\frac{\alpha}{\beta}$ is then plotted against the loss tangent calculated for the same conditions. These results are the same when conductivity and frequency are fixed and permittivity is varied, or when conductivity and permittivity are fixed and frequency is varied, as the loss tangent is proportional to all three variables. As $\frac{\alpha}{\beta}$ is asymptotic to 1, under quasi-static conditions, and 0 under low-loss conditions, it is necessary to set a limit that defines when they are equal. In this case we have defined "equal" as when the difference is ≤0.5%. For quasi-static conditions $\frac{\alpha}{\beta} \geq 0.995$, when the loss tangent is ≥216. This zone is indicated with the lighter shading on the right side of the plot in Figure 3.1. For low-loss conditions $\frac{\alpha}{\beta} \leq 0.005$ when the loss tangent is ≤0.01 (the darker shaded area on the left side of the plot in Figure 3.1). The unshaded zone in the centre of the plot is the transition band between low-loss and quasi-static conditions, where neither displacement nor conductive currents dominate.

These loss tangent limits define a large transition band and are somewhat unrealistic when error levels for parameters such as phase velocity are examined. In Figure 3.2, we compare the low-loss velocity ($V_{lowloss}$) given in Equation 3.4, and the quasi-static velocity (V_{qs}) given in Equation 3.6, with the complete expression for the velocity (V_{true}) presented in Equation 3.9. For the quasi-static case V_{true}/V_{qs} is calculated and is expected to approach 1 when conditions are dominated by conduction currents. For the low-loss case $V_{true}/V_{lowloss}$ is calculated and is expected to approach 1 when conditions are dominated by displacement currents. As the

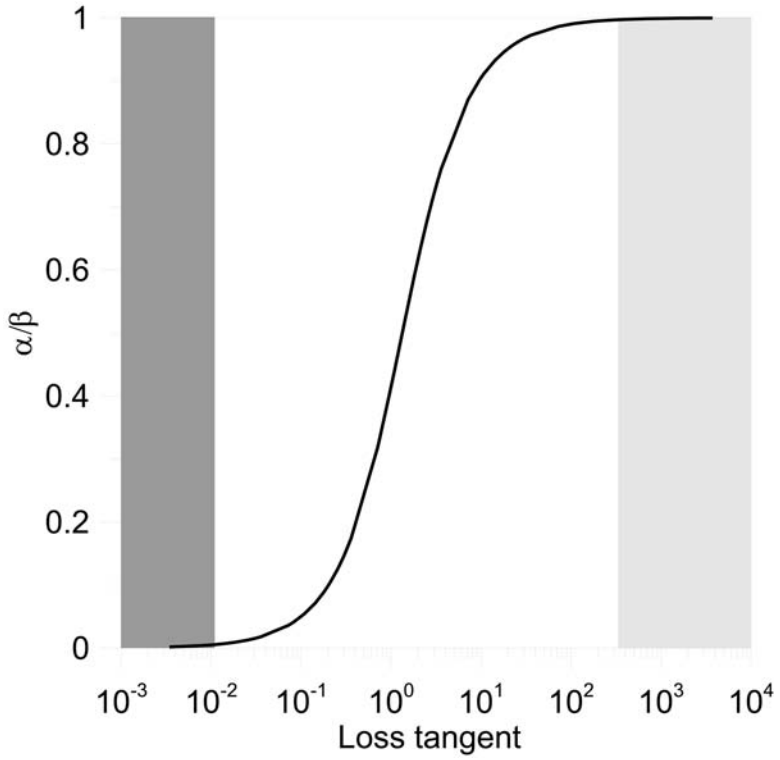

Figure 3.1. Comparison of the ratio of the attenuation term and the phase term of the wavenumber to loss tangent. When $\alpha/\beta \rightarrow 1$, $\alpha \rightarrow \beta$ and conditions are dominated by conduction currents. When $\alpha/\beta \rightarrow 0$, $\alpha \rightarrow 0$ and conditions are dominated by displacement currents. The darker shaded area on the left side of the plot indicates the combinations of conductivity, frequency and permittivity for which the loss tangent is <0.01, and conditions are predominantly low-loss (as defined in the text). The lightly shaded area on the right side of the plot indicates the combinations of conductivity, frequency and permittivity for which the loss tangent is >216 and conditions are predominantly quasi-static (as defined in the text).

results from the approximations, and the exact solution approach each other asymptotically, we again state that the results are "equal" when they vary by ≤0.5% and are "reasonable" when they vary by ≤5% (this 5% level is arbitrary, and represents only a reasonable error estimate for velocity). The effect on the loss tangent when frequency, conductivity or dielectric permittivity is varied is the same, so the results shown in Figure 3.2 are the same when varying any of these parameters.

V_{qs} is within 0.5% of V_{true} when loss-tangent ≥ 103 and is within 5% when loss tangent ≥ 9.7. $V_{lowloss}$ is within 0.5% of V_{true} when loss tangent ≤ 0.20 and is within 5% when loss tangent ≤ 0.69. Conditions for quasi-static and low-loss are not symmetrical around loss tangent = 1, as might be expected. Based on these distinctions, five zones are shown in Figure 3.2. In Zone 1

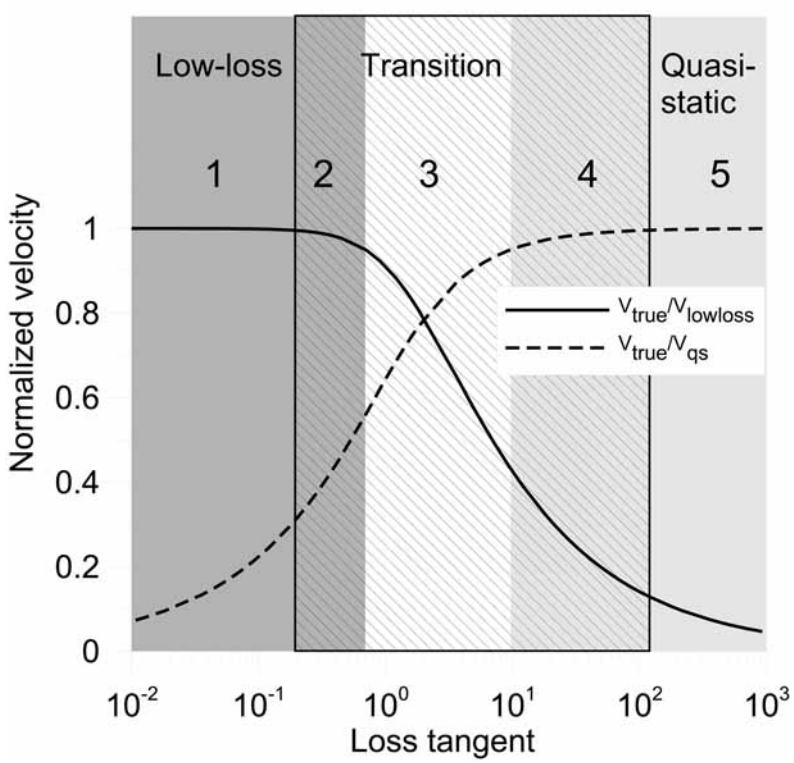

Figure 3.2. Comparison of approximate low-loss and quasi-static velocities (Equations 3.4 and 3.6) to true values (Equation 3.9). Loss tangent increases with decreasing frequency and dielectric permittivity and with increasing conductivity. Parameter ranges where low-loss estimate error is less than 5% are highlighted in dark grey. Parameter ranges where quasi-static estimate error is less than 5% are highlighted in light grey. The boxed, cross hatched area shows the range of parameters where approximate solutions deviate from exact solutions by 0.5% or more. The numbers at the top of the plot define zones where low-loss conditions prevail, where quasi-static conditions prevail, and where transition band conditions prevail, as defined in the text.

the loss tangent is ≤ 0.20 so conditions are such that displacement currents are the main energy propagation mechanism, with little propagation due to conduction currents. Under these conditions GPR would work well, and EMI techniques would not. The low-loss phase velocity equation (Equation 3.4) may be used to estimate phase velocity. In Zone 2 the loss tangent is ≤ 0.69 but is >0.20. This is the beginning of the transition band where neither displacement nor conduction currents dominate, and the low loss phase velocity equation (Equation 3.4) may still be used to estimate phase velocity, but with an error of less than 5%. GPR will work better under these conditions than an EMI technique. Zone 3 is the transition band (0.69 < loss tangent < 9.7), where the full-solution phase velocity (Equation 3.9) should be used to calculate phase velocity. Zone 4 is the other side of the transition band where the loss tangent is ≥ 9.7 but is < 103. Under these conditions the error in using Equation 3.6 for the quasi-static phase velocity is less than 5%, and thus Equation 3.6 or 3.9 may be used. An EMI technique will work better under

these conditions than GPR. Zone 5 is where conduction currents dominate and dielectric currents are minimal. In this zone, the loss tangent ≥ 103 and Equation 3.6 may be used to estimate phase velocity. EMI techniques would work well under these conditions but GPR would not.

Figure 3.3 is similar to Figure 3.2, except that the responses of each of the input parameters to the loss tangent have been plotted separately against V_{true}/V_{qs} and $V_{true}/V_{lowloss}$. The 0.5% and 5% error rules from the phase velocity analysis are used here for analysis purposes. For Figure 3.3a, permittivity is fixed at 5, frequency is fixed at 25 MHz and conductivity is allowed to vary. Under these conditions, displacement currents dominate when the conductivity is less than 1.4 mS/m (>715 ohm-m) and conduction currents dominate when the conductivity is greater than 715 mS/m (<1.4 ohm-m). For Figure 3.3b, the permittivity is fixed at 5, the conductivity is fixed at 10 mS/m (100 ohm-m) and the frequency is allowed to vary. Under these conditions, displacement currents dominate for frequencies greater than $1.8x10^8$ Hz and conduction currents dominate for frequencies less than $3.5x10^5$ Hz. For Figure 3.3c, the conductivity is fixed at 10 mS/m (100 ohm-m), the frequency is set at 25 MHz and the permittivity is allowed to vary. Under these conditions, displacement currents dominate for permittivities greater than 36 and conduction currents dominate for permittivities less than 0.07. The same five zones defined for Figure 3.2 are shown on each of the plots in Figure 3.3. The arrows at the base of each plot show the direction in which the loss tangent increases.

An alternative way to look at these results is to plot two of the variables against each other while fixing the third variable and then map out the three major zones of behaviour (i.e. purely dielectric, purely conductive and the transition band) based on the loss tangent. In Figure 3.4 permittivity is fixed to two different levels: to 5 for Figure 3.4a and 40 for Figure 3.4b, and the other two parameters are allowed to vary. Annan (2005a) gives ranges of conductivities and permittivities for a number of materials. Permittivities for clays range from 5 to 40 (and conductivities range from 2 to 1000 mS/m). These permittivity values are used as the minimum comparison levels for our analyses. In Figure 3.4 conductivities range from 0.001 mS/m (1M ohm-m) to 1000 mS/m (1 ohm-m), and frequencies range from 1000 Hz to 1000 MHz. In each plot the solid sloped line indicates the range of conductivities and frequencies for which the loss tangent is 1. The darker shaded area at the bottom of each plot indicates the combinations of conductivity and frequency for which the loss tangent is ≤0.2 (i.e. the 0.5% error level for low-loss conditions based on phase velocity calculations) and the lighter shaded area at the top of each

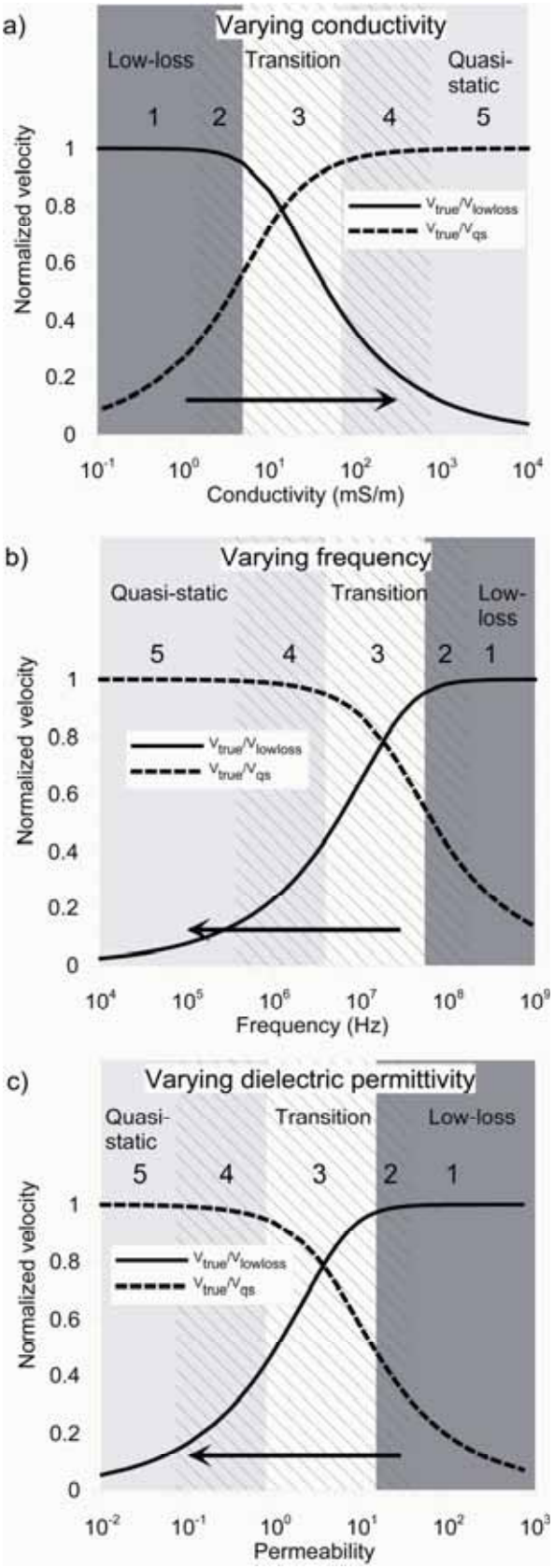

Figure 3.3. Comparison of approximate low-loss and quasi-static velocities (Equations 3.4 and 3.6) to true values (Equation 3.9). a) permittivity is fixed at 5, and frequency is fixed at 25 MHz. Conductivity is allowed to vary. b) permittivity is fixed at 5, and conductivity is fixed at 10mS/m (100 ohm-m). Frequency is allowed to vary. c) conductivity is fixed at 10 mS/m (100 ohm-m), and frequency is fixed at 25 MHz. Permittivity is allowed to vary. The black arrows on each plot show the direction in which the loss tangent increases. Parameter ranges where low-loss estimate error is less than 5% are highlighted in dark grey. Parameter ranges where quasi-static estimate error is less than 5% are highlighted in light grey. Cross hatched area shows range of parameters where approximate solutions deviate from exact solutions by 0.5% or more. The numbers at the top of each plot define zones where low-loss conditions prevail, where quasi-static conditions prevail, and where transition band conditions prevail, as defined in the text.

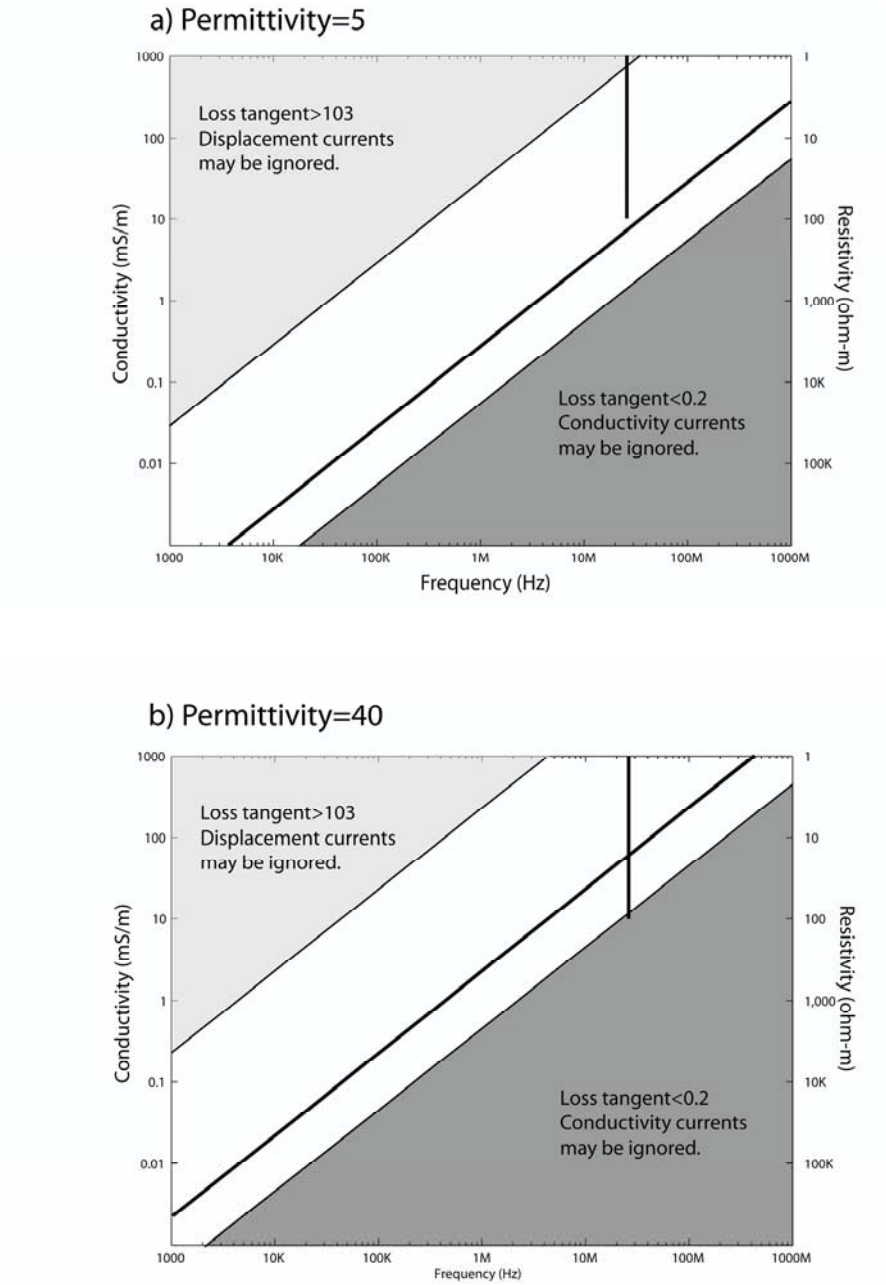

Figure 3.4. Loss tangent calculated for conductivities ranging from 0.001 mS/m (1M ohm-m) to 1000 mS/m (1 ohm-m) and frequencies ranging from 1000 Hz to 1000 MHz. In a) dielectric permittivity is set to 5, and in b) dielectric permittivity is set to 40. The lightly shaded area at the top of each plot indicates the combinations of conductivity and frequency for which the loss tangent is >103 and conditions are predominantly quasi-static. The darker shaded area at the bottom indicates the combinations of conductivity and frequency for which the loss tangent is <0.2 and conditions are predominantly low-loss. The unshaded zone in the centre of each plot is the transition band. The sloped solid lines indicate conductivities and frequencies for which the loss tangent =1. The heavy vertical lines indicate test conditions described in text (i.e. f=25 MHz, conductivities range from 10 to 1000 mS/m).

plot highlights the combinations of conductivity and frequency for which the loss tangent is ≥103 (i.e. the 0.5% error level for quasi-static conditions based on phase velocity calculations).

If, for example, we wish to determine the feasibility of using a 25 MHz GPR system over ground with permittivity ranging from 5 to 40, and conductivity ranging from 10 to 1000 mS/m, examination of the solid vertical lines in Figures 3.4a and 3.4b show that low-loss conditions are only met when the permittivity is 40, and conductivity is less than approximately 11 mS/m (>91 ohm-m). The system would be operating predominantly in the transition band. Close examination of Figure 3.4a shows that when the permittivity is 5, the conductivity must be less than 715 mS/m (>1.4 ohm-m) to be in the transition band. For most of the conditions given for this survey, using the equation for phase velocity based on the low-loss approximation to translate times to depths would not be appropriate. It would be necessary to collect information about the shallow conductivity structure of the ground and use Equation 3.9 to solve for phase velocities.

3.4.2 Transition band behaviour

Under low-loss conditions EM signal travels through the earth over distances that may be measured in multiples of wavelength. There is little signal attenuation due to conductive losses and the skin depth is much larger than the wavelength. Signal travels relatively large distances (as measured in wavelengths) to reflective boundaries where some of the energy is transmitted through the boundary and some returns to the surface to be recorded at the GPR receiver. Under these conditions the attenuation term, and therefore conductivity, is relatively unimportant. Under quasi-static conditions EM signal travels through the earth over distances that are less than one wavelength, signal attenuation is quite large due to conductive losses, and the skin depth is less than the wavelength. The attenuation term and conductivity are relatively important. The signal that is recorded is not a reflection, but is usually a secondary magnetic field measurement at a given frequency that is proportional to the ground conductivity. In the transition band both of these effects are observed to varying degrees.

It is apparent that the attenuation constant is important in determining what type of information is available from the electric field. To illustrate the significance of this, two measures of signal attenuation have been calculated and are presented in Figure 3.5. First, the signal attenuation at a depth of one wavelength has been calculated for a range of conditions. Second, the number of wavelengths per skin depth has also been calculated. Figure 3.5a presents the general case, where these two parameters are plotted against loss tangent. For Figure 3.5b permittivity is fixed at 5, and for Figure 3.5c is fixed at 40 (the system frequency is 25 MHz). In

each case, the loss tangent and conductivity endpoints are based on the 0.5% $\frac{\alpha}{\beta}$ error levels defined earlier. For Figure 3.5a, the loss tangent low-loss limit is 0.01 and the quasi-static limit is 216; for Figure 3.5b, the conductivity low-loss limit is approximately 0.07 mS/m (14,400 ohm-m) and the quasi-static limit is approximately 1500 mS/m (0.67 ohm-m); and for Figure 3.5c, the conductivity low-loss limit is approximately 0.56 mS/m (1790 ohm-m) and the quasi-static limit is approximately 12,000 mS/m (0.08 ohm-m).

The attenuation constant for each set of conditions is calculated using Equation 3.7. Wavelength is given by $\lambda = v/f$ where velocity is defined by Equation 3.9 and f is the system frequency. The signal magnitude at one wavelength depth is calculated using the real part of Equation 3.1 (E_0 is set to 1 V/m), setting $z = \lambda$.

The shading scheme used in Figure 3.2 and the phase velocity error levels are used to highlight areas where conduction currents dominate, where displacement currents dominate, and the transition bands. Loss tangent and conductivities at which the signal level has attenuated to 1% of E_0 is indicated in each plot. This occurs when the loss tangent is greater than 3.2. For a permittivity of 5, this translates to conductivity greater than 22 mS/m (<45.5 ohm-m), and for a permittivity of 40 this translates to conductivity greater than 176 mS/m (<5.7 ohm-m).

Figure 3.5 highlights that for a GPR survey, as the loss tangent gets larger (in this case as the ground becomes more conductive) and approaches the values where quasi-static conditions dominate, signal attenuation is significant. Under these conditions the usefulness of a GPR survey becomes significantly less.

3.5 Results

3.5.1 GPR: Phase velocity

For a GPR survey run over relatively conductive soil with a permittivity of 16, i.e. average "soil" (Reynolds, 1997) the standard phase velocity calculated using Equation 3.4 is 7.5×10^7 m/s. If the system frequency is 25 MHz and the ground conductivity is 100 mS/m (10 ohm-m), the loss tangent is 4.5, and data collected for this survey would be in the transition band. Therefore, the more accurate phase velocity calculated using Equation 3.9 is 4.5×10^7 m/s, 60% of the low-loss estimate. Using the incorrect low-loss value for phase velocity would result in large errors when estimating depths in this survey. This sort of error would most likely be noticed if velocities were measured during the survey using common midpoint (CMP) gathers or measuring arrival times from subsurface features at known depths.

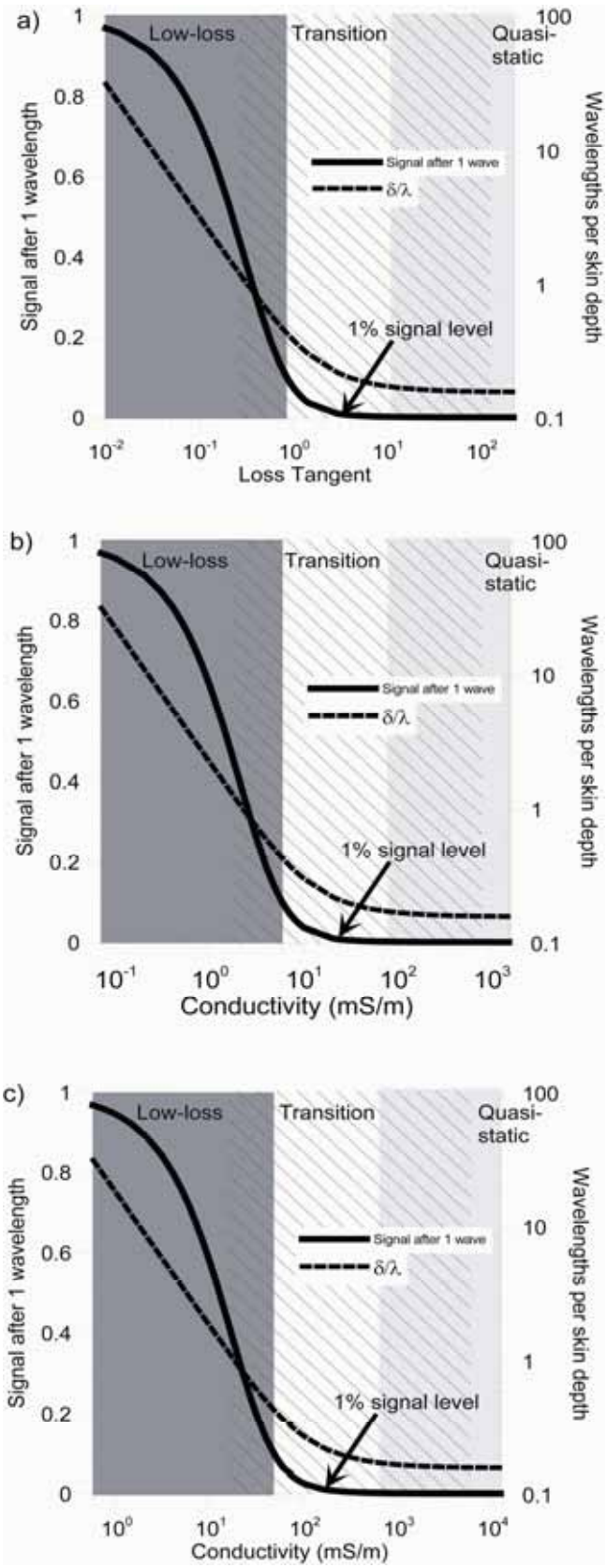

Figure 3.5. a) relative signal strength after one wavelength and wavelengths per skin depth plotted against loss tangent. b) relative signal strength after one wavelength and wavelengths/skin depth plotted against conductivity. Permittivity = 5, f = 25 MHz. c) relative signal strength after one wavelength and wavelengths/skin depth plotted against conductivity. Permittivity = 40, f = 25 MHz. Shading scheme for all plots is the same as in Figure 3.2.

.

3.5.2 EMI: Skin depth and phase velocity

Kalscheuer et al. (2008) show that under relatively resistive conditions the inclusion of permittivity information when inverting RMT data affects the results significantly. This can be shown in the context of this paper when loss tangent, skin depth and phase velocity are calculated based on a typical scenario from their work. For Table 3.1, skin depths were compared setting the conductivity to 0.1 mS/m (10,000 ohm-m), and the permittivity to either 1 (i.e. similar to the quasi-static assumption) or 5 (i.e. typical for fractured crystalline rock) (Kalscheuer et al., 2008). Results were tested at 10 kHz and 170 kHz. For comparison purposes these scenarios were tested using both the quasi-static solution for skin depth (Equation 3.5) as well as the full solution (Equation 3.10). Not surprisingly, at 10 kHz there is very little difference between the quasi-static and the true solutions when the permittivity is 1, as the loss tangent is 180. Even when the permittivity is set to 5 the maximum difference is slightly greater than 1% (the loss tangent is 36). At 170 kHz the situation is different. When the permittivity is 1 the loss tangent is 11, and when the permittivity is 5, the loss tangent is 2, putting both cases in the transition band. While there is a 5% discrepancy between the quasi-static solution and the full solution when the permittivity is 1, when the permittivity is 5 the discrepancy is approximately 20%, emphasizing that even small errors in estimating permittivity at high frequency and resistivity can produce large differences in the quality of solutions under these conditions.

Table 3.1. Permittivity effects on RMT data.

Frequency (kHz)	ε_r	Conductivity (mS/m)	Resistivity (ohm-m)	Loss tangent	δ_{qs} (m)	δ_{true} (m)
10	1	0.1	10000	180	503.3	504.7
10	5	0.1	10000	36	503.3	510.3
170	1	0.1	10000	11	122.1	128.0
170	5	0.1	10000	2.1	122.1	153.4

3.5.3 Field example

Figure 3.6 shows a 2 km subset from a line of data run over a highly salinised floodplain along the Murray River near Mildura, Australia. These data are more thoroughly explained in Chapters 4 and 5 so will only be briefly discussed here. Three lines of coincident, towed small-loop TEM and towed 25 MHz GPR were collected during early 2008 along dirt roads running approximately north-south across the floodplains of the Murray River. The lines all started near the southern margins of salinised floodplains, ending at, or near, the southern bank of the Murray River. Parts of these lines passed near relatively fresher anabranch creeks of the Murray River,

where localised flushing of the near-surface sediments is likely (Murray Darling Basin Commission, 2003; Overton et al., 2006; Lawrie et al., 2008).

Figures 3.6a and 3.6b show the GPR data, comparing the results when standard, low-loss processing is applied to the GPR data, and when the full-solution data processing scheme based on this study is applied; Figure 3.6c shows the inverted TEM results for the same stretch of data. The processing steps for the two GPR sections are identical, until the conversion stage of time to depth. For Figure 3.6a, phase velocity is estimated using the low-loss equation (Equation 3.4), setting permittivity to 11, which gives a uniform phase velocity for this area of $9x10^7$ m/s. For Figure 3.6b, each GPR sounding is matched with its nearest TEM sounding. Phase velocities are estimated for each data sample, based on conductivity, using the full solution for the phase velocity (Equation 3.9). Phase velocity based on the direct ground-wave arrival is used for all signal arriving before the first visible reflection. GPR signal magnitudes are then placed at the correct depth using repeated applications of the two-way travel time equation (Blindow, 2009) and Snell's law, as explained in Chapter 4. The highly conductive features in the TEM section and the small breaks in the GPR data at approximately stations 10600, 10840 and 11090 are related to small bridges and culverts along the track.

The most obvious difference between Figures 3.6a and 3.6b is the vertical scale. The GPR data shown in Figure 3.6a span a total thickness of over 25 m, which does not vary. When processed using the full solution, as shown in Figure 3.6b, the depth extent is more variable, with the total thickness varying from approximately 7 to 12 m, depending on local conductivity.

Along this transect, Figures 3.6a and 3.6b would be interpreted similarly, particularly when interpretation is based on signal attenuation. It is possible to identify zones that are highly attenuated in both, interpreted as areas where groundwater is saline, as well as zones that are less attenuated, where groundwater is relatively fresh. Comparison of the vertical scale of the two plots shows that the section in Figure 3.6b bears a stronger resemblance to the TEM section than Figure 3.6a, and would be interpreted similarly. Based on the TEM (Figure 3.6c), from station 9500 to 10400 the relatively resistive surface layer is interpreted to be dry soils, above the capillary fringe (Cresswell and Shand, 2009). The thickness of the surface layer is very similar to that defined by the relatively high amplitude signal at the top of the GPR data shown in Figure 3.6b. However, significant differences are noted between it and the thickness of the same layer shown in Figure 3.6a. The signal magnitude in the GPR of the surface layer is high, suggesting

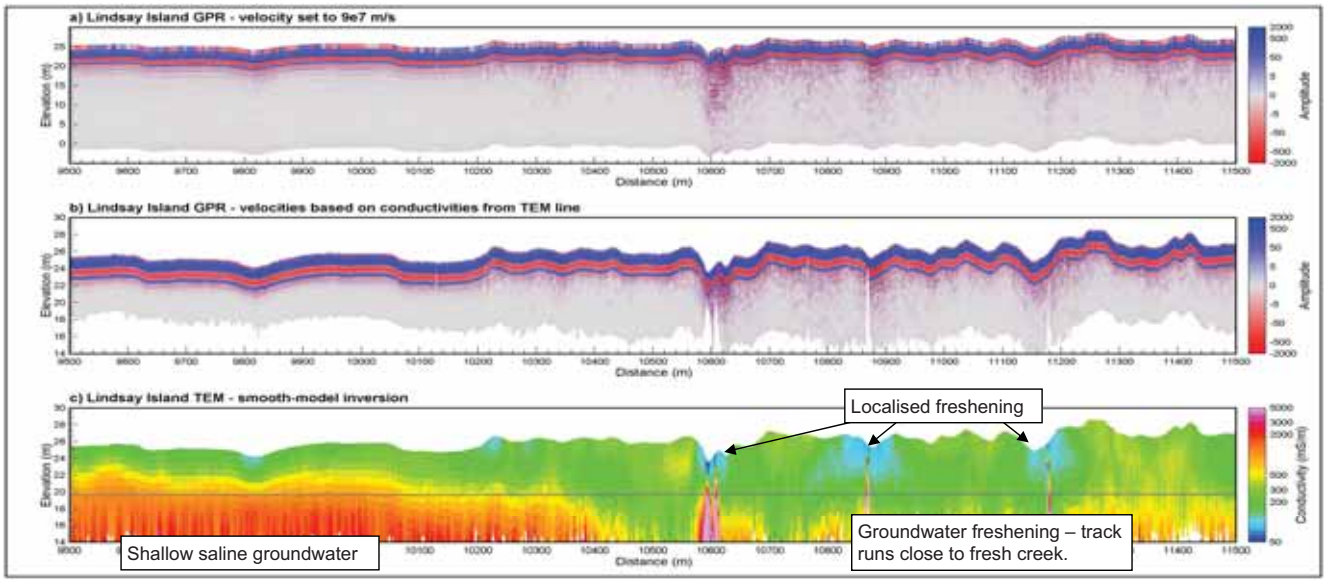

Figure 3.6. Example depth sections of GPR and towed-TEM over 2 km stretch. a) GPR data processed using low-loss assumptions and permittivity = 11. b) GPR data processed using velocities calculated based on the conductivity information from the TEM data set. c) inverted TEM data set. The vertical axis is elevation in metres. The horizontal axis is distance along profile in metres. Highly conductive features in TEM section and breaks in GPR data at approximately stations 10600, 10840 and 11090 are bridges (i.e. cultural features). Basic hydrogeological interpretation is highlighted on the TEM section. The location of the regionally determined water table is indicated with a grey line on the TEM section.

that this layer is likely to be dry. From Station 10400 to the north, this traverse runs parallel to Mullaroo Creek, a small, relatively fresh anabranch of the Murray River. The sediments along this stretch are more resistive than those seen on the southern end of this stretch, and are interpreted to be flushed by their proximity to the creek. In Figure 3.6b the attenuation of the GPR signal is consistent with this interpretation. Overall, smaller, relatively resistive zones in the TEM section are associated with the less attenuated zones in the GPR data in Figure 3.6b and are similar in scale both laterally and vertically.

Interpretation of the GPR data where times have been converted to depths using the equation for phase velocity based on the full-solution of the wavenumber (Figure 3.6b) has greater similarity to interpretation of the inverted TEM section (Figure 3.6c) than interpretation based on processing using the low-loss equation (Figure 3.6a).

3.6 Conclusions

When working with GPR systems at low frequencies it may not always be clear when conditions allow low-loss assumptions to be used accurately. When these assumptions are no longer valid it is necessary to incorporate the full solution for the wavenumber equation when estimating phase velocity. This is not a trivial step, as this equation requires information about the conductivity structure of the ground, which may not be available.

Similarly, for EMI surveys, if the loss tangent is not sufficiently greater than 1, it may be necessary to use the full solution for the wavenumber equation to accurately estimate phase velocity and skin depth. This again is a complication as it requires knowledge about the permittivity of the survey area.

Implications for the further processing and inversion of both GPR and EMI data should be considered. Most EMI processing schemes and inversions ignore displacement currents. This has the potential to contribute to ambiguity in defining shallow conductivity structure. Similarly, conduction current information is shown to be important when processing low-frequency GPR data.

The equations reviewed in this paper are necessarily limited as they do not account for parameters used to calculate the wavenumber that may vary with frequency and are therefore complex. We only have a limited understanding of the nature of these variations, so our ability to solve for velocity and skin depth is limited by estimates of these parameters at one frequency. This is potentially a large source of error that requires further investigation.

Chapter 4

Combined processing and interpretation of ground penetrating radar and high-resolution time domain electromagnetics in a conductive setting

M. A. Hatch, T. Munday, G. Heinson, K. Lawrie, J. Clarke, P. Mill

Geology and Geophysics, School of Earth and Environmental Sciences
University of Adelaide, Adelaide, SA 5005 Australia

Text in manuscript

STATEMENT OF AUTHORSHIP

Combined processing and interpretation of ground penetrating radar and high-resolution time domain electromagnetics in a conductive setting

Text in manuscript

Hatch, M. A. (Candidate)
Developed concepts, wrote manuscript and acted as corresponding author.

I hereby certify that the statement of contribution is accurate

Signed .....*Date* 27 March 2011

Heinson, G.
Contributed to planning of article and provided critical evaluation

I hereby certify that the statement of contribution is accurate and I give permission for the inclusion of the paper in the thesis

Signed .....*Date* 28/3/2011

Munday T.
Contributed to planning of article and provided critical evaluation.

I hereby certify that the statement of contribution is accurate and I give permission for the inclusion of the paper in the thesis

Signed .....*Date* 27th March 2011

Lawrie, K.
Provided funding for project and initial motivation for work to be performed.

I hereby certify that the statement of contribution is accurate and I give permission for the inclusion of the paper in the thesis

Signed ..... *.....Date* 28/3/11

Clarke, J.
Assisted with TEM data collection and initial discussions on data interpretation.

I hereby certify that the statement of contribution is accurate and I give permission for the inclusion of the paper in the thesis

Signed ..... *.....Date* 28/3/11

Mill, P.
Collected GPR data for project and initial discussions on GPR data processing.

I hereby certify that the statement of contribution is accurate and I give permission for the inclusion of the paper in the thesis

Signed …… *……..Date…27 March 2011…*

4 COMBINED PROCESSING AND INTERPRETATION OF GROUND PENETRATING RADAR AND HIGH-RESOLUTION TIME DOMAIN ELECTROMAGNETICS IN A CONDUCTIVE SETTING

4.1 Summary

Ground geophysical techniques provide high-resolution data sets that have the potential to provide information about floodplain conditions, including surface water - groundwater interactions, distribution of saline groundwater, and location of fresh-water lenses. Along the floodplains of the Murray River in southeastern Australia, where the groundwater in the floodplains often equals or exceeds sea-water salinities, conditions are particularly difficult for the application of electrical and electromagnetic (EM) techniques. In this study, coincident traverses of low-frequency (25 MHz) ground penetrating radar (GPR) and high-resolution ground-based time domain EM (TEM) data were acquired on three transects over floodplains of the Murray River, west of Mildura, Victoria, Australia. The primary objective of this study was to integrate GPR and TEM data sets in the hydrogeological investigation of these environments and to ascertain whether benefit could be gained by their combined interpretation.

The TEM data were processed using smooth-model and discrete-layer 1D inversions. The GPR data were initially processed using standard time-to-depth equations, but the assumptions of low-loss and normal incidence produced inaccurate solutions. Using the phase velocity equation, based on the full solution of the wavenumber equation to allow for the high-loss component of the data, significantly improves the interpretation of data collected in these conductive settings. This requires inclusion of information about both the conductivity and dielectric permittivity structure of the area. The revised processing of the GPR data indicates that the calculated arrival time for signal from the surface layer, based on the TEM, is longer than the observed arrival of the surface ground-wave, and therefore the GPR-derived surface layer conductivities are less than the TEM-derived conductivities for the same layer. Although the processing shown in this paper does improve the utility of GPR data collected in high-loss environments, they are only incremental improvements, and GPR data still yield little extra information on the characteristics of floodplain sediments and their variability.

4.2 Introduction

Ground penetrating radar (GPR) systems have not been employed in conductive ground settings primarily due to high signal attenuation at normal operating frequencies. However, the recent development of lower frequency systems (10 MHz to 100 MHz) intended to image deeper (see, for example, Davis and Annan, 1989; Jol et al., 2002; Tallini et al., 2006; Tsoflias and Becker, 2008; Zeng et al., 2008; Franke and Utsi, 2009) has prompted renewed trials of their capability in more conductive environments. This includes the 25 MHz system used in this study. We anticipated that the main limiting factors when running these surveys would be: a) the attenuation of signal related to the presence of highly conductive groundwater just below the surface, thereby limiting penetration to only a few metres; and b) the difficulty of resolving thin layers in the near surface because of the relatively large wavelength (approximately 2 m at typical velocities) of the 25MHz GPR system. Two additional factors subsequently considered were whether breaching low-loss assumptions when estimating phase velocities would result in significant depth estimation errors, and whether the large transmitter – receiver separation would result in significant errors when calculating the depths of shallow features, particularly as normal incidence is generally assumed when processing GPR data.

The GPR data acquired for this study were initially processed using routines that employ the commonly used assumptions of low-loss and normal incidence. An alternative approach using the full-solution of the wavenumber as the basis for calculating phase velocity (Chapter 3 of this thesis and Giroux and Chouteau, 2010) was also examined. The conditions under which this solution should be used were considered. A method that incorporates the full set of conductivity information from collocated TEM data to estimate the phase velocity structure of the area was developed. Based on surface-layer information, an approach for estimating surface-layer conductivity and thickness using the GPR data set is described. Results from the full-solution processing are compared with those from the initial low-loss processing, and we further describe how the GPR data were corrected for system geometry.

The term “surface layer” is used frequently in this chapter. It is intended to denote the shallowest layer that the two geophysical techniques used for this study are able to resolve (sometimes with difficulty). It is generally starts at the surface and extends to a depth of two to five metres.

4.3 Study area

The ground GPR and TEM data presented here were acquired as part of a ground validation program for a large airborne electromagnetic (AEM) survey undertaken along the

Murray River, in southeastern Australia, specifically to examine the risk of salinisation to the river and the adjacent floodplains (Lawrie et al., 2008). As part of that study, three lines of ground-based TEM and GPR, varying in length from less than 3 km to more than 16 km, were collected to establish if these data sets could be interpreted together to improve understanding of floodplain dynamics and structure at finer scales. Their locations are shown in Figure 4.1, which also shows the outline of the Murray River and associated floodplains, between approximately Wentworth, New South Wales to the east, and Chowilla Creek, South Australia, to the west. The floodplain in this part of the Murray River is made up of a surface layer consisting of clays, silts and fine sands, generally 1 to 7 metres thick, overlying coarser sands. The water table typically occurs at a depth of 2 to 5 m and is usually very saline, with conductivities often greater than 5,000 mS/m (0.2 ohm-m) (Aquaterra, 2010). Locally, groundwater may be less saline, particularly in the immediate vicinity of the Murray River and along other smaller, watercourses associated with the river system, where flushed zones are developed (Murray Darling Basin Commission, 2003; Overton et al., 2006; Lawrie et al., 2008; Aquaterra, 2010). The background image for Figure 4.1 is an image of groundwater salinity in this area (Murray Darling Basin Commission, 2002) showing the high groundwater salinities that characterise this area.

All three traverses were along dirt tracks that started on the southern margin of the floodplain system lining the Murray River, ending immediately adjacent to the river itself (Figure 4.1). Each transect was designed to intersect zones of interest on the floodplain.

4.4 Geophysical data acquisition and processing

4.4.1 Time domain EM: NanoTEM

The towed TEM system used for this survey work was Zonge Engineering's NanoTEM system. This EM system was developed in the early 1990's as a fast-sampling geophysical tool for near-surface investigations.

Data acquired for this study were collected in February 2008. A 3 x 3-m plastic transmitter - receiver frame was pulled on a plastic sled approximately 8 m behind a quad bike, recording data at discrete time intervals (Figure 4.2a). The transmitting antenna was a triple-turn of wire attached to the frame, with the 1 x 1-m triple-turn receiving antenna mounted in the centre. Data were collected and recorded every two seconds, stacking 100 cycles at a repetition rate of 64 Hz. For a ground velocity of 5 to 10 km/hr, data were recorded at approximately 3- to 6-m intervals. Locational information coincident with EM data acquisition was collected using a GPS unit.

NOTE:
This figure is included on page 80 of the print copy of the thesis held in the University of Adelaide Library.

Figure 4.1. Location of the study area in southeastern Australia highlighted on the location map with a red polygon. The Murray River is the boundary between New South Wales and Victoria, as well as for the offset section of South Australia. The areal extent of the floodplains around the Murray is highlighted with green stippling. The underlying image is of regional groundwater salinity. The TDS of seawater is approximately 35,000mg/L (Murray Darling Basin Commission, 2002).

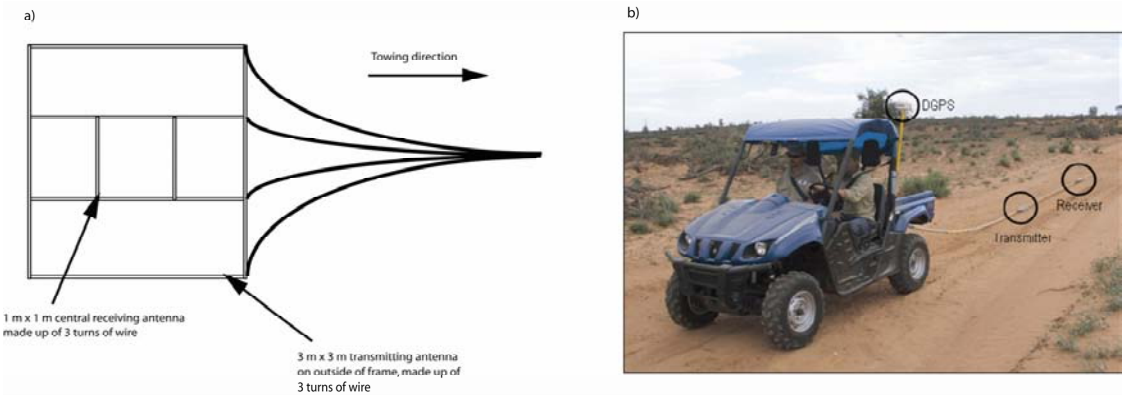

Figure 4.2. Equipment used for ground component of this study. a) schematic diagram of towed TEM system; b) photo of GPR rig on site.

Following acquisition, the two data sets (TEM decays and GPS locations) were combined, and inverted using two different 1D inversion routines: Zonge Engineering's smooth-model inversion, STEMINV and the University of Aarhus' EM1DINV, used here as a discrete-layer inversion.

STEMINV is a minimum structure inversion that calculates a maximum depth for a given sounding based on the raw data, then divides that depth into many thin layers with fixed thicknesses and assigns each layer an average conductivity, based on the sounding data. As the inversion process progresses, the conductivity of each layer is allowed to change, while the layer thickness remains fixed. This produces a conductivity-depth sounding for each data sounding, where conductivity varies smoothly with depth. This type of smooth inversion does not produce sharp, interpretable boundaries between geologic units. Nevertheless, as the number of layers is large and each layer thickness is small, this type of inversion may show more vertical variation, and therefore resolve smaller features that may be missed by a discrete-layer inversion (Siemon et al., 2009; Reid et al., 2010).

A discrete-layer type of 1D inversion uses a small number of layers to represent the subsurface (Auken et al., 2005). For this project, a modified discrete-layer inversion is used, where the number of layers is set at the start, with layer thickness and conductivity allowed to vary. Layer conductivity was slightly constrained to match adjacent layers within a sounding to improve model fit. This type of inversion has the ability to show contact locations more accurately than smooth-model inversions. For this work, three separate discrete-layer inversions were run for each complete data set, i.e. a one layer, a two layer and a three layer inversion. At each sounding location, the sensitivity analysis results from each inversion were compared and the result used that maximized the number of layers, but for which the sensitivity results were within set limits. These criteria were based on error and fit calculations performed by the inversion routine, as described in Auken et al. (2005).

Results for the smooth-model inversion and the discrete-layer inversion were then stitched together into separate sections, fitted to topography derived from high-resolution GPS data collected with the GPR, and presented as conductivity depth sections. Figure 4.3a is an example of the discrete-layer inversion and Figure 4.3b is an example of the smooth-model inversion results. The results are similar, with the smooth-model inversion showing more detail than the discrete-layer inversion, but not producing sharp boundaries at contacts.

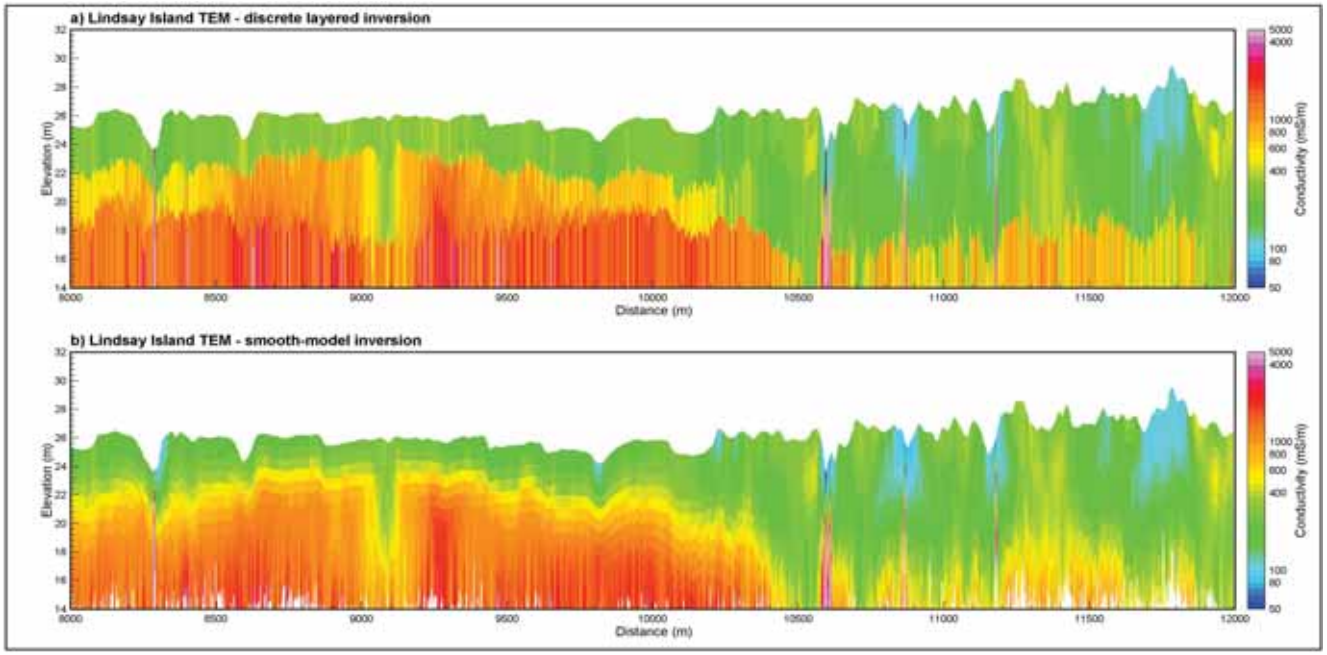

Figure 4.3. Comparison between conductivity depth sections for: a) discrete; and b) smooth-model inversion results from the TEM. The vertical axis is elevation in metres. The horizontal axis is distance along profile in metres.

The two inversions were used at different stages in this study during data processing and interpretation to take advantage of the strengths inherent in each. The smooth-model results were used in an analysis of finer details associated with floodplain variability, particularly in the top few metres, details that are not resolved in the discrete-layer inversion. The discrete-layer results were employed in some of the later processing steps because the large number of layers in the smooth-model inversion would have complicated the process.

The 1D model assumption used in the inversions is mostly valid in the sub-horizontal, layered sedimentary settings that are encountered in the study area.

4.4.2 Ground penetrating radar: GPR

The GPR data acquired for this survey were collected in late January 2008 using the Mala ProEx GPR controller unit, and the Mala RTA 25 MHz unshielded antennae, towed behind a two-seater quad bike (Figure 4.2b). There was a 4-m spacing between the receiving and transmitting antennae on this system. Data were recorded at 0.5 second intervals, stacking 4 readings. Towed at 5 to 10 km/hr, data were recorded at approximately 0.7- to 1.4-m intervals. GPS data were collected simultaneously with the GPR data.

It should be noted that the transmitter and the receiver on the Mala RTA system are oriented in a collinear rather than the more conventional parallel setup, thereby making the system "towable" (Figure 4.2b). While this is convenient for efficient data collection in the field, due to the shape of the transmitted field data collected using this orientation are more affected by features that are offline, than when collected using the parallel setup (Annan, 2005a).

Initial data processing was undertaken using Sandmeier Software's REFLEXW processing package. The data were resampled to 2-m station increments, signal offset corrected (i.e. dewowed), bandpass filtered (with cut-offs at 5, 15, 55 and 75 MHz), and diffraction stack migrated (to minimize air-wave effects only as the antennae are not shielded). Two-way travel times were then converted to depths. After calculating depths, the data were fitted to topography, based again on the high-resolution GPS data, and the results presented as depth sections.

4.4.2.1 GPR data processing

The methodology described here is based on a phase velocity equation that is not limited to low-loss conditions (Giroux and Chouteau, 2010 and Chapter 3), and uses the geometric-optics approach, commonly called ray-tracing, to translate times to depths in each sounding. One of the underlying assumptions when applying ray-tracing is that the wavelength of the system is significantly less than the depth to the feature (Annan, 2005a); this is not the case here. Using a typical velocity for the study area of $5x10^7$ m/s, and the pulse width for a 25 MHz system

of 40 ns, the wavelength is 2 m. As will be shown in this study, it is unlikely that the GPR signal penetrates further than a total of 10 m in this conductive environment, and much of what is interpretable in these data sets occur in the top 4 m. Therefore, ray-tracing may not be the most appropriate method for determining depth to features. Nevertheless, as an approximate initial approach for GPR data collected under difficult conditions, these simplifications were deemed appropriate. While recognising that the method suggested here may not be ideal, we suggest that the results are reasonable for data collected under these conditions.

For the bulk of the GPR data analyses that follow, the relative dielectric permittivity of the study area is assumed to be 11. This is an estimate for a floodplain type of environment, where the surface layer is likely to be dry, with moisture increasing with depth. Reynolds (1997) lists relative dielectric permittivity values for a number of soil types, ranging from 3 to 30, with clay soil (dry) listed at 3, marsh at 12, agricultural land at 15 , pastoral land at 13 and "average" soil at 16. Other values of permittivity were also tested.

In Chapter 3 the importance of evaluating the loss tangent when processing data from low-frequency GPR surveys was noted. Most GPR data are collected under low-loss conditions where the loss tangent is much less than 1 (Davis and Annan, 1989). The equation for loss tangent is given by Equation 4.1:

$$\tan\theta = \frac{\sigma}{\varepsilon\omega} \qquad (4.1)$$

where σ is electrical conductivity (S/m), ε is dielectric permittivity (F/m). For convenience we note that ε is often expressed as $\varepsilon_0\varepsilon_r$, where ε_0 is the permittivity of free space (8.854 x 10^{-12} F/m) and ε_r is the (dimensionless) relative dielectric permittivity. For the remainder of this chapter we will refer to the relative dielectric permittivity (ε_r) as permittivity.

Equation 4.2 is the standard, low-loss equation used to estimate phase velocity. Phase velocity is used in GPR processing to translate two-way travel times to depths:

$$v = \frac{1}{\sqrt{\mu\varepsilon}} \qquad (4.2)$$

where μ is magnetic permeability (H/m) and is often expressed as $\mu_0\mu_r$, where μ_0 is the magnetic permeability of free space (4π x 10^{-7} H/m) and μ_r is relative magnetic permeability. As μ_r is very close to one for many near-surface materials (Lazaro-Mancilla and Gomez-Trevino, 2000), we assumed that to be the case for this study.

Equation 4.2 is a relatively simple expression for phase velocity that is only dependent on permittivity. Standard tables for the permittivity of different materials are given in Reynolds (1997), Scharma (1997), and Annan (2005a; 2005b) and these may be used in Equation 4.2. When low-loss assumptions are violated, the phase velocities estimated using Equation 4.2 are

inaccurate, producing sections where the depth to features is incorrectly determined. In Chapter 3 it was shown that the loss tangent needs to be less than 0.7 for displacement currents to dominate and for low-loss conditions to prevail. When the loss tangent is between approximately 0.7 and 10, conditions are in the transition band between low-loss and quasi-static conditions. Under these conditions, phase velocity estimates can be improved using Equation 4.3 (shown originally in Chapter 3), the full-solution phase velocity equation:

$$v = \frac{1}{\sqrt{\frac{\mu\varepsilon}{2}\sqrt{\left(1+\frac{\sigma^2}{\varepsilon^2\omega^2}\right)}+1}} \qquad (4.3)$$

where ω is angular frequency (given by $2\pi f$, where f is the system frequency). Equation 4.3 is dependent on permittivity and conductivity, making it necessary to have additional information about the conductivity structure of the ground over which the survey was run. It should be noted that the band limits given above were based on the comparison of phase velocities using Equations 4.2 and 4.3, noting where the differences between the two were greater than 5%.

To put this into the context of the field area where our data were collected, for a 25 MHz GPR system, assuming that the ground permittivity is 11, the errors in using the low-loss phase velocity equation are greater than 5% for ground that is more conductive than 11 mS/m (91 ohm-m). Results from the TEM survey run concurrently, as well as other work on floodplains along this part of the Murray River (Figure 4.1 and Aquaterra, 2010), show that large areas are affected by salinisation, and therefore are likely to be characterised by conductivities that are significantly higher than 11 mS/m. Therefore, Equation 4.3 should provide more reasonable phase velocity estimates than Equation 4.2 under these circumstances.

4.4.2.2 System geometry

Another critical step in processing the GPR data acquired for this survey is to correct for errors in depth estimation due to the relatively large offset between the GPR receiver and transmitter. Figure 4.4 illustrates this for a reflector at 0.5-m depth. For a system with a 4-m separation between the transmitting and receiving antenna, a signal from the surface to a reflector at 0.5 m depth travels a total distance of 4.12 m (the indicated dashed line), and not the normal incidence two-way travel distance of 1 m (the solid vertical line). If normal incidence is assumed, the reflector at 0.5-m depth will be interpreted to occur at a depth of 2.06 m, i.e. half of the two-way travel distance. The adjusted depth for signal in a one-layer earth is given using the following geometric correction based on standard seismic and GPR hyperbolic function depth equations (Blindow, 2009):

$$D = \sqrt{\left(\frac{t_{2way} * v}{2}\right)^2 - \left(\frac{H}{2}\right)^2} \quad (4.4)$$

where D is depth, t_{2way} is the two-way travel time, $\boldsymbol{v}$ is the phase velocity, and H is the horizontal separation between the receiver and the transmitting antennae.

Correcting for system geometry is more complicated for multilayer cases where the ray path is refracted at each velocity boundary in accordance with Snell's law (Figure 4.5). This is solved here by iteratively testing all possible ray paths (in 1 degree increments) from the transmitting antenna into the first layer, applying Snell's law successively at each interface until the ray path is found for which the calculated total time most closely matches the time record being examined. Once the ray path is found, the total vertical depth is determined through successive applications of Equation 4.4 to determine the thickness of each layer and summing the individual thicknesses.

In EM theory, it is recognised that for a wave travelling from a non-conductive material to a conductive material, the refraction angle is complex, making evaluation of Snell's law more difficult (Stratton, 1941). In this situation, the component of the EM wave associated with the signal phase refracts at one angle, and the component of the EM wave associated with the signal amplitude refracts at another. Given the shallow depths involved in this study, the complication in implementing this and the likelihood that errors will not be large for the relatively short distances involved, this is ignored here. Further work is needed to evaluate the effects of complex refraction on GPR data.

4.4.2.3 Combining conductivity and system geometry

Combining the steps outlined in the previous two sections in order to improve velocity estimation and to correct for system geometry, involved a number of iterations. Each GPR sounding is matched with its nearest TEM equivalent, with the conductivity from the latter then used as the basis for the velocity estimate for each GPR sounding. To simplify processing, it was practical to use a relatively simple conductivity model with a limited number of layers to solve for the correct ray path using Snell's law. Results from the three-layer, discrete-layer inversion of the TEM data were used to process the GPR data.

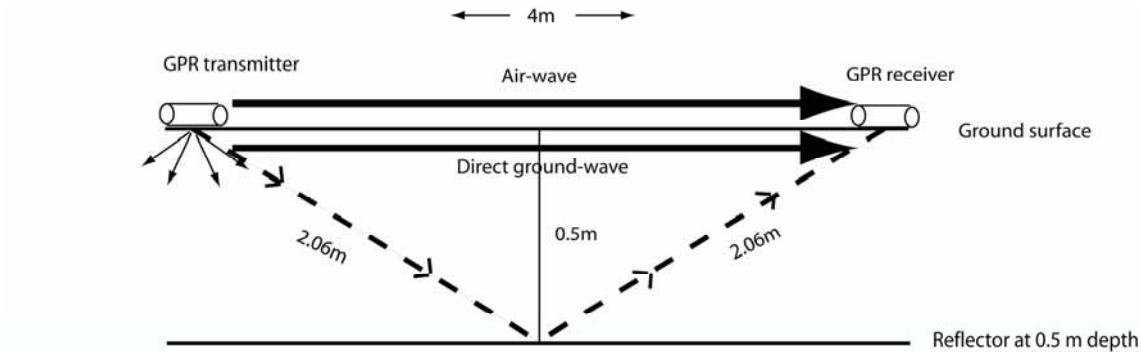

Figure 4.4. Schematic diagram of near-surface interactions for GPR system where the receiving and the transmitting antennae are separated by 4 m. For a reflector at 0.5 m depth, the signal actually travels 4.12 m from the surface to the reflector and back to the surface (dashed line). This arrives only 2.4 ns later than the direct wave, making resolution of shallow features difficult.

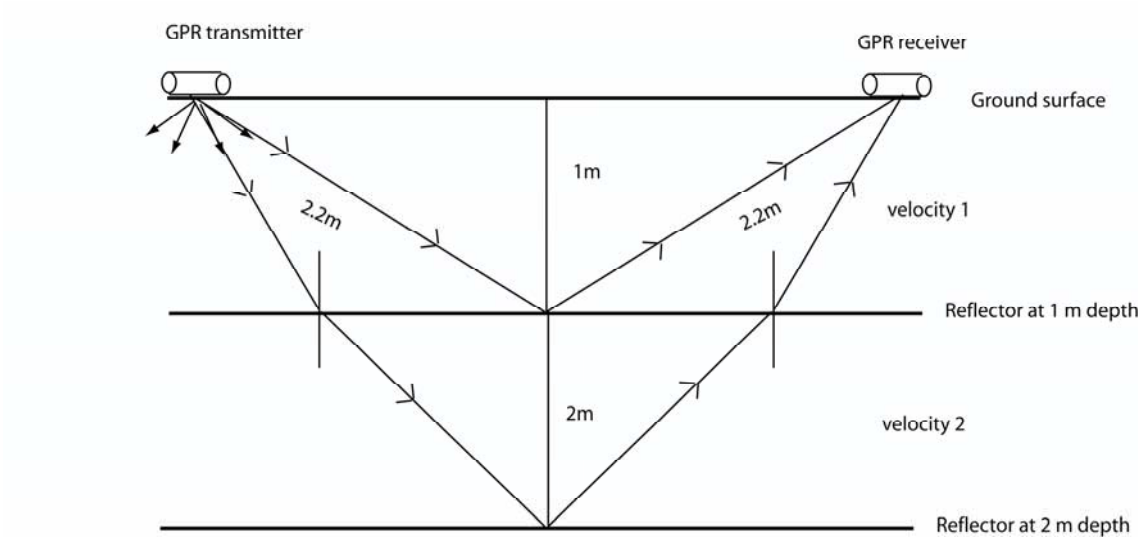

Figure 4.5. Geometric corrections for deeper layers are complicated by differences in layer velocity refracting the travel path. The ray paths need to be approximated using Snell's law.

4.4.2.4 Near-surface resolution

Resolution of shallow reflectors is relatively poor for a system with a large distance between the receiving and transmitting antenna (Figure 4.4). Using a typical phase velocity for this area of $5x10^7$ m/s the ground-wave travels the 4 m from the transmitter to the receiver in 80 nanoseconds. Signal from the reflector at 0.5-m depth travels 4.12 m, and arrives in 82.4 nanoseconds, only 3% different than the direct ground-wave, which is not a significant enough time difference to resolve the ground-wave from the reflected wave. For a reflector in the same material at a depth of 3 m, the signal arrives at 144 nanoseconds, which can be resolved.

4.5 Discussion

When the TEM data were used as the basis for calculating the phase velocity based on the full solution to the wavenumber, it was noted that the calculated, direct ground-wave travel time was longer than the observed arrival of the direct ground-waves for most soundings. There are three explanations for this that need to be evaluated: 1) there is an error in defining the time of the transmitter turn-on, resulting in inaccurate timing of reflections; 2) there is a thin resistive layer at the surface that is not resolved by the TEM, affecting the timing of the GPR; or 3) the two systems are resolving the same surface layer, but producing different estimates of the conductivity for that layer. The first explanation is relatively simple to evaluate, and will be analysed in this section. The other two are difficult to corroborate, as either may be correct at different locations along a particular transect. These will be examined further in the following sections.

The analysis of the GPR waveform and the resulting conductivity / thickness inferences in this and following sections would be improved if the transmitted waveform of the GPR system used to collect these data was known. As it is not known, a Ricker wavelet (Sheriff, 2002) was assumed and is the basis for the determination of the timing for the air wave, the ground wave, and the first true reflection arrivals. It is quite possible that these arrivals are not as clearly defined as is assumed here, and that the onset and completion of parts of the signal overlap, resulting in uncertainty as to the timing of these events. Nevertheless, as the results of this analysis of the GPR data are quite consistent with TEM data collected over the same area, as will be shown in subsequent sections of this chapter, we suggest that the method shown here is at least a reasonable starting point for processing data collected under these conditions.

To evaluate the conductivity of the surface layer based on GPR data it is necessary to solve Equation 4.3 for conductivity and use the velocity of the ground-wave to estimate the conductivity at the surface:

$$\sigma = \varepsilon\omega\sqrt{\left(\left(\frac{2}{v^2\mu\varepsilon}\right) - 1\right)^2 - 1} \qquad (4.5)$$

Figure 4.6 shows an example of this, as applied to a single GPR sounding, in this case station 10000 on the Lindsay Island line. Figure 4.4 shows the GPR system configuration, specifically showing the air-wave and direct ground-wave. For a 4-m antenna separation, the air-wave, travelling at $3x10^8$ m/s, takes 13.3 ns to traverse the distance between the transmitting and receiving antennae. The 25 MHz GPR wavelet used by this system has a pulse width of $1/f$, or 40 ns and is assumed to be shaped similarly to a Ricker wavelet (Sheriff, 2002). Based on this pulse width, the air-wave is measured over a 40 ns time window (and finishes at t = 53.3 ns). In Figure 4.6 the time between transmitter turn-on and the arrival of the air wave (13.3 ns) is indicated with stippling, while the air-wave itself is indicated with cross-hatching. From the TEM, the conductivity of the top layer at this location is 314 mS/m (3.2 ohm-m). Using Equation 4.3 (assuming that the permittivity is 11), the velocity for this shallow layer is $2.75x10^7$ m/s. At this velocity the direct ground-wave travels the 4-m space between the receiving antenna and the transmitting antenna in 145 ns, indicated with the top arrow in Figure 4.6. From examination of Figure 4.6 the direct ground-wave arrival occurs at approximately 70 ns (indicated with the left arrow). Using the velocity calculated for this layer (4m/70 ns) of $5.7x10^7$ m/s, in Equation 4.5, yields a GPR–derived conductivity of the surface layer of approximately 60 mS/m (17 ohm-m).

To set the thickness for this layer, the time associated with the first arrival after the complete ground-wave (again, assuming that the wave is similar to Ricker wavelet shaped) is assumed to be the start of the first resolvable reflection after the ground wave, and is indicated with the bottom right arrow in Figure 4.6. As noted in the System Resolution section, the resolution of features in the top few metres is relatively poor, particularly given this system's larger transmitter – receiver separation. Using the phase velocity derived from the direct ground-wave arrival ($5.7x10^7$ m/s), and the time to the first reflection (approximately 140 ns), the surface layer thickness, in this example, is approximately 3.5 m, after correcting for geometry and two-way travel time.

Velocities and thicknesses based on the direct ground-wave arrival time from each GPR sounding are used in the GPR processing as the properties of the top layer. Once the calculated depth of the GPR signal exceeds this layer thickness, the velocity analysis reverts to the values calculated from the appropriate layer determined from the TEM inversion.

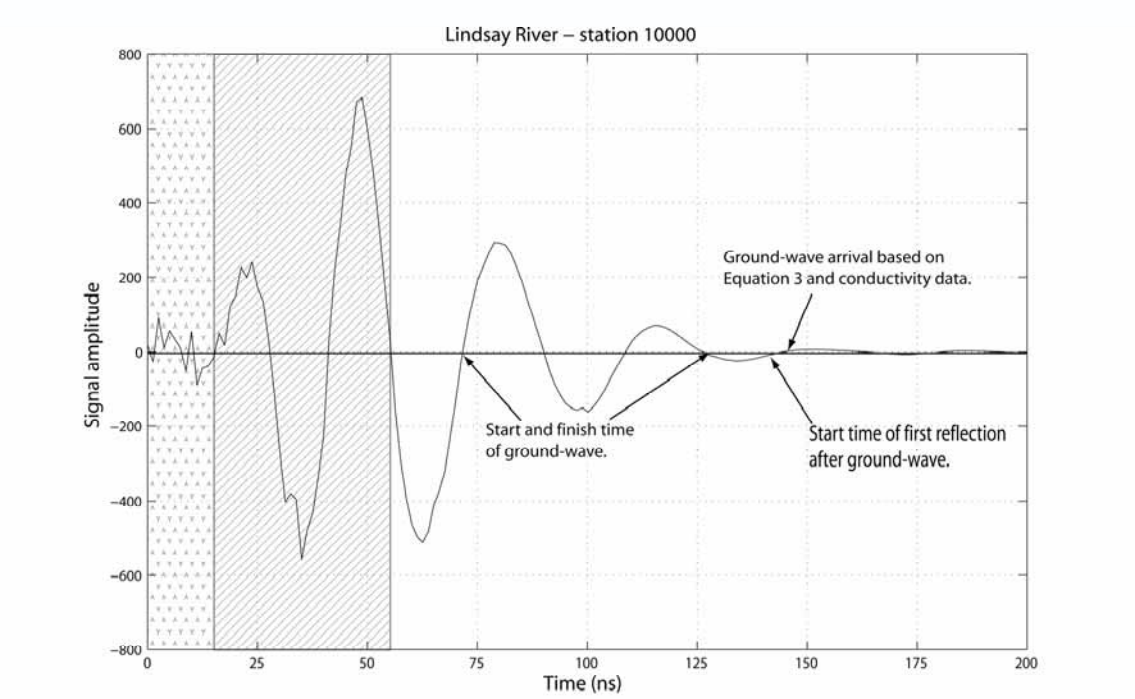

Figure 4.6. Calculating surface layer conductivity from GPR. The time from transmitter turn-on to the arrival of the air-wave is indicated with dotted stippling. The air-wave is indicated with cross-hatching. The conductivity of the top layer from the TEM is 314 mS/m (3.2 ohm-m). The calculated velocity is 2.75×10^7 m/s (based on Equation 4.3) so the ground-wave arrival should occur at 145 ns. Setting the conductivity to approximately 60 mS/m (17 ohm-m) for this layer sets the start time for the ground-wave correctly.

It is unlikely that the surface layer discrepancy described here is caused by a simple timing error in the GPR. Examination of Figure 4.6 shows that this would require a timing error of 70 ns (the difference between the calculated time for the direct ground-wave arrival of 140 ns and the observed time of 70 ns). It is possible that that there are less significant timing issues in these data, but it is unlikely that timing error alone explains the discrepancy.

Determination of the surface layer conductivity from the GPR data, described here, would be impossible if the ground conditions were closer to low-loss. The use of Equation 4.5 to calculate the conductivity of the surface layer from the direct-wave arrival time is dependent on the ability of the system to resolve the difference between the end of the air-wave and the arrival of the direct ground-wave. For a 25 MHz GPR system, with a 4-m separation between transmitter and receiver, and ground permittivity of 11, the trailing edge of the air wave is observed to occur at t = 53.3 ns (Figure 4.6). When the surface layer conductivity is 24.7 mS/m (40.5 ohm-m) the leading edge of the ground wave also arrives at 53.3 ns. When the ground is more resistive than this value the air wave and the ground wave overlap making it progressively more difficult to separate the two and, therefore, estimate the ground-wave velocity.

4.5.1 Comparison of low-loss processing with full-solution processing

Figure 4.7 shows the GPR results from a 2-km subsection of the Lindsay Island section, where standard, low-loss processing is compared with full-solution processing. The processing steps for the two GPR sections are identical except for the conversion of time to depth. Figure 4.7a shows the results when low-loss processing is used, i.e. Equation 4.2. When the permittivity is set to 11, the phase velocity is uniformly $9x10^7$ m/s. This value is employed to convert all GPR times to depths, correcting for system geometry using Equation 4.4. Figure 4.7b shows the results when the GPR times are converted to depths using full-solution processing, and Figure 4.7c shows the inverted TEM results for the same transect. The highly conductive features in the TEM section and the small breaks in the GPR data at approximately stations 10600, 10840 and 11190, are related to small bridges and culverts along the transect.

The most notable difference between Figures 4.7a and 4.7b is the vertical scale. The GPR data, as processed using the low-loss estimate of velocity shown in Figure 4.7a, span a total thickness of over 25 m, which does not vary. When processed using the full-solution phase velocity, as shown in Figure 4.7b, the depth extent of the section is more variable, with the total thicknesses varying from approximately 7 to 12 m, depending on local conductivity.

Along this transect, the two GPR sections would be interpreted similarly, particularly when based on signal attenuation. It is possible to identify zones that are highly attenuated in both, where groundwater is saline, as well as zones that are less attenuated, where groundwater is relatively fresh. Comparison of the vertical scale of the two plots shows that the section in Figure 4.7b bears a stronger resemblance to the TEM section than the section in Figure 4.7a, and would be interpreted similarly. Based on the TEM (Figure 4.7c), from station 9500 to 10400 the relatively resistive surface layer is interpreted to be dry soil, above the capillary fringe (Cresswell and Shand, 2009). This is underlain by a deeper saline groundwater system. The thickness of the surface layer is very similar to that defined by the relatively high amplitude signal at the top of the processed GPR data, shown in Figure 4.7b. However, significant differences are noted between it and the thickness of the same layer shown in Figure 4.7a. The signal magnitude in the GPR of the surface layer is high, suggesting that this layer is likely to be dry. From station 10400 to the north, this traverse runs parallel to Mullaroo Creek, a small, relatively fresh anabranch of the Murray River. The sediments along this stretch are more resistive than those seen on the southern end of this stretch, and are interpreted to be flushed by their proximity to the creek. In Figure 4.7b, attenuation of the GPR signal is consistent with this interpretation. Overall, smaller, relatively resistive zones in the TEM section are associated with the less attenuated zones in the GPR data in Figure 4.7a and are similar in scale, both laterally and vertically.

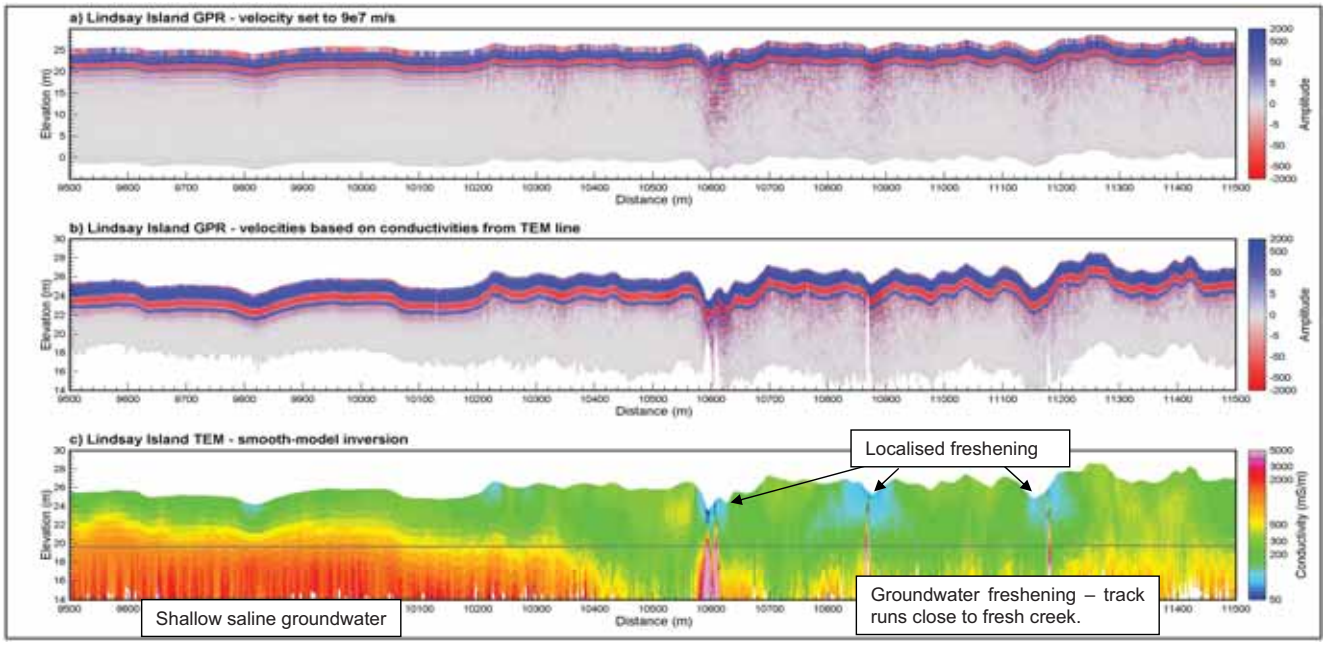

Figure 4.7. a) GPR data processed using low-loss assumptions and permittivity = 11; b) GPR data processed using velocities calculated based on the conductivity information from the TEM data set; c) inverted TEM data set. The vertical axis is elevation in metres. The horizontal axis is distance along profile in metres. Highly conductive features in the TEM section and breaks in the GPR data at approximately stations 10600, 10840 and 11190 are bridges (i.e. cultural features). Basic hydrogeological interpretation is highlighted on the TEM section. The location of the regionally determined water table is indicated with a grey line on the TEM section.

In evaluating the difference between these two sets of results it is worth considering whether the wrong permittivity value was used in the low-loss phase velocity equation. To evaluate this, the GPR sounding at station 10000 is examined. For this station, on Figure 4.7, the total depth for the GPR sounding, using the full-solution processing is 7.46 m, while the time for this reading is approximately 610 ns. From Equation 4.4, the average signal velocity required for this depth is approximately 2.52×10^7 m/s. Inverting the low-loss phase velocity equation (Equation 4.2) to solve for permittivity shows that the permittivity would need to be 142 to match this velocity and depth, which is unrealistically high for this type of environment (Reynolds, 1997; Scharma, 1997; Annan, 2005a).

Overall, interpretation of the GPR data where times have been converted to depths using the equation for phase velocity based on the full-solution of the wavenumber equation (Figure 4.7b) correlates better with the information shown in the TEM section (Figure 4.7c) than when these data are processed using low-loss assumptions (Figure 4.7a).

4.5.2 Analysis of the conductivity properties of the GPR-determined surface layer

Earlier in this paper we described a method for determining the conductivity and thickness of the surface layer, based on the GPR data alone. Figure 4.8 shows the results of these calculations, with the results superimposed onto the inverted TEM section. Results from km 8 to 12 of the Lindsay Island transect line are shown here. The GPR data for this transect are presented in Figure 4.8a, with the location of the first reflector highlighted in black. In Figure 4.8b the surface layer defined by the GPR has been overlain on the inverted TEM section. Figure 4.8c shows the TEM results based on the discrete-layer inversion, while Figure 4.8d shows the results when the smooth-model inversion is used. Note in Figure 4.8a that the black line is the same depth as the GPR-derived surface conductivity layer shown in Figure 4.8b, i.e. the depth to the first reflector in the GPR.

Comparison of the thicknesses defined for the surface layer by the GPR and the TEM (Figures 4.8b and 4.8c) shows a relatively good correlation from station 8000 to 10000. Over this part of the traverse the TEM shows that the surface layer is significantly less conductive than the second layer, and as a result this contrast is readily observable in that data set. From station 10000 to 12000 the conductivity contrast between the surface and the second layer is not as consistent. Nevertheless the surface layer delineated by the GPR is more resistive and consistent than the surface layer delineated by the TEM. Examination of the smooth-model TEM

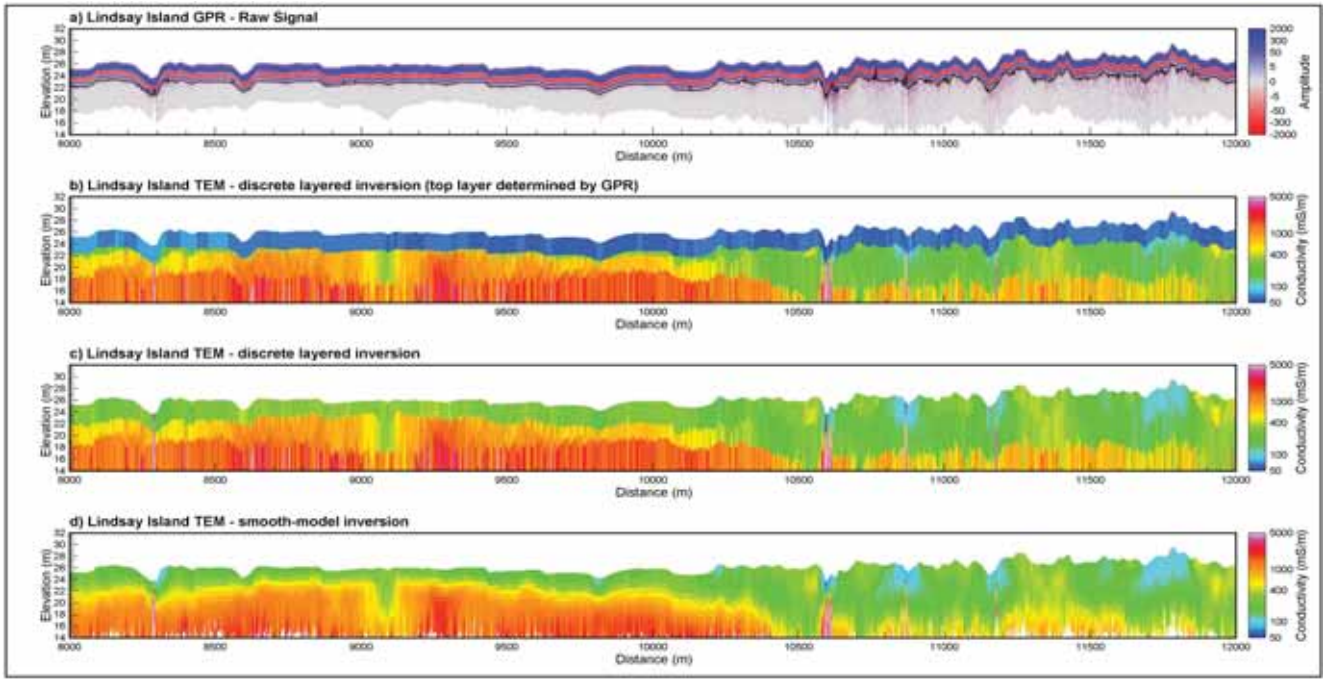

Figure 4.8. Depth sections of towed-TEM and GPR for the Lindsay River data set from km 8 to 12. a) GPR data with top of 1st major reflector highlighted in black; b) TEM data inverted using the discrete-layer inversion, with the top layer information derived from the GPR data; c) TEM data inverted using the discrete-layer inversion; d) TEM data inverted using the smooth-model inversion. The vertical axis is elevation in metres. The horizontal axis is distance along profile in metres. Permittivity is set to 11.

inversion (Figure 4.8d) suggests that there are locations along the transect where the smooth-model inversion resolves small, non-continuous resistive zones in the surface layer that are not resolved in the discrete-layer inversion, suggesting that the TEM may be having difficulty imaging the contrast between the two layers.

Comparison of the surface layer conductivities as determined by the TEM and the GPR show that the GPR-derived conductivities are, on average, nearly three times lower than the TEM-derived conductivities for that layer. The mean conductivity of the top layer of the entire Lindsay Island TEM discrete-layer inversion is 211 mS/m (4.7 ohm-m). The mean conductivity of the top layer, as defined by the GPR, is 71 mS/m (14 ohm-m). Using a different value for the permittivity in Equation 4.3 to determine the phase velocity does not reduce these differences significantly. When permittivity is set to 1, an unrealistically low value for this environment (Reynolds, 1997), the GPR-derived conductivity for the surface layer remains low at 111 mS/m (9 ohm-m). Similarly, it was shown earlier that it is unlikely that there is a significant timing error in the GPR resulting in the wrong velocity being calculated and therefore the wrong conductivity assigned. To continue analysing this discrepancy, the response of the TEM system was forward modelled, focusing on the top-layer response. The data were modelled using the University of Aarhus program Emma (which uses the engine from the EM1DINV code to forward model), and then inverted using the STEMINV smooth-model inversion program. Using both programs showed that the results of this testing were consistent across two modelling engines. For forward modelling purposes the TEM results from the zone from station 8700 to 9000 have been simplified to two layers. The thickness of the surface layer was fixed at 3 m, while the second layer extends to infinite depth. The conductivity of the second layer was set to 1000 mS/m (1 ohm-m). The response of the system was evaluated by varying the conductivity of the surface layer, using values of 333 mS/m (3 ohm-m), 167 mS/m (6 ohm-m), 111 mS/m (9 ohm-m), 83 mS/m (12 ohm-m) and 67 mS/m (15 ohm-m), thereby covering the range of conductivities between the TEM-based extreme and the GPR-based extreme. The complete results are shown in Figure 4.9.

Examination of Figure 4.9 suggests that the surface TEM response tends to group together for conductivities less than 167 mS/m, with only the surface response for the 333 mS/m layer standing out. The surface conductivities are similar to their real values for the 167 mS/m and 111 mS/m test values, with the inversion providing values of 142 and 120 mS/m respectively.

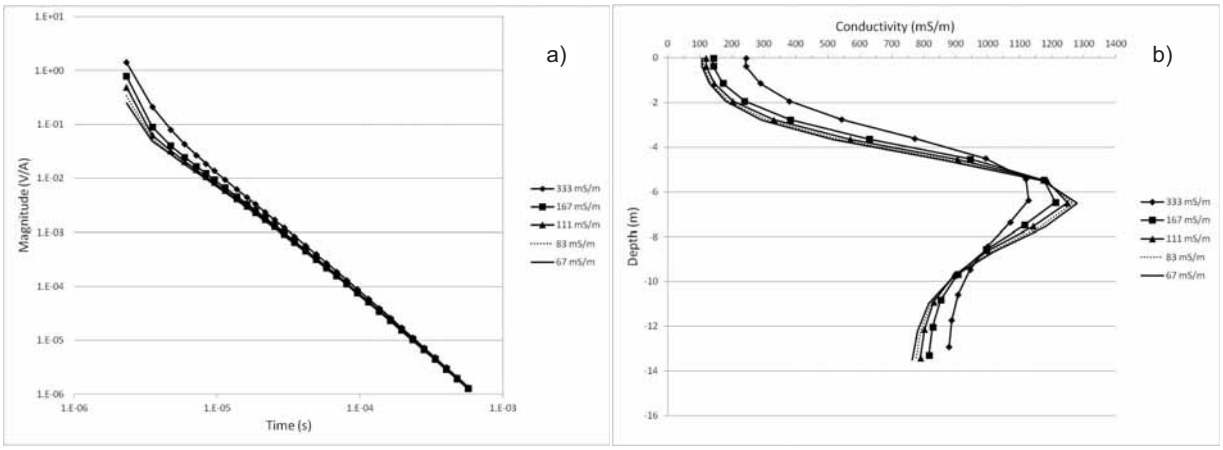

Figure 4.9. Forward modelled (a) and inverted (b) TEM response for five scenarios. All models were run for a two-layer model, with the surface layer extending to a depth of 3 m and the bottom layer set to 1000 mS/m (1 ohm-m). Surface layer conductivities were set to 333 mS/m (3 ohm-m), 167 mS/m (6 ohm-m), 111 mS/m (9 ohm-m), 83 mS/m (12 ohm-m) and 67 mS/m (15 ohm-m).

Above and below these values the inversion tends to further underestimate and overestimate conductivity. These results show that while there is ambiguity in the TEM system's ability to resolve the conductivity of the surface layer, this ambiguity is not sufficient to explain the conductivity discrepancies between the two systems.

Figure 4.10 shows the borehole conductivity results for Bore B7928, located at approximately station 3715 on the Lindsay Island line. The conductivity of the surface layer derived from the TEM matches the borehole conductivity better than the top layer conductivity derived from the GPR at that station. However, the ground TEM and borehole conductivity results diverge significantly at depths greater than 8 m. This suggests that the depth of investigation for the TEM system is similar to 8 m. The first data point for the inductive tool is at approximately 0.4 m. These results suggest that either: a) the TEM is better at resolving the conductivity of the surface layer than the GPR, or that b) the GPR surface response is based in the top 0.4 m.

4.5.3 Varying permittivity

In Equation 4.3 both conductivity and permittivity are variables that affect velocity. Similarly, in Equation 4.5, velocity and permittivity are both variables that affect conductivity. All of the results discussed so far have assumed that ground permittivity is 11, with velocity determined by the conductivity variation in the coincident TEM data sets. In this section we examine the results when the permittivity is set to 3 and 20, values chosen as reasonable permittivity limits for clay/silt soils with variable moisture content (Reynolds, 1997; Scharma, 1997; Annan, 2005a).

Figure 4.11 is the Lindsay River GPR section from km 8 to 12, with Figure 4.11a showing the results when permittivity is set to 3 and Figure 4.11b showing the results when permittivity is set to 20. Comparison of these sections shows that depth does not vary greatly when permittivity is varied. The maximum depth for the entire Lindsay River transect (approximately 17 km long) when permittivity is 3 is 15.8 m with a mean maximum depth of 8.4 m. When permittivity is 20 the maximum depth is 14.3 m with a mean maximum depth of 8.2 m. The GPR time for these deepest values is approximately 615 ns.

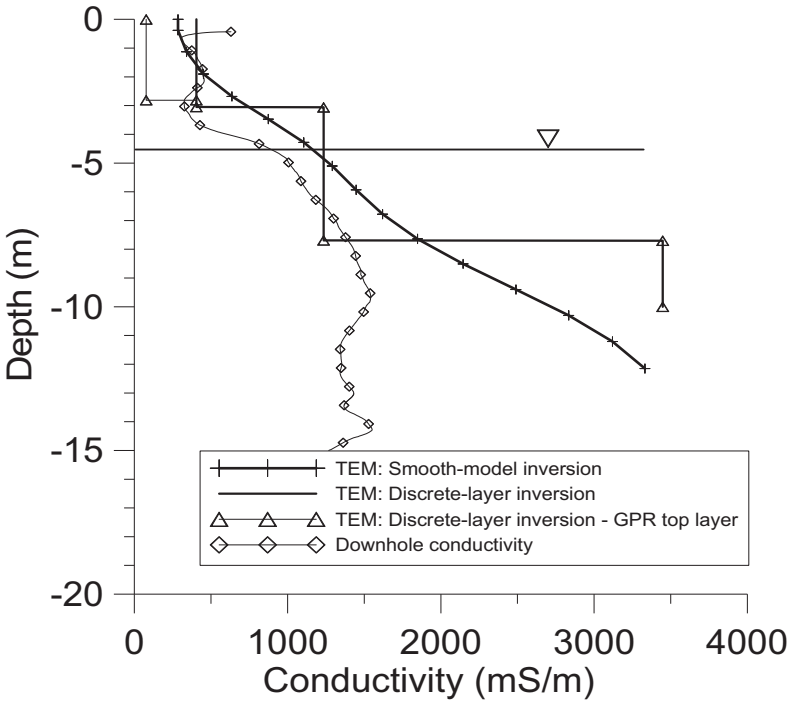

Figure 4.10. Borehole conductivity log for Bore B7928, located at approximately station 3640 on the Lindsay River line, compared with TEM smooth-model and discrete-layer inversion results at that station. GPR-derived surface layer conductivity is shown also for comparison. Approximate depth to water table indicated with black triangle.

These results are compared in Figure 4.12. Figure 4.12a compares calculated phase velocities at 25 MHz, varying both conductivity and permittivity in Equation 4.5. Figure 4.12b shows how loss tangent changes under the same conditions. Low-loss conditions, i.e. where the loss tangent is less than 0.2 (as defined in Chapter 3), are highlighted in grey on Figure 4.12b. Generally, when ground conductivity and loss tangent are high, permittivity has very little effect on phase velocity, and conductivity is the more important influence. As ground conductivity and loss tangent decrease, the influence of conductivity decreases and the influence of permittivity increases. These observations are consistent with the relatively insignificant variation in depths with permittivity variation shown in Figure 4.11. Ground conditions in the field area where these data were collected are generally conductive, so varying permittivity has little effect on phase velocity and, therefore, little effect on the maximum depth of the GPR survey.

The Lindsay River inverted TEM section from km 8 to 12 is shown in Figure 4.13. Sections in Figure 4.13a and 4.13b show the conductivity of the top layer based on the GPR, with the permittivity set to 3 in Figure 4.13a, and to 20 in Figure 4.13b. Figure 4.13c is the inverted TEM data without incorporating the surface conductivity information from the GPR. When the

permittivity is 3, the mean conductivity of the GPR defined surface layer is 83 mS/m (12 ohm-m). When the permittivity is 20, the mean conductivity of the surface layer is 53 mS/m (19 ohm-m).

These results are analysed in Figure 4.14, which compares calculated conductivities using Equation 4.5, where the velocity is fixed at 5.34×10^7 m/s, varying permittivity from 1 to 30. This phase velocity was calculated using Equation 4.3 (the full-solution phase velocity), setting the permittivity to 11 and the conductivity to 71 mS/m (the mean GPR-derived surface layer. conductivity for the Lindsay Island traverse). The range of calculated conductivities shown in Figure 4.14, when varying permittivity, is consistent with the conductivity variation shown in Figure 4.13.

Examination of Figures 4.11 to 4.14 permits us to conclude that when evaluating GPR data collected over conductive ground, under conditions that are not low-loss: a) variations in the conductivity of the subsurface affect the phase velocity more than variation in the permittivity does; and b) conductivity values calculated from the phase velocity of the direct ground-wave arrival is relatively sensitive to permittivity.

4.5.4 Using simpler estimates of conductivity distribution

In Figure 4.15 we compare the effects on the Lindsay Island GPR section, when the GPR data have been processed using different methods to estimate the conductivity structure of the survey area. In each case the ground-wave velocity and thickness based on the GPR has been used to define the surface layer, reverting to TEM conductivities to calculate depth for the remainder of the GPR data.

Figure 4.15a shows the GPR data processed using the full-solution phase velocity, and is the same as Figure 4.8a. Figure 4.15b shows the GPR data processed when the TEM data were processed to simulate the data collected by a low induction number (LIN) approximation based terrain conductivity meter (McNeill, 1980). These systems are significantly faster and easier to use than TEM systems but typically record a conductivity at a single receiver-transmitter separation and frequency, (i.e. at a single depth, or at most a small range of depths). For Figure 4.15b the conductivities of the top 5 m of the TEM smooth-model inversion data set were averaged for each station and these results used in Equation 4.3 to estimate the velocity for each GPR sounding using Equation 4.5. These averaged data are similar to the results from a LIN system, where the data have been LIN corrected (Reid and Howlett, 2001), to improve the estimate of conductivity in highly conductive ground. Figure 4.15c shows the data as processed when a single conductivity estimate for the survey area is used in Equation 4.3 to estimate phase velocity. In this case conductivity is set to 200 mS/m (5 ohm-m).

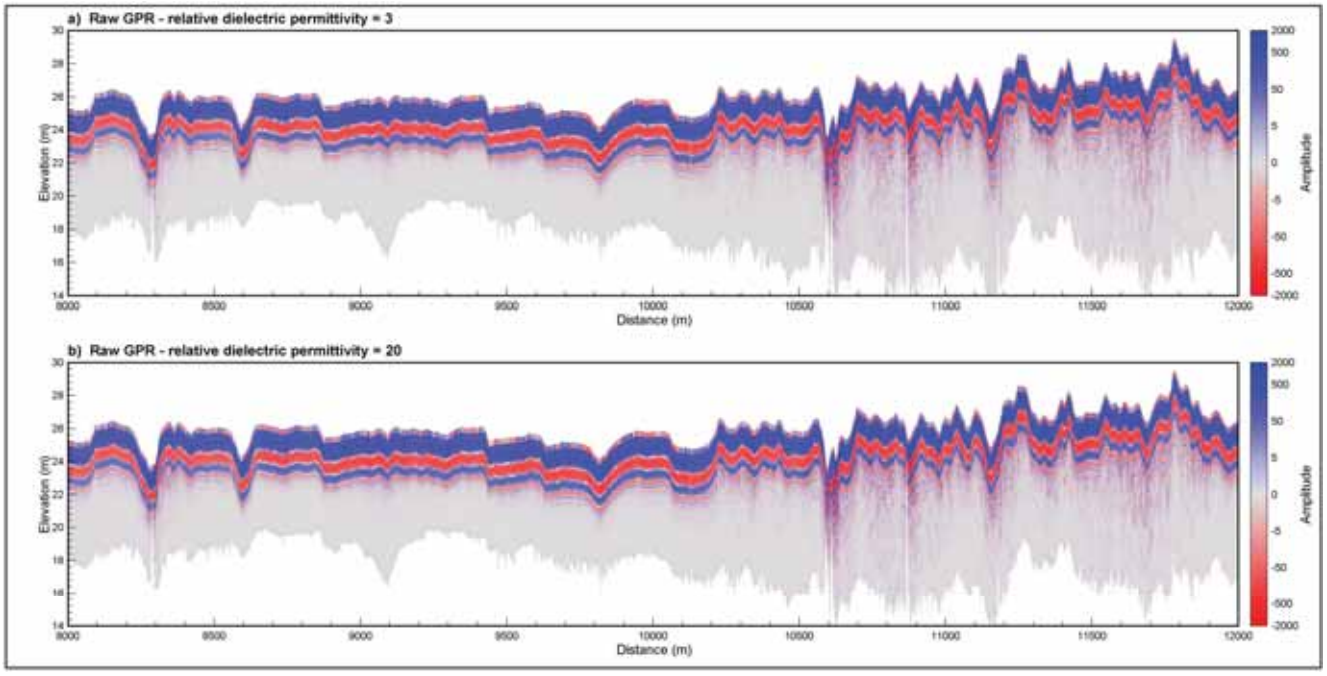

Figure 4.11. Comparison of GPR results when permittivity is varied for Lindsay River data set, km 8 to 12: a) permittivity is set to 3; and b) permittivity is set to 20. The vertical axis is elevation in metres. The horizontal axis is distance along profile in metres.

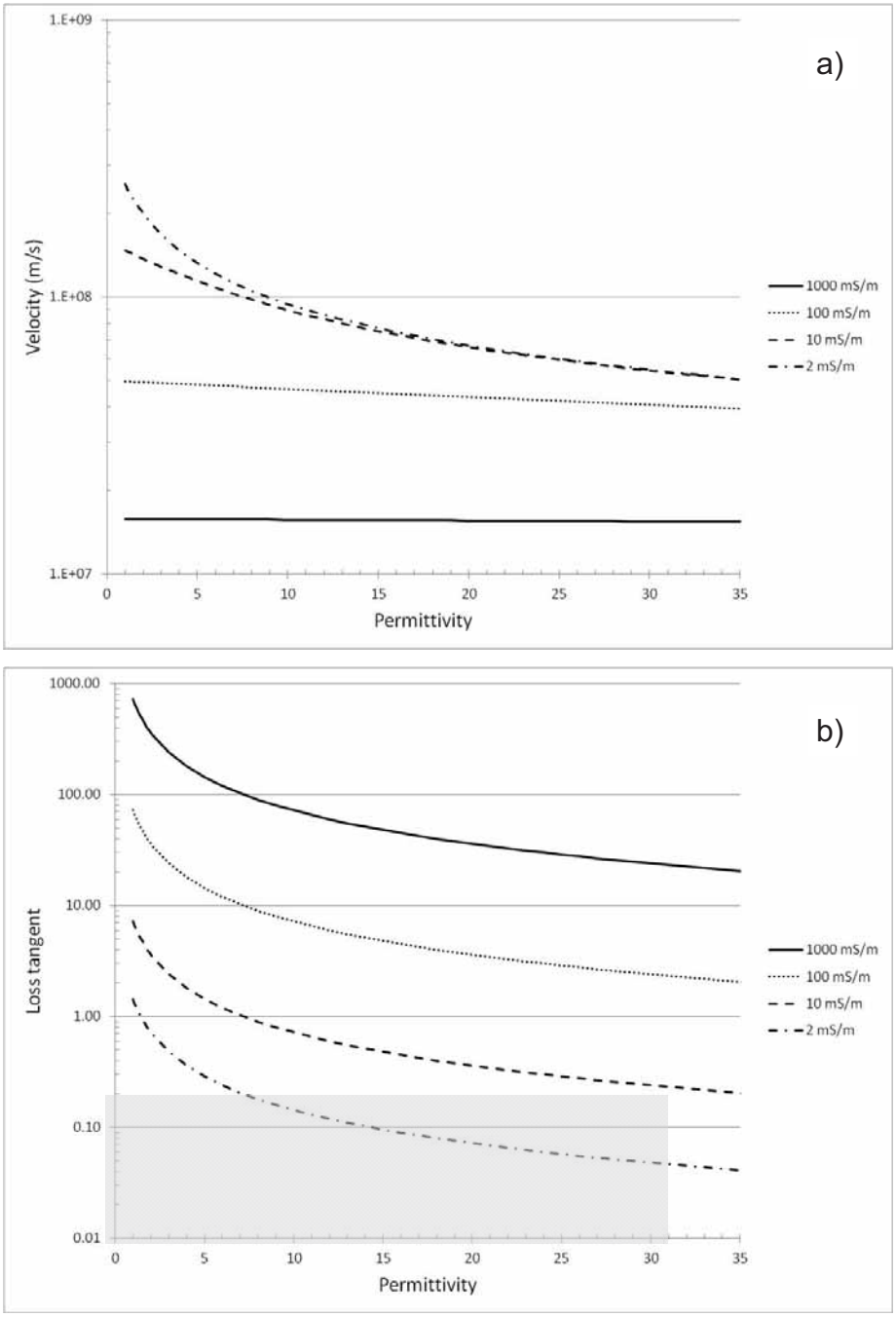

Figure 4.12. a) Phase velocity and b) loss tangent calculated for four conductivities, varying permittivity from 1 to 35. Low-loss conditions are highlighted in grey.

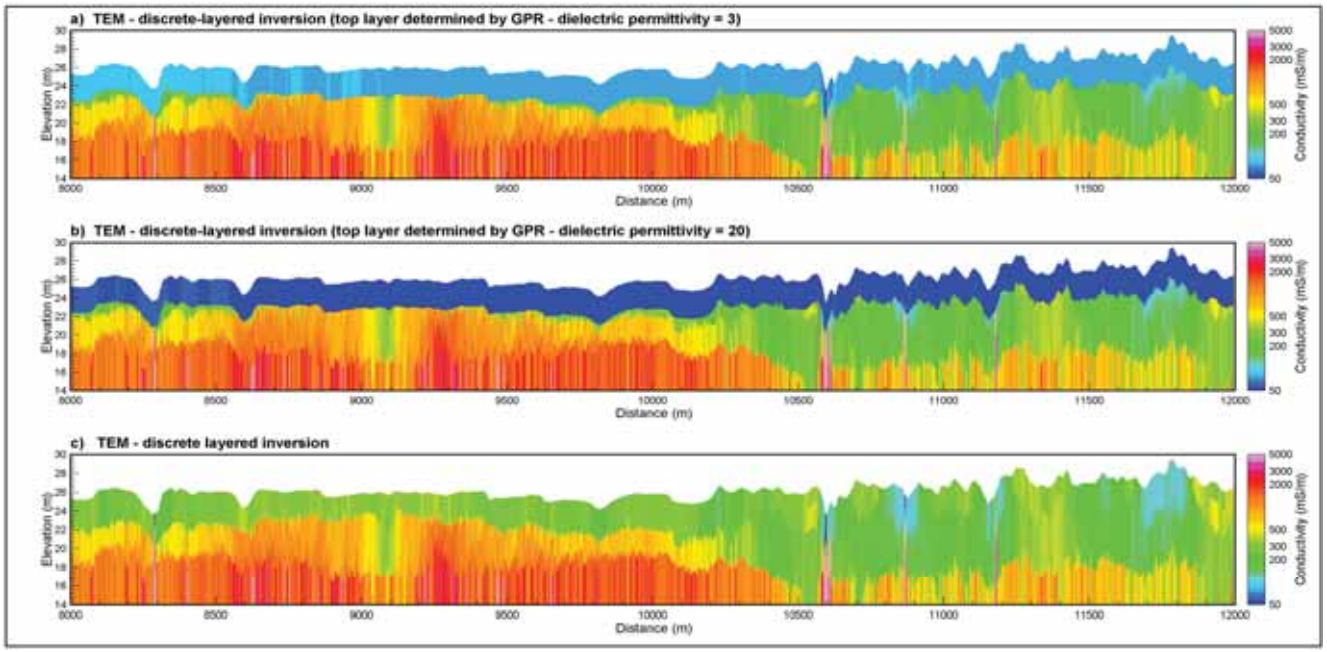

Figure 4.13. Comparison of TEM results when permittivity is varied for Lindsay River data set, km 8 to 12: a) inverted TEM data where the conductivity of the top layer is GPR-derived and the permittivity is set to 3; b) inverted TEM data where the conductivity of the top layer is GPR-derived and the permittivity is set to 20; and c) inverted TEM data without surface layer GPR. In all cases, the vertical axis is elevation in metres. The horizontal axis is distance along profile in metres.

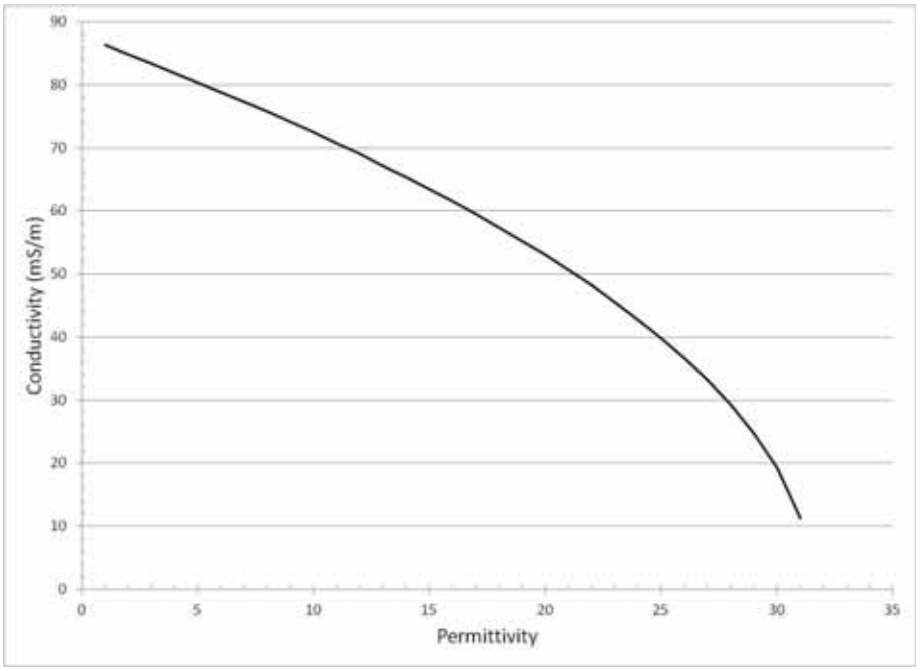

Figure 4.14. Conductivity variation plotted against permittivity. Phase velocity is fixed at 5.34×10^7 m/s.

When features in the "groundwater freshening" zone from approximately 10500 to 11200 on Figures 4.7 and 4.15 are compared, it is apparent that the location along line of the three smaller, near-surface zones labelled "localised freshening" would be identified in all of the GPR data sections, no matter how they were processed. The thickness and size of these zones, as interpreted from the low-loss velocity processing in Figure 4.7a, is significantly different to what would be interpreted from the TEM in Figure 4.7c. The fully-processed GPR shown In Figure 4.15a most closely resembles the TEM section in that zone, with the overall thickness of the section deepening, reflecting that the entire area is freshening. Also, the size and location of the smaller localised surface zones are similar, both in lateral and vertical extent, to the same zones in the TEM section. As the LIN processed GPR reflects the conductivity conditions in the top 5 metres, it does a good job of matching the TEM results for the smaller, shallow, localised freshening zones, but the results for the deeper parts of the section are not as good as for the fully-processed GPR. Similarly, using a single estimate for the conductivity of the entire area, Figure 4.15c, generally improves the quality of the interpretation, especially when compared to the low-loss processing. Nevertheless, this processing method does not allow the thickness of the section to vary, and therefore provides less information about the deeper part of the section, and whether it is freshening or not.

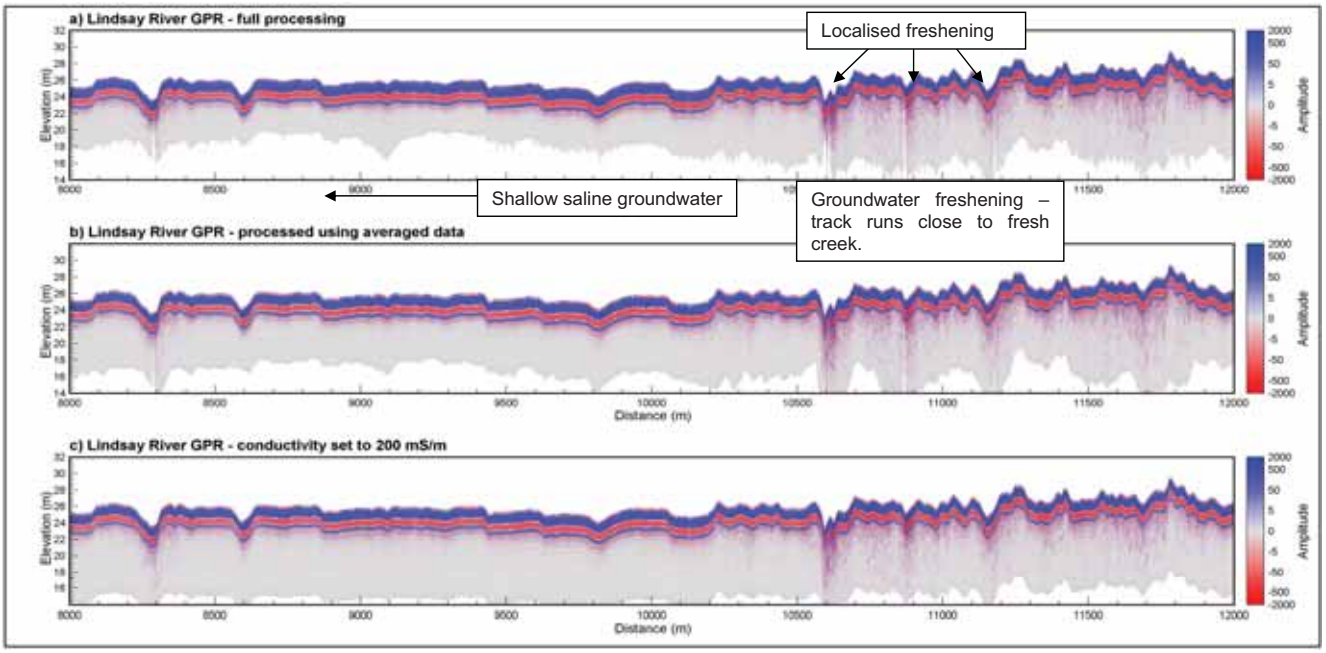

Figure 4.15. GPR depth sections for the Lindsay River data set from km 8 to 12 where the data were processed using three different methods to estimate conductivity conditions: a) GPR data processed using the full set of TEM data (same as Figure 4.8a); b) GPR data processed using averaged TEM data to simulate LIN-based terrain conductivity meter data; and c) GPR data processed using a single estimate (200 mS/m) for conductivity. In all cases permittivity was set to 11. Basic hydrogeological interpretation is highlighted on Figure 4.15a.

This type of comparison shows that transition-band GPR data, i.e. GPR data collected when the loss tangent is between 0.7 and 10, are best processed using all of the TEM information, with the simulated LIN system results being only slightly worse. The processing results based on the single estimate for conductivity are not as good as either of the others but are significantly better than the results derived using the low-loss velocity estimate (Figure 4.7a).

4.6 Conclusions

The highly salinised floodplains of the Murray River are geophysically challenging areas to work in, as the shallow groundwater is often as conductive as seawater, resulting in very little signal penetration for electrically based geophysical techniques. Nevertheless, with appropriate processing EMI and GPR surveys have the potential to provide useful information in this environment. For TEM surveys this involves careful use of smooth-model and discrete-layer inversions. For GPR surveys it requires careful attention to system geometry, assumptions about low-loss conditions and use of appropriate equations when solving for phase velocity and depth. Even when these details are accounted for in the GPR processing, the results are only an incremental improvement over those derived from the application of conventional processing. Nevertheless, comparison with TEM results for the area suggests that the improvement is sufficient to make these data potentially more useful. Overall, when these data sets are processed carefully they complement each other and have the prospect of improving our overall understanding of floodplain hydrogeology in this study area.

More specifically, this paper has examined a number of issues relating to the processing of low-frequency GPR data. They include:

- When estimating phase velocity using the equation based on the full-solution to the wavenumber, differences between the calculated surface layer velocity based on the TEM data, compared with those inferred from the GPR data have been noted. We have used the observed GPR surface layer velocity to estimate the surface layer thickness for a given GPR sounding and then reverted to TEM derived velocities for the remainder of the sounding. It is also important to incorporate GPR system geometry in these depth calculations, as the large separation between the transmitting and receiving antennae, if unaccounted for, can contribute to inaccurate depth estimates, particularly in the top few metres.
- It is possible to estimate surface layer conductivity from GPR data under certain conditions. In the example shown here, the thickness of this layer based on the depth to the first reflector in the GPR data is similar to the thickness of the top layer for much of the inverted TEM data. This layer is, nevertheless, more resistive than that shown in the TEM.

- Under transition-band conditions, variations in permittivity do not have much effect on phase velocity and therefore on depth estimation in the GPR data sets.
- Under transition-band conditions, variations in permittivity have a relatively large effect on the conductivity of the surface layer defined by the GPR.

Three methods of introducing conductivity information to the phase velocity estimation calculations were explored for GPR data collected under transition-band conditions. The best results for depth estimation were obtained when direct ground-wave velocity information was combined with the results from the discrete-layer TEM inversion to define layer velocities. Use of a single, estimated value for the conductivity, combined with the GPR-derived surface layer gave poor results. Accounting for lateral variation in conductivity at a single depth, as for data from a LIN-based terrain conductivity meter produced intermediate results. All of these scenarios appeared to provide more credible results than from using phase velocity based on low-loss assumptions.

A number of shortcomings were noted in the methodology that we propose here for processing GPR data collected under transition-band conditions. Nonetheless, given the shallow depths of the data being processed, and the relative improvement over low-loss assumption processing, the processing method outlined here is worth further evaluation for data sets collected over other similar field areas.

Chapter 5

Interpretation of airborne and ground geophysical systems over conductive ground

M. A. Hatch, T. Munday, G. Heinson, K. Lawrie, J. Clarke, P. Mill, L. Halas

Geology and Geophysics, School of Earth and Environmental Sciences
University of Adelaide, Adelaide, SA 5005 Australia

Text in manuscript

STATEMENT OF AUTHORSHIP

Interpretation of airborne and ground geophysical systems over conductive ground

Text in manuscript

Hatch, M. A. (Candidate)
Developed concepts, wrote manuscript and acted as corresponding author.

I hereby certify that the statement of contribution is accurate

Signed …. .....*Date* 27 March 2011

Munday T.
Contributed to planning of article and provided critical evaluation.

I hereby certify that the statement of contribution is accurate and I give permission for the inclusion of the paper in the thesis

Signed .....*Date* 24th March 2011

Heinson, G.
Contributed to planning of article and provided critical evaluation

I hereby certify that the statement of contribution is accurate and I give permission for the inclusion of the paper in the thesis

Signed . .....*Date* 28/3/2011

Lawrie, K.
Provided funding for project and initial motivation for work to be performed.

I hereby certify that the statement of contribution is accurate and I give permission for the inclusion of the paper in the thesis

Signed ..... *.....Date* 28/3/11

Clarke, J.
Assisted with TEM data collection and initial discussions on data interpretation.

I hereby certify that the statement of contribution is accurate and I give permission for the inclusion of the paper in the thesis

Signed ..... *.....Date* 28/3/11

Mill, P.
Collected GPR data for project and initial discussions on GPR data processing.

I hereby certify that the statement of contribution is accurate and I give permission for the inclusion of the paper in the thesis

Signed …… *……..Date…27 March 2011…*

Halas, L.
Provided figures for upcoming Geosciences Australia report.

I hereby certify that the statement of contribution is accurate and I give permission for the inclusion of the paper in the thesis

Signed ..... *.....Date* 28/03/2011

5 INTERPRETATION OF AIRBORNE AND GROUND GEOPHYSICAL SYSTEMS OVER CONDUCTIVE GROUND

5.1 Summary

High-resolution geophysical techniques, whether ground-based or airborne, have the potential to provide information about floodplain processes, including important surface water/groundwater interactions and groundwater quality that can be valuable in the development of appropriate natural resource management strategies. In this study, we compare and contrast results from a coordinated surface and airborne geophysical program on highly conductive floodplains near Mildura, Victoria. Specifically we examine three transects from a high-resolution, time-domain electromagnetic (TEM) system, a low-frequency ground penetrating radar (GPR) system and a frequency domain helicopter electromagnetic (FDHEM) system, and consider their effectiveness for resolving floodplain characteristics, including the depth to water table, location of perched water lenses, and extent and location of flush zones near waterways. We compare the resolution of information defined by the three systems and examine whether the results from the two ground techniques could be combined to better inform the hydrogeology in this environment.

Data from the TEM and FDHEM systems were processed using standard 1D inversion routines, with conductivity depth sections prepared for each traverse. The GPR data were processed using a more complete definition for phase velocity than the commonly used low-loss equation, to more accurately estimate the depths to features on the floodplain.

Results from the TEM and FDHEM surveys are similar, with the TEM providing more resolution at the surface and the FDHEM providing more information at depth. The GPR results indicate that incorporation of a more appropriate method to calculate phase velocity is an improvement over standard, low-loss processing, and allows these data to be interpreted more reliably with the TEM and FDHEM data. Processed this way the GPR is limited to approximately the top 8 m, where it nevertheless appears to provide information about the depth to the surface capillary fringe, and the relative conductivity of the unsaturated zone and shallow groundwater.

5.2 Introduction

In 2007 approximately 24,000 line km of frequency-domain helicopter electromagnetic (FDHEM) data were acquired along a 450 km stretch of the Murray River from the South Australian border to Gunbower in Victoria, for the River Murray Corridor Project (Lawrie et al.,

2008). These data were collected to help characterise the near-river environment, specifically to quantify the risk of salinisation to the river and the adjacent floodplains. As part of this investigation, three transects of ground geophysical data were also acquired for comparison with the airborne data set in one section of the floodplain. Along each transect coincident sets of high-resolution time-domain electromagnetics (TEM) and low-frequency ground penetrating radar (GPR) data were collected. This paper examines the three geophysical data sets in order to: a) compare the scale of information defined in the ground data against that presented in the FDHEM; and b) establish if these data sets could be interpreted together to improve understanding of floodplain dynamics at finer scales, concentrating especially on the GPR data, as very little of this type of information has been collected over conductive ground.

There has been a perception that geophysical techniques based on electromagnetic induction (EMI) techniques, especially airborne EM (AEM), would not provide useful data in highly conductive environments like the floodplains examined in this study. Anecdotally, it has been assumed first that signal attenuation would be so high that little useful information would be acquired, and then what little near-surface conductivity information was collected would not vary sufficiently, both laterally and vertically, to resolve features of interest over the survey area. Recent AEM surveys flown over conductive floodplains in Australia have shown that these perceptions are false, as illustrated in a number of studies over conductive floodplains in Australia (Munday et al., 2005; Fitzpatrick et al., 2007a; Munday et al., 2008),.

GPR has not been used in conductive settings either as it is known that the high-loss conditions that prevail in conductive settings would result in strong signal attenuation at normal operating frequencies and very little signal penetration. New systems have been designed that use lower frequencies (10 MHz to 100 MHz) in an attempt to image deeper in low-loss settings (Davis and Annan, 1989; Jol et al., 2002; Tallini et al., 2006; Tsoflias and Becker, 2008; Zeng et al., 2008; Franke and Utsi, 2009). Their introduction has raised the question as to how these systems perform in higher-loss, floodplain environments. It was anticipated that the main limiting factors in this environment would be that: a) the signal penetration would be limited due to attenuation in highly conductivity ground; and b) the relatively large pulse width of a low-frequency GPR system would limit resolution of thin layers. In Chapter 4 it is shown that to improve processing in this environment it is necessary to estimate phase velocity based on the full-solution of the wavenumber equation and not the low-loss version. Additionally, the equipment used for this survey had a large separation between the transmitter and receiver. As depths for this survey are small, processing data assuming normal incidence is incorrect, and it is necessary to correct for system geometry. For the purposes of comparing ground and airborne

results we have processed these data using the steps outlined in Chapter 4 and interpret the two EMI data sets and the GPR together.

5.3 Geological setting

The Murray Basin is an intracratonic basin that covers an area of approximately 300,000 square km, and is filled with mostly undeformed Cenozoic carbonate and terrigenous sedimentary rocks that make up the main hydrogeological units (Brown and Stephenson, 1991).

The unit of primary interest on the alluvial floodplain (immediately adjacent to and under the river) is the Coonambidgal Formation, which in this area is made up multiple generations of overlapping sets of meander belts of the river. Lithologically it is made up of interbedded sands and silts, with drapes of clays overlying parts of the floodplain. The surface morphology of the Coonambidgal in this area is related to the distance of the floodplain from the river. As the distance from the river increases (associated with increasing floodplain age) the relief of the buried scroll bars decreases, and the thickness of the clay cover increases (Clarke et al., 2010). This change in surface roughness can often be observed on the TEM and GPR sections as the topography has been superimposed on the sections.

The Terrace unit, furthest from the river, and topographically above the floodplain, consists of older (Pleistocene) alluvial deposits 2 to 4 m above the level of the modern scroll plain (Clarke et al., 2010). The Pleistocene-aged Blanchetown Clay and the Pliocene-aged Loxton-Parilla Sands underlie much of the floodplain and the basin and are usually the next units below the Coonambidgal. These units are typically 10 to 12 m deep (Clarke et al., 2010).

The water table occurs at 2 to 5-m depth. Groundwater in this area is often very saline, with conductivity values ranging from less than 100 mS/m in fresh areas to more than 5000 mS/m over much of the salinised floodplain (Aquaterra, 2010). Figure 5.1 is a low resolution image of groundwater salinity in this area (Murray Darling Basin Commission, 2002) highlighting that much of the area is underlain by groundwater nearly as saline as seawater (approximately 3270 mS/m or 0.31 ohm-m). Groundwater may be less saline in the immediate vicinity of the river or other smaller water courses associated with the Murray River, resulting in flush zones in the otherwise saline groundwater (Murray Darling Basin Commission, 2003; Overton et al., 2006; Lawrie et al., 2008).

NOTE:
This figure is included on page 113 of the print copy of the thesis held in the University of Adelaide Library.

Figure 5.1. Groundwater salinity of the study area in south-central Australia, highlighted on the location map with a red polygon. RMC AEM data grid is shown in grey. The areal extent of the floodplains around the Murray are highlighted with green stippling. The Murray River is the boundary between New South Wales and Victoria, as well as for the offset section of South Australia. The TDS of seawater is approximately 35,000 mg/L (Murray Darling Basin Commission, 2002).

The locations of the three ground-based survey lines are shown in Figure 5.1. These data sets were acquired along roads or tracks that intersected zones of interest along each traverse. The outline of the FDHEM data set collected over this area is highlighted in grey. The AEM flight lines are not coincident with the ground data, so AEM results are interpolated to the ground-data locations, from the gridded, inverted FDHEM data set.

5.4 Geophysical data acquisition and processing

5.4.1 Airborne electromagnetics

The FDHEM data for this study were acquired in 2007 using Fugro Airborne Surveys RESOLVE FDHEM system. For the RESOLVE system, the transmitting and receiving antennae are housed in a "bird" slung approximately 30 m below a helicopter. Terrain and obstacle permitting, the bird is flown at an elevation of 30 m above the ground at a speed of 120 to 130 km/h. At this speed, data are collected at approximately 3-m intervals along the flight path. Data

were acquired at six frequencies: nominally 400Hz, 1800 Hz, 3300 Hz, 8200 Hz, 41 kHz, and 140 kHz. Five of the six receiver-transmitter coil pairs in the bird collect data in the horizontal coplanar orientation, with the 3300 Hz coils configured in the vertical coaxial orientation.

For this study the RESOLVE FDHEM data were inverted using Brodie and Sambridge's (2006) holistic inversion. This inversion routine produces quasi-3D conductivity models, based on a computationally efficient 1-D forward modelling algorithm. The holistic inversion uses the raw, uncalibrated, uncorrected data and then combines all of the data processing and inversion into one large, simultaneously solved inversion problem (Brodie and Sambridge, 2006). This routine treats all of the variables that are difficult to control for, but that contribute to the drift corrections that standard FDHEM data processing make, and solves for them by making them unknowns in the inversion routine. This is accounted for by treating the data as a spatial whole, taking advantage of inter-frequency and spatial coherence in the FDHEM data set. The result is an inverted conductivity model that is both laterally and vertically smooth. Information from geophysically logged bores is included in the inversion as *a priori* information to constrain conductivities in the vicinity of each the borehole.

For the FDHEM data set shown in this paper, the survey area was regularized into 40 m x 40 m squares, with thicknesses varying logarithmically with depth. The shallowest layer was set to a thickness of 2 m, increasing to approximately 10-m thickness in the 18th layer, for a total depth of approximately 90 m. After inversion, the gridded FDHEM results were interpolated to the three line locations, based on the GPS locations from the GPR lines. Conductivity-depth sections were then prepared, which were draped over topography.

5.4.2 Towed TEM

The TEM system used for this survey work was Zonge Engineering's NanoTEM system. This is an inductive electromagnetic geophysical technique developed in the early 1990's as a fast-sampling, shallow geophysical tool.

These data were acquired in February 2008. A 3 x 3 m transmitter/receiver frame was towed approximately 8 m behind a quad bike, collecting data at discrete time intervals (Figure 5.2a). The outside of the frame was set up as the transmitting antenna, with a triple turn of wire attached to the frame. The 1 x 1 m receiving antenna was mounted in the centre and was also made of a triple turn of wire. Data were acquired in a near-continuous mode, with the system sampling every two seconds, stacking 100 cycles at a repetition rate of 64 hertz. Towed at 5 to 10 km per hour, data were recorded at approximately 3 to 6-m intervals. Locational information coincident with TEM data acquisition was collected using a GPS unit.

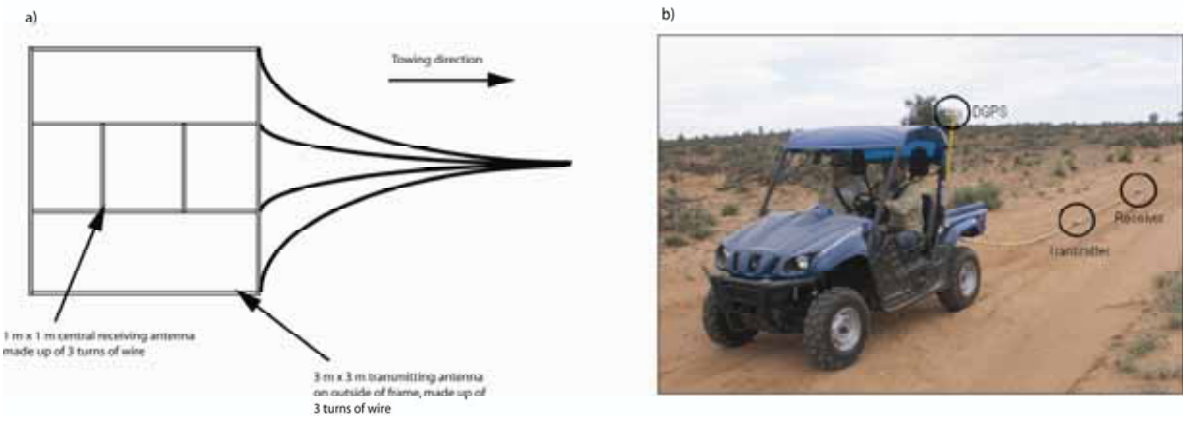

Figure 5.2. Equipment used for ground component of this study: a) schematic diagram of towed TEM system; and b) photo of GPR rig on site.

Following acquisition, the two data sets (TEM decays and GPS locations) were combined and the located TEM data set was inverted using two different 1D inversion routines: Zonge Engineering's smooth-model inversion routine STEMINV and the University of Aarhus' EM1DINV program, used here as a discrete-layer inversion.

The results for the smooth-model inversion and the discrete-layer inversion were then stitched together into separate sections, draped over topography (based on the high-resolution GPS data collected with the GPR data) and are presented as conductivity depth sections.

The 1D model assumption used in the inversions is mostly valid in the sub-horizontal, layered sedimentary settings that are encountered in the study area, where it produces results that are only slightly distorted by 2D or 3D effects that could be induced by marked changes in substrate topography, faults, fractures, or other short wavelength geological phenomena.

5.4.3 Ground penetrating radar

Data for this survey were acquired using the Mala ProEx GPR controller unit, and the Mala 25 MHz unshielded RTA antenna, towed behind a two-seater quad bike (Figure 5.2b). The offset between the transmitting antenna and the receiving antenna was 4 m with data recorded at 0.5 second intervals, stacking 4 readings. The system was towed at 5 to 10 km per hour, with data recorded at approximately 0.7 to 1.4-m intervals. GPS data were collected simultaneously with the GPR data. This survey was conducted in late January and early February 2008.

It should be noted that the transmitter and the receiver on the Mala RTA system are oriented in a collinear rather than the more conventional parallel setup, thereby making the system "towable" (Figure 5.2b). While this is convenient for efficient data collection in the field, due to the shape of the transmitted field data collected using this orientation are more affected by features that are offline, than when collected using the parallel setup (Annan, 2005a).

Initial data processing was undertaken using the REFLEXW program. The data were: 1) resampled to 2-m station increments; 2) signal offset corrected (i.e. dewowed); 3) bandpass filtered (with cut-offs at 5, 15, 55 and 75 MHz); and 4) diffraction stack migrated (to minimize direct air-wave effects only as the antennae are not shielded). Two-way travel times were then converted to depths using software written for this project. After calculating depths, the data were then draped over topography, based on high-resolution GPS data collected with the GPR data, and the results presented as depth sections.

5.4.3.1 GPR Data Processing

In Chapter 3 it was shown that the loss tangent is important when evaluating whether the conditions for a given GPR survey are suitable for evaluation using the low-loss estimate for phase velocity. The loss tangent is given by Equation 5.1.

$$\tan\theta = \frac{\sigma}{\varepsilon\omega} \qquad (5.1)$$

where σ is the electrical conductivity (S/m), ε is dielectric permittivity (F/m). For convenience we note that ε is often expressed as $\varepsilon_0\varepsilon_r$, where ε_0 is the permittivity of free space (8.854 x 10^{-12} F/m) and ε_r is the (dimensionless) relative dielectric permittivity.

The phase velocity based on low-loss assumptions is given by Equation 5.2.

$$v = \frac{1}{\sqrt{\mu\varepsilon}} \qquad (5.2)$$

where μ is the magnetic permeability (H/m). μ is often expressed as $\mu_0\mu_r$, where μ_0 is the magnetic permeability of free space (4π x 10^{-7} H/m) and μ_r is the relative magnetic permeability.

In Chapter 3 conditions are low-loss when the loss tangent is less than 0.2. Under low-loss conditions it is appropriate to use Equation 5.2 to estimate the phase velocity, which is only dependent on the dielectric permittivity. It is further stated that conditions are in the transition band between low-loss and quasi-static conditions when the loss tangent is between 0.2 and 103. Under these conditions it is more appropriate to use the phase velocity equation based on the complete solution to the wavenumber equation, given by Equation 5.3.

$$v = \frac{1}{\sqrt{\frac{\mu\varepsilon}{2}\sqrt{\left(1+\frac{\sigma^2}{\varepsilon^2\omega^2}\right)}+1}} \qquad (5.3)$$

where ω is angular frequency (given by $2\pi f$, where f is the system frequency).

Based on the TEM data acquired during this survey, the conductivity of the field area ranges from approximately 50 to 1000 mS/m (20 to 1 ohm-m). The GPR system used for this system operated at 25 MHz system. If we assume that the relative dielectric permittivity for this area is 11, which is a reasonable value for this type of environment (Reynolds, 1997; Scharma,

1997; Annan, 2005a), the loss tangent ranges from approximately 3 to 65, and a survey run under these conditions would be in the transition band between pure low-loss conditions and pure quasi-static conditions. It is therefore appropriate to estimate the phase velocity using Equation 5.3 and not use the low-loss approximation from Equation 5.2.

To estimate depths to reflections in the GPR data set, each GPR sounding is matched with its nearest TEM sounding. Phase velocities are estimated for each data sample, based on conductivity, using the full solution for the phase velocity (Equation 5.3). The phase velocity of the direct ground-wave arrival is used for all signal arriving before the first visible reflection. GPR signal magnitudes are then placed at the correct depth iteratively, using repeated applications of the two-way travel time equation (Blindow, 2009) shown in Equation 5.4, and Snell's law to account for ray-path refraction at layer boundaries, as described more fully in Chapter 4.

$$D = \sqrt{\left(\frac{t_{2way} * v}{2}\right)^2 - \left(\frac{H}{2}\right)^2} \qquad (5.4)$$

where D is depth, t_{2way} is the two-way travel time, $\boldsymbol{v}$ is the phase velocity, and H is the horizontal separation between the receiver and the transmitting antennae.

In Chapter 4 a method was outlined to estimate the conductivity and thickness of the surface layer based on the velocity of the direct ground-wave and the timing of the first reflection after the direct ground-wave. This processing step has been performed on the data sets acquired for this study, and the results overlain onto the TEM sections for comparison and analysis. In the conductive floodplain environment, the bottom of the GPR-derived surface layer has been interpreted in Chapter 4 as being the top of the capillary fringe (Cresswell and Shand, 2009), above the water table, where the soil water content is high enough for the signal to strongly attenuate. This will be discussed further in Chapter 5.6 (Discussion). The location of the first reflector after the direct ground-wave has also been highlighted in the GPR sections to indicate the depth of the top of the capillary fringe in the GPR data.

5.5 Results

Figures 5.3, 5.4 and 5.5 are detailed location maps showing the three transects examined in this study, with each transect overlain on a false colour image of the study area. Transect location is indicated using the 6-m depth slice from the smooth-model inversion of the TEM data sets. Showing their locations this way highlights the traverse's location, as well as the observed spatial patterns of conductivity at a depth at, or slightly below, the top of the water table. Examination of layer conductivity with a spatial perspective permits a qualitative correlation

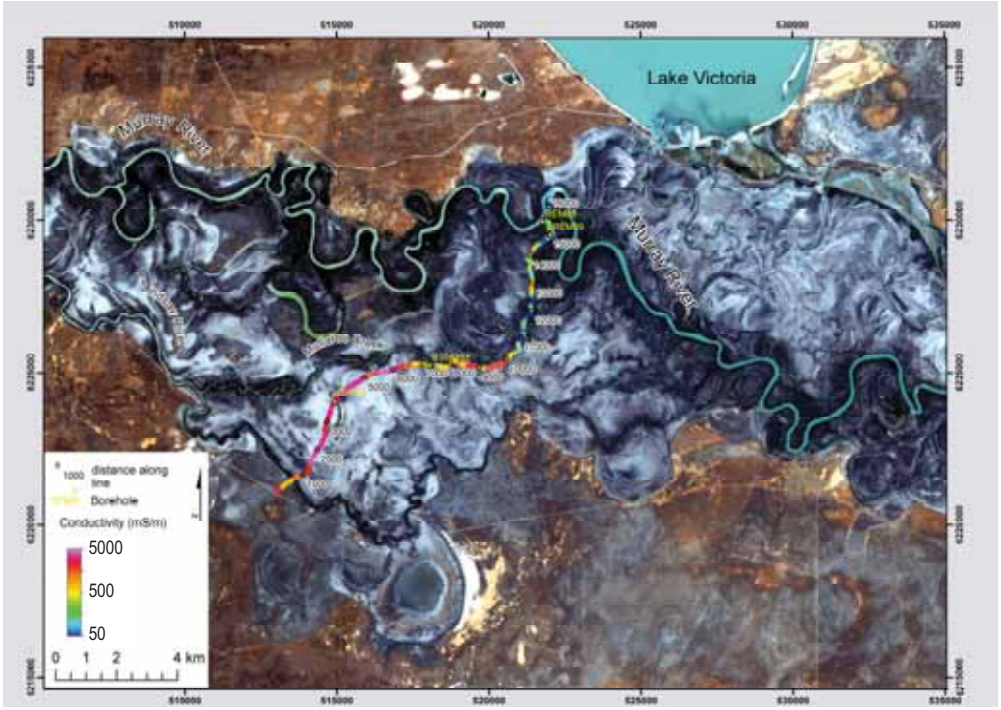

Figure 5.3. Detailed view of Lindsay Island transect. The underlying image is a false colour image showing regional land use and patterns. Line location is shown using 6-m depth slice of inverted TEM data. Distances along line and borehole locations are also shown.

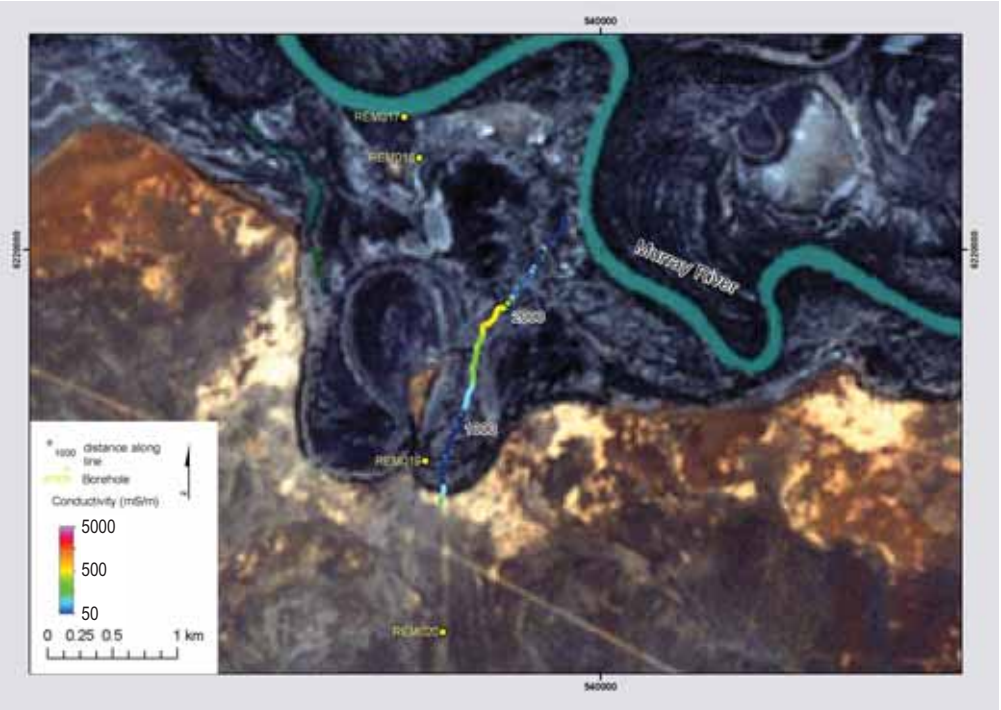

Figure 5.4. Detailed view of Potterwalkagee Creek transect. The underlying image is a false colour image showing regional land use and patterns. Line location is shown using 6-m depth slice of inverted TEM data. Distances along line and borehole locations are also shown.

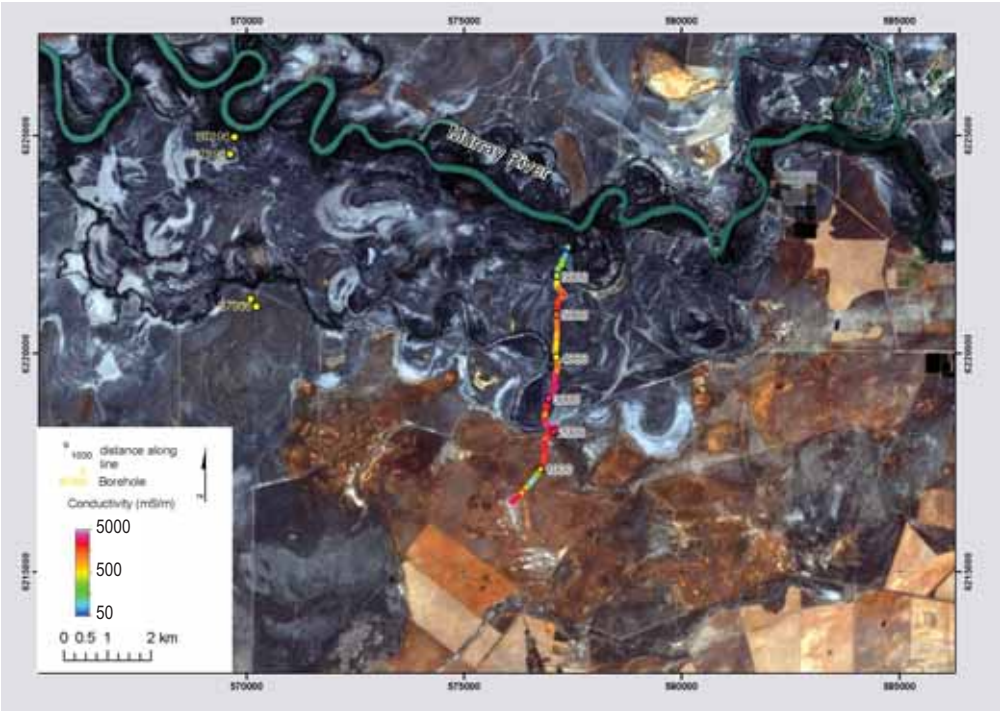

Figure 5.5. Detailed view of Walpolla Island transect. The underlying image is a false colour image showing regional land use and patterns. Line location is shown using 6-m depth slice of inverted TEM data. Distances along line and borehole locations are also shown.

between the observed conductivity and the proximity to other possible drivers of salinity variation to be made. Distance along each traverse is shown on each map, as well as the locations of the boreholes used for comparison.

A complete depth section for the Lindsay River line is presented in Figure 5.6, with more detailed sections presented in Figures 5.7, 5.8 and 5.9. The complete depth section for the Potterwalkagee Creek line is presented in Figure 5.10, while the complete depth section for Walpolla Island is presented in Figure 5.11. Shown on each figure is: a) the processed GPR data with location of the top of the capillary fringe as determined by the GPR highlighted with a black line; b) the inverted TEM section with the surface layer determined by the GPR superimposed over the TEM data; c) the inverted TEM section; and d) the inverted FDHEM data. In addition, Figure 5.6e shows the FDHEM data set to a depth of approximately 60 m. The regional water table elevation (Munday, personal comm.) is shown on each section as a grey line. Locations of flush zones based on interpretation of the GPR data are shown on section a) of each figure. Simplified hydrogeological interpretations are shown on section d) of each figure. Simplified bore logs from the 4 boreholes that are within 150 m of the traverses are superimposed at their approximate locations on each figure. Higher resolution images of the bore logs are presented in Figure 5.12.

Each bore log shows the logged lithological information for each bore, and also has a black line superimposed onto each log to indicate the depth to the top of the capillary fringe, based on the GPR data. Where available, groundwater depth and conductivity information is also included. Additionally, when the original bore logs supplied information about where moisture was encountered during drilling, this depth is indicated on each log with a dashed red line. This is interpreted as the approximate depth to the top of the capillary fringe.

There are a limited number of sources for borehole information in this area. Unfortunately this information is often contradictory, as terminology and procedures for data collection have varied over time. Additionally, these measurements may vary by season, as well as by year, depending on rainfall patterns and other factors. Efforts have been made to pick the best quality information, and cite all known data sources.

Bore log information for bore B7928 (Figure 5.7 and Figure 5.12a) was sourced from Thorne et al. (1990). The depth to groundwater information was collected from the on-line Victorian Water Resources Data Warehouse (2011b). The information shown here was gathered in December, 2006. Groundwater conductivity information is also available from this site but is limited and inconsistent, so is not presented here.

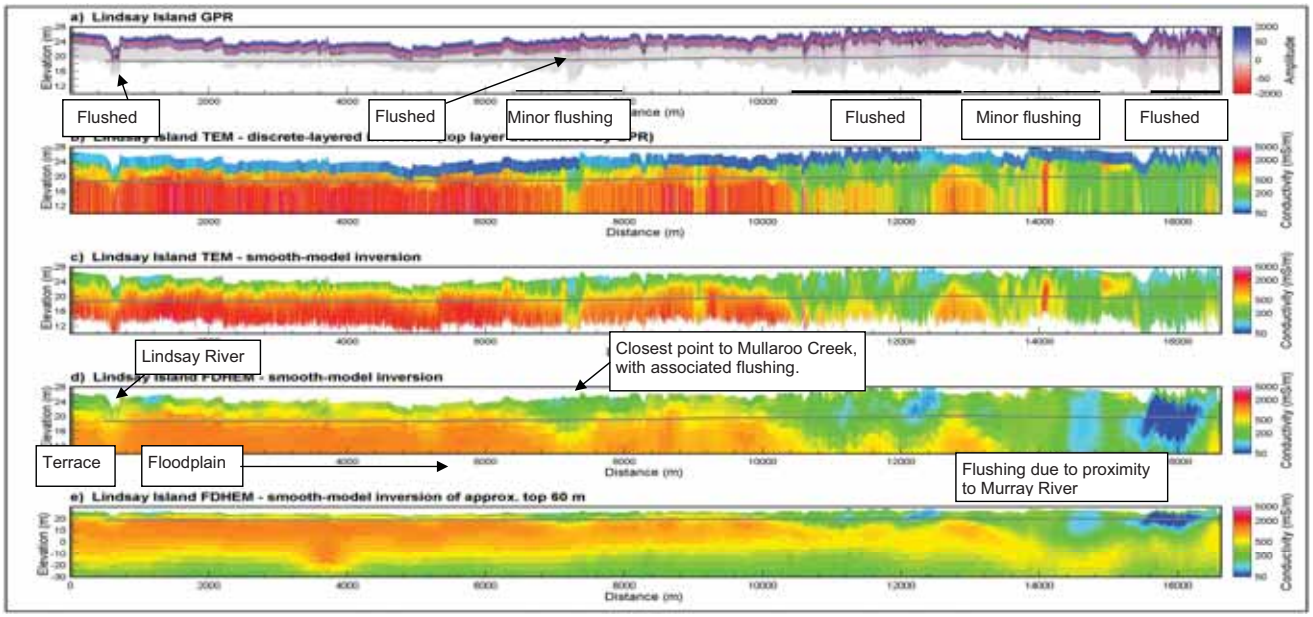

Figure 5.6. Depth section comparison of GPR, towed TEM and FDHEM for entire Lindsay Island data set: (a) processed GPR data; (b) inverted, towed TEM data with top layer information supplied by GPR; (c) inverted towed TEM data; (d) inverted FDHEM data; and e) inverted FDHEM, showing approximately the top 60 m. The vertical axis is elevation in metres. The horizontal axis is distance along profile in metres. Regional water level is indicated on each section with a grey line. Flushed zones are identified on the GPR section. Basic hydrogeological interpretation is highlighted on the FDHEM section (d). Location of the top of the capillary fringe based on GPR information is indicated on the GPR section with a black line.

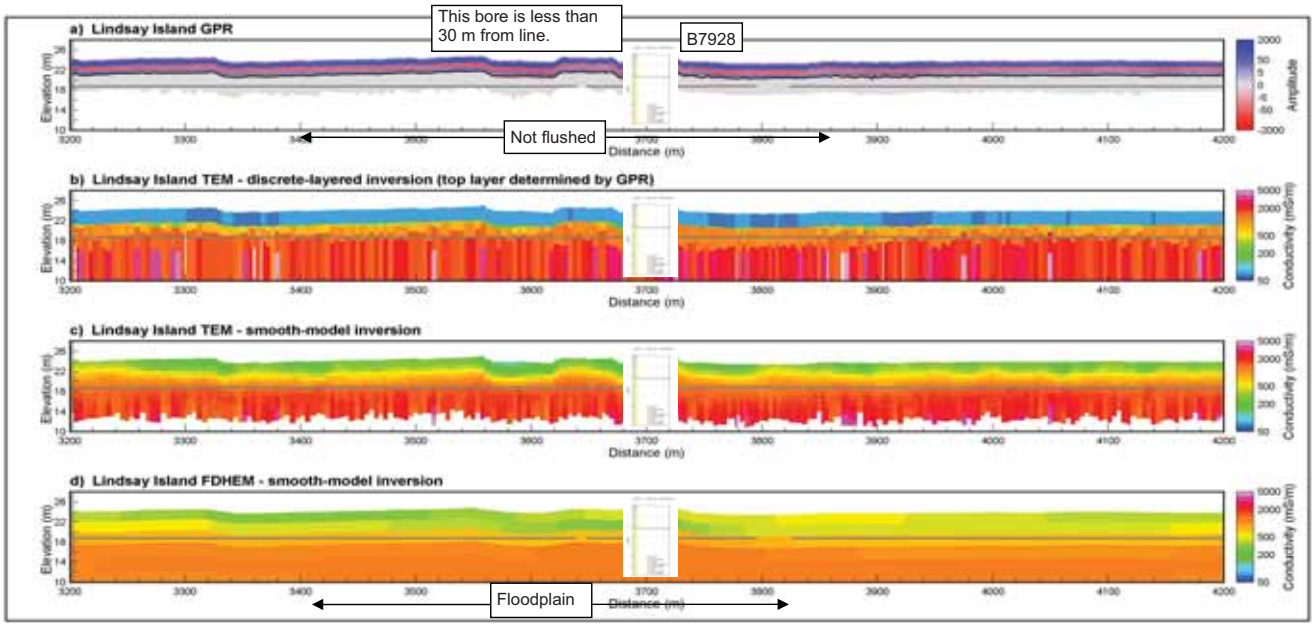

Figure 5.7. Depth section comparison of GPR, towed TEM and FDHEM for Lindsay Island data set, from station 3200 to 4200: (a) processed GPR; (b) inverted TEM data with top layer information supplied by GPR; (c) inverted TEM data; and (d) inverted FDHEM data. The vertical axis is elevation in metres. The horizontal axis is distance along profile in metres. Regional water level is indicated on each section with a grey line. Bore logs are superimposed on all sections, with depth to watertable indicated with a blue line, and approximate top of the capillary fringe with a red line. Flushed zones are identified on the GPR section. Basic hydrogeological interpretation is highlighted on the FDHEM section. Location of the top of the capillary fringe based on GPR information is indicated on the GPR section with a black line.

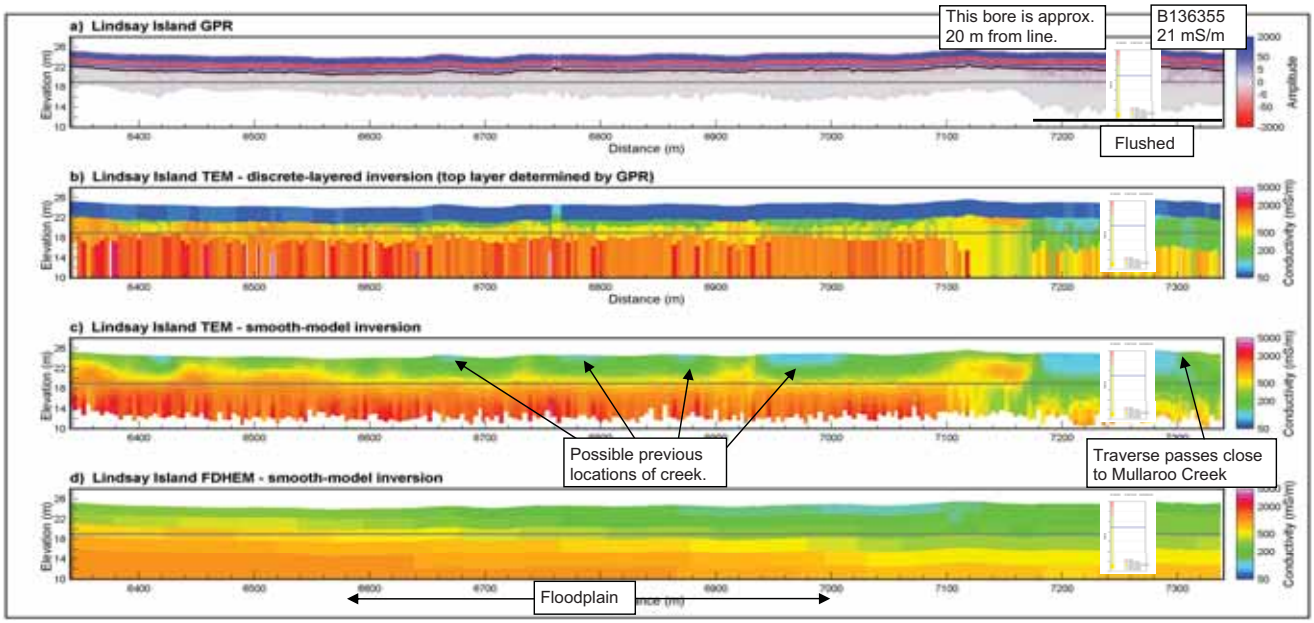

Figure 5.8. Depth section comparison of GPR, towed TEM and FDHEM for Lindsay Island data set, from 6340 to 7340: (a) processed GPR; (b) inverted TEM data with top layer information supplied by GPR; (c) inverted TEM data; and (d) inverted FDHEM data. The vertical axis is elevation in metres. The horizontal axis is distance along profile in metres. Regional water level is indicated on each section with a grey line. Bore logs are superimposed on all sections, with depth to watertable indicated with a blue line, and approximate top of the capillary fringe with a red line. Flushed zones are identified on the GPR section. Basic hydrogeological interpretation is highlighted on the FDHEM section. Location of the top of the capillary fringe based on GPR information is indicated on the GPR section with a black line.

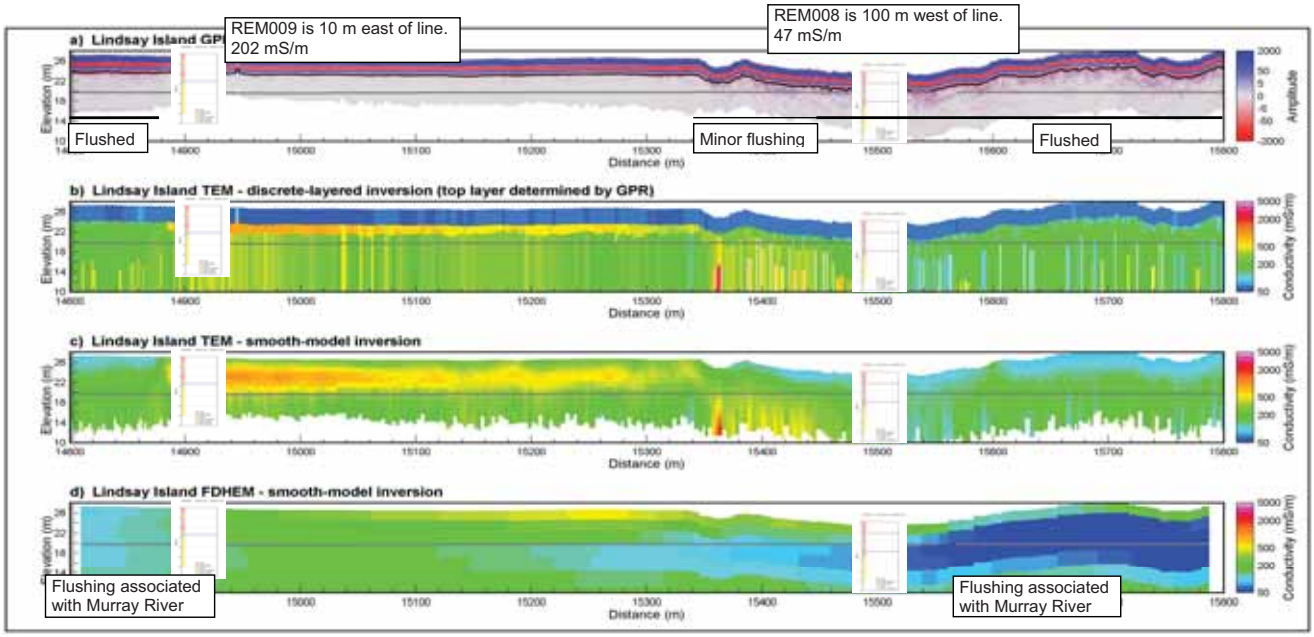

Figure 5.9. Depth section comparison of GPR, towed TEM and FDHEM for Lindsay Island data set, from 14800 to 15800: (a) processed GPR; (b) inverted TEM data with top layer information supplied by GPR; (c) inverted TEM data; and (d) inverted FDHEM data. The vertical axis is elevation in metres. The horizontal axis is distance along profile in metres. Regional water level is indicated on each section with a grey line. Simplified bore logs are superimposed on all sections, with depth to watertable indicated with a blue line, and approximate top of the capillary fringe with a red line. Flushed zones are identified on the GPR section. Basic hydrogeological interpretation is highlighted on the FDHEM section. Location of the top of the capillary fringe based on GPR information is indicated on the GPR section with a black line.

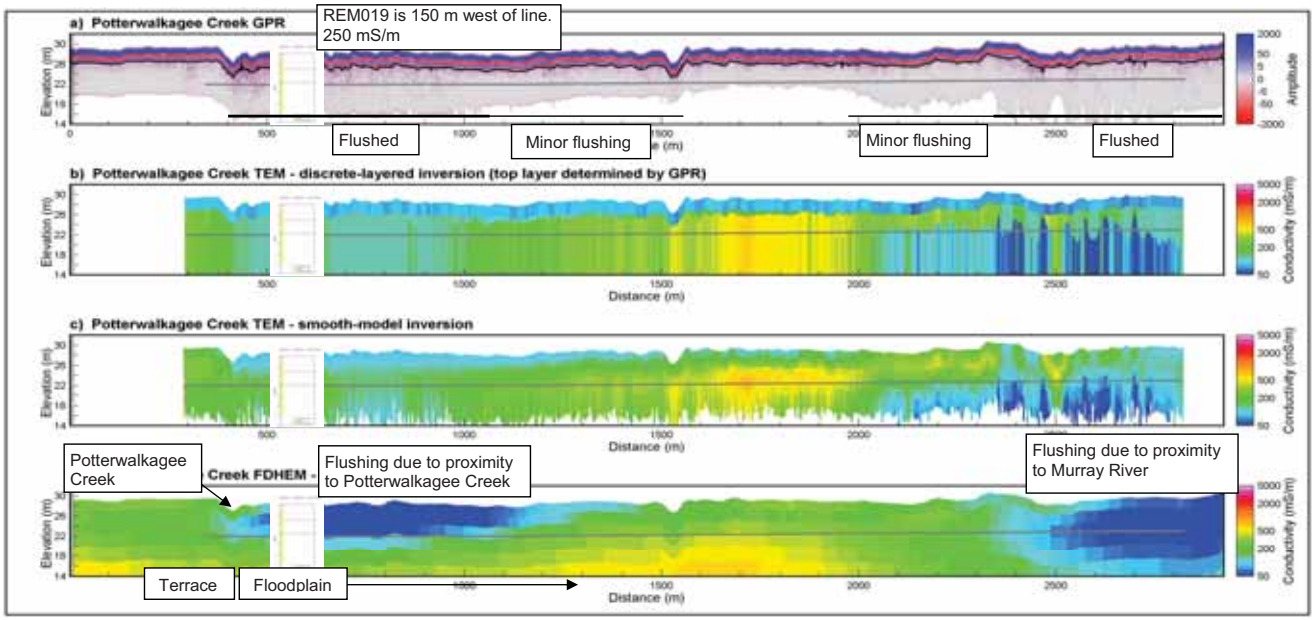

Figure 5.10. Depth section comparison of GPR, towed TEM and FDHEM for entire Potterwalkagee Creek data set: (a) processed GPR; (b) inverted TEM data with top layer information supplied by GPR; (c) inverted TEM data; and (d) inverted FDHEM data. The vertical axis is elevation in metres. The horizontal axis is distance along profile in metres. Regional water level is indicated on each section with a grey line. Simplified bore logs are superimposed on all sections, with depth to watertable indicated with a blue line, and approximate top of the capillary fringe with a red line. Flushed zones are identified on the GPR section. Basic hydrogeological interpretation is highlighted on the FDHEM section. Location of the top of the capillary fringe based on GPR information is indicated on the GPR section with a black line.

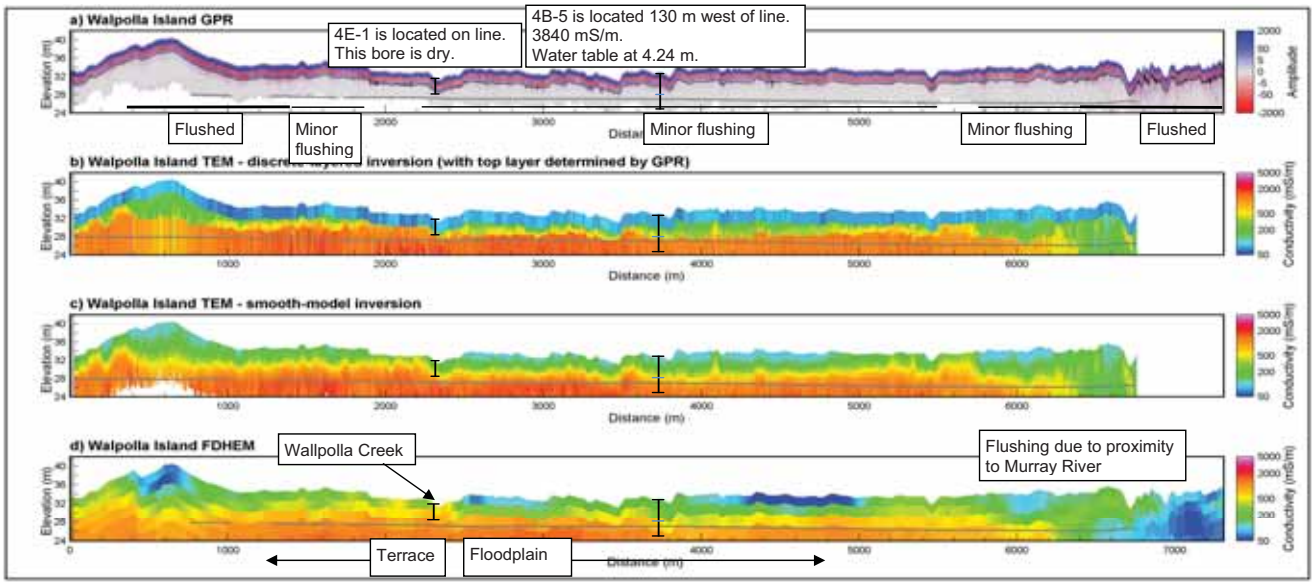

Figure 5.11. Comparison plot of GPR, towed TEM and FDHEM for entire Walpolla Island data set: (a) processed GPR; (b) inverted TEM data with top layer information supplied by GPR; (c) inverted TEM data; and (d) inverted FDHEM data. The vertical axis is elevation in metres. The horizontal axis is distance along profile in metres. Regional water level is indicated on the each section with a grey line. No bore logs were available for 4E-1or 4B-5, but groundwater depth and conductivity information was. This is superimposed on the sections at their approximate locations. The blue line on the 4B-5 marker indicates the water table location. Flushed zones are identified on the GPR section. Basic hydrogeological interpretation is highlighted on the FDHEM section. Location of the top of the capillary fringe based on GPR information is indicated on the GPR section with a black line.

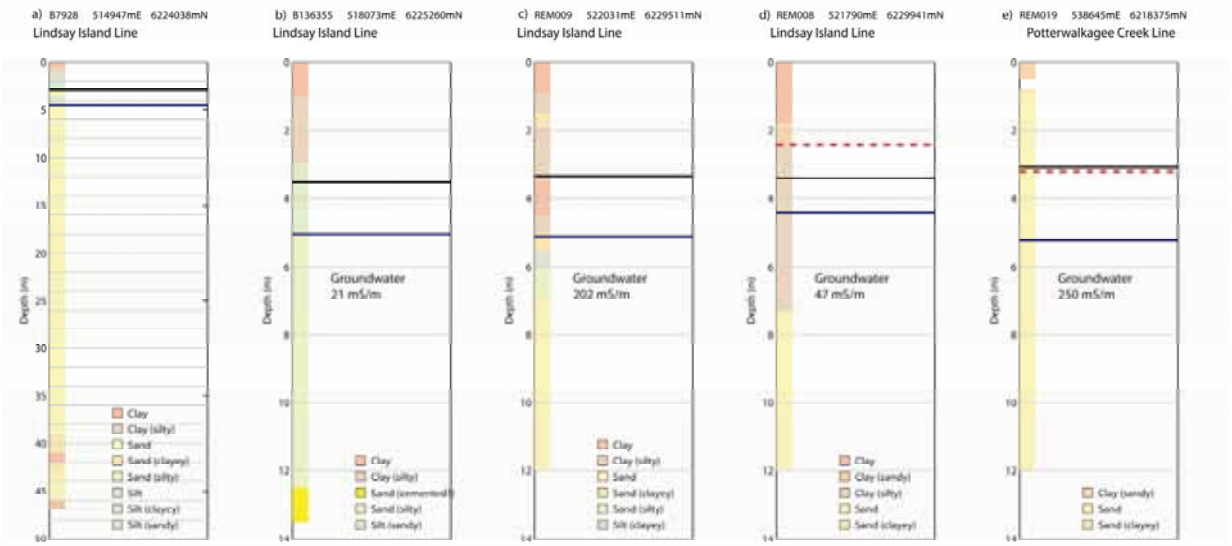

Figure 5.12. Detailed logs of bores presented in Figures 5.7 to 5.9. On each log, water table depth is indicated with a blue line. Where original bore logs supplied information about where moisture was encountered during drilling, this depth is indicated with a dashed red line. This depth is interpreted as the approximate depth to the top of the capillary fringe. The black line indicates the depth to the top of the capillary fringe, as interpreted from the GPR data. Note that the full log for B7928 extends to 50-m depth.

Bore log information for B136355 (Figure 5.8 and Figure 5.12b) was sourced from the on-line Victorian Water Resources Data Warehouse (2011a). Groundwater depth and conductivity information was sourced from Aquaterra (2010). Similar groundwater depth and conductivity information is also available from the Victorian Data Warehouse website.

Bore log information for REM008, REM009 and REM019 (Figure 5.9, 5.10 and Figure 5.12) was sourced from two unpublished reports supplied to Geoscience Australia (Kellett, personal comm.). Groundwater depth and conductivity information was sourced from Aquaterra (2010). No bore logs were available for 4E-1 and 4B-5. Groundwater depth and conductivity information was sourced from Aquaterra (2010).

Examination of the geologic bore logs in Figure 5.12 suggests a pattern that is consistent with the regional hydrogeological description provided in Chapter 5.3 (Geological Setting). Each shows variable thicknesses of clays, sandy clays, silts, silty sands (i.e. clay drape) to a depth of less than 1m to greater than 7 m, overlying relatively clean sands to depth. This is important to the geophysical interpretation, as this consistency in the near-surface geology is not reflected in the variability of the EMI and GPR data sets.

On Figures 5.6 to 5.11 the grey line indicating the elevation of the regional water table (Munday, personal comm.) on each section does not always match the water table level indicated on each bore log. Two possible explanations are that: a) the dates of data collection are different for the regional water table and each log; and/or b) the regional water table is a “best fit” surface based on water elevation from many of the bore logs in the area, and as a result may not fit the actual measured water elevation at a given location.

Figure 5.13 compares the downhole induction log for Bore B7928 with results from the nearest TEM and FDHEM soundings. The bore conductivity data were acquired in October 2006. This bore is located less than 30 m from the nearest TEM sounding and approximately 50 m from the nearest FDHEM sounding. There is relatively good correlation between conductivity values derived from the three surveys near the surface, suggesting that the induction tool, the ground TEM and the FDHEM are resolving similar information, and that the 1D approximations that form the basis for the inversion routines used to process these data, are essentially correct. The ground TEM data appear to overestimate the borehole-derived conductivities at depth, while the FDHEM follows the borehole conductivities very well. Brodie (personal comm.) indicated that in the vicinity of the borehole the downhole data are constraining the inversion results, and that fits for soundings further from the borehole were not likely to be as good. Comparison with FDHEM

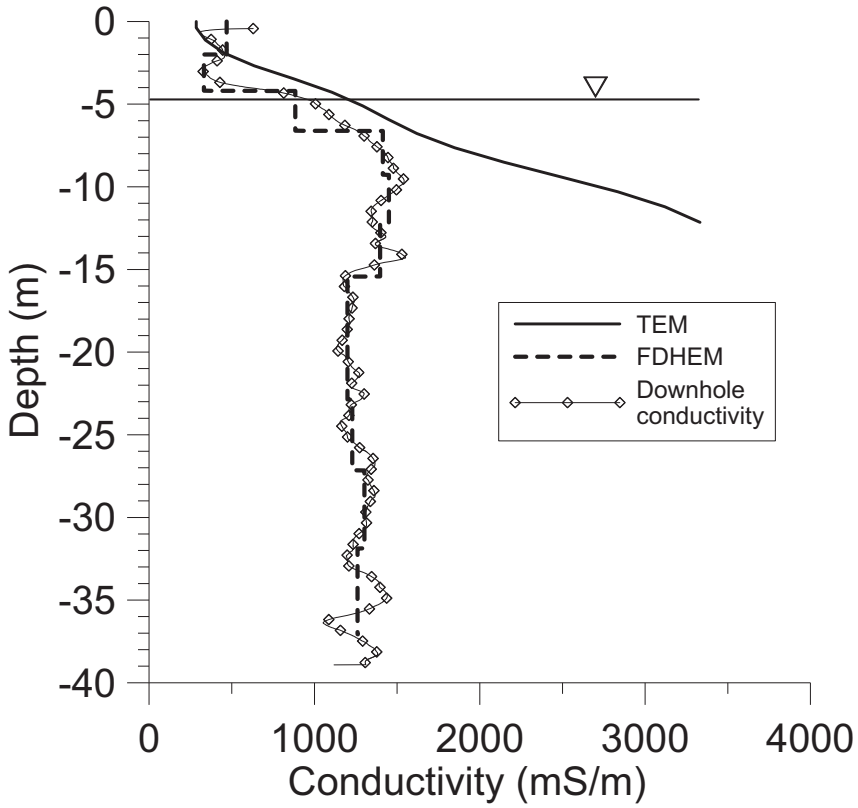

Figure 5.13. Borehole conductivity log for Bore B7928 located at approximately station 3700 on Lindsay River line compared with the TEM smooth-model inversion sounding and the FDHEM smooth-model inversion for the nearest station (<30 m). The TEM conductivities diverge significantly from the borehole conductivities at depth. Approximate depth to water table indicated with black triangle.

soundings further from the borehole suggests that 25 m may be the approximate depth of investigation for the FDHEM in this area. Based on an FDHEM survey run over a similarly conductive floodplain (this time in South Australia), using the same system, Viezzoli et al. (2010) report that 15 m is the approximate depth limit for this system, based on depth of investigation calculations (Christiansen and Auken, 2010). For the TEM data shown in Figure 5.13, the sounding shape is relatively similar to the other two sets of data to a depth of 8 to 10 m, suggesting that this is the approximate depth of investigation for the TEM in this area.

Figure 5.14 compares the inverted regional FDHEM data set with the ground TEM data. For the FDHEM, the averaged conductivity value over the interval from 5 to 10-m depth is shown. For the ground TEM, the 6-m depth slice is shown. There is generally good correlation between the two data sets with the ground TEM appearing to show more detail than the FDHEM.

Figure 5.15 is a map of tree health in the vicinity of the Lindsay Island traverse, based on

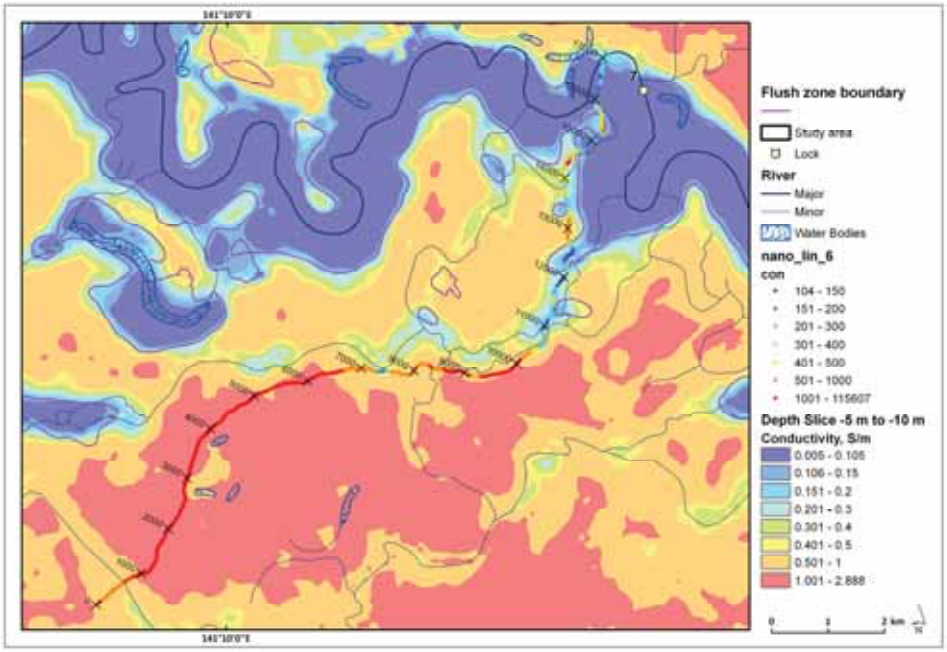

Figure 5.14. Image comparing inverted regional FDHEM data set, depth slice at 5- to 10-m depth, with 6-m depth slice of ground TEM data set as overlay.

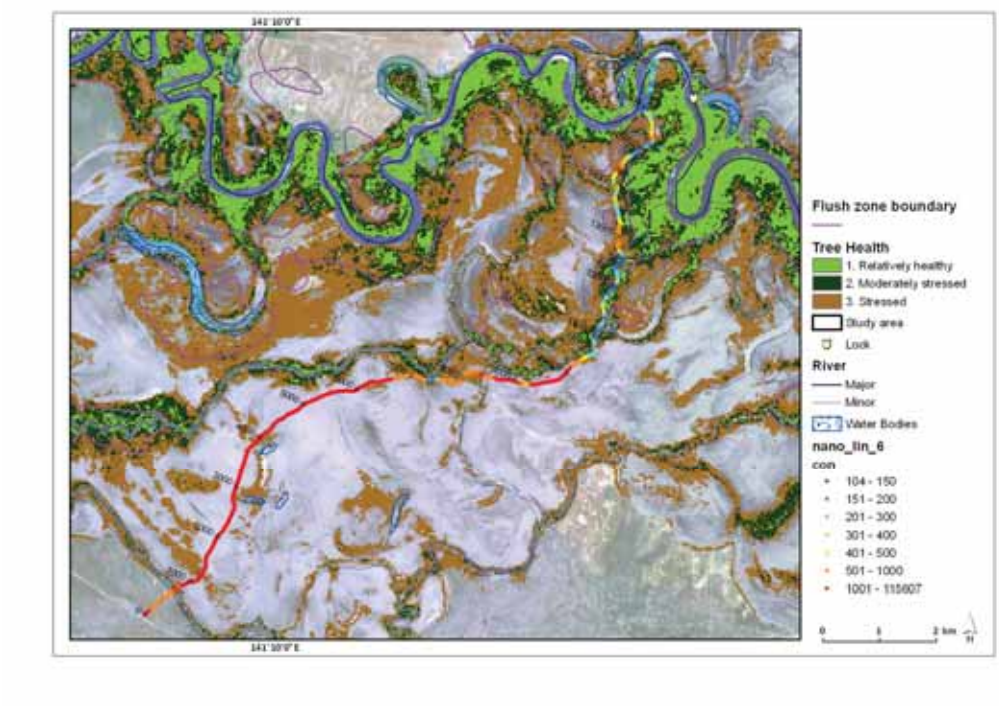

Figure 5.15. Image comparing map of derived tree health with 6-m depth slice of ground TEM data set as overlay.

Landsat image analysis, with the 6-m depth slice from the inverted ground TEM data set overlain to demonstrate the correlation between tree health and ground conductivity. The Normalized Difference Vegetation Index (NDVI) shown here is produced by combining information from two different wavelengths of data from Landsat images (Elmore et al., 2000). We expect tree health to improve with proximity to fresher water like the Murray River and associated waterways. Similarly, we expect conductivity to be lower where groundwater is fresher, and therefore, that conductivity should be lower in areas where tree health is good.

Figure 5.16 is a map of flush zone location and thickness, based on the inverted FDHEM data, with the 6-m depth slice from the inverted ground TEM data set overlain to demonstrate the correlation between patterns in the conductivity and the FDHEM-derived flush zones. Flushed zone information was obtained by preparing conductivity elevation slices of the area from the inverted FDHEM data set to a depth of 25 m, and then locating zones in these maps where the conductivity was less than 105 mS/m, corresponding with groundwater defined as slightly brackish to fresh (Lawrie et al., 2008). The black line surrounding the colour zones in Figure 5.16 outlines the extent of the flush zone with thicknesses indicated by the colour key. Flushed zones based on the interpretation of the ground TEM and the GPR data sets are indicated with labelled circles on this figure. It is apparent from Figure 5.16 that all of three techniques have located the significant flush zones, while the ground techniques additionally highlight the location of a number of smaller flush zones.

5.6 Discussion

5.6.1 Expected EMI response

Where the groundwater is saline, we expect the response from the EMI systems to be mostly conductive to depth, as the response from the saline groundwater overwhelms the response from the sands and clays. Above the water table we expect the thickness of the capillary fringe to vary with clay content (Cresswell and Shand, 2009), with the finer pore space in clays allowing the water to rise higher above the water table than in coarser sands. Dry clays and sands above the capillary fringe should be resistive, while moist clays and sands in the capillary fringe should be relatively conductive. It is worth noting that clays are generally thought of as conductors relative to sands and most other near-surface materials. This is not always correct as dry clays are usually resistive and require some water in their matrix to be conductive (Keller, 1991). Therefore, it is reasonable to expect that the EMI response would reflect the level to

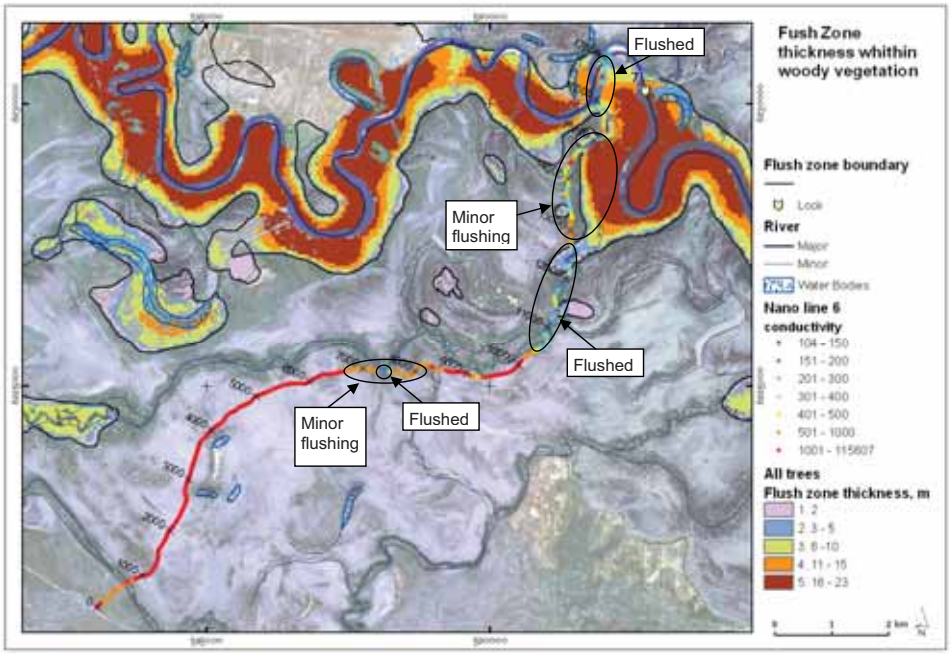

Figure 5.16. Image comparing derived map of flush zone location and thickness based on FDHEM inverted data set with 6 m depth slice of ground TEM data set as overlay. Location along TEM data track of flush zones interpreted from ground TEM and GPR have been super-imposed.

which water has risen above the water table due to capillary action to make the dry, near-surface soil sufficiently moist for the conductivity to increase. In this situation, the depth at which the conductivity changes from resistive to conductive should correlate approximately with the thickness of the capillary fringe above the water table. Where this fringe is thicker, the clay content of the floodplain sediments is expected to be greater and be correlated with an increase in conductivity.

Closer to the Murray River and the smaller, relatively fresh creeks associated with it, we expect the groundwater to be fresher, reflecting flushed conditions. In these areas, the EMI response beneath the water table level will be more resistive, compared with areas away from these flush zones where the groundwater is conductive. Potentially, the EMI response may also be influenced by texture (i.e. clay content), with higher conductivities in clay-rich zones than sandy zones. This may not be the case for at least some of the near-surface clays found in this environment, as a comparison of the bore log for REM008 (Figure 5.12d) and the associated EMI response (Figure 5.9c and 5.9d) suggests. This bore, located in a zone interpreted to be flushed on the Lindsay River line, shows significant clay content in the subsurface to deeper than 7 m, with the water table occurring at approximately 4.4 m depth and the GPR-derived capillary fringe depth occurring at 3.4 m. Examination of the EMI response in the area around this bore shows that the near surface is resistive from the surface to the bottom of the sounding. This suggests that the near-surface textural variation of the sediments is not influencing the EMI response in this area. Furthermore, it suggests that, at least near the ground surface, water conductivity is the most significant driver of near-surface conductivity. Hatch et al. (2003) made similar conclusions for TEM data collected over another floodplain, west of this field area.

5.6.2 Expected GPR response

For the GPR data sets, similar patterns to those observed in the EMI data sets are expected, although the reasons differ, as it is GPR signal attenuation that varies with substrate conductivity and is therefore the main parameter to evaluate. GPR signal attenuation is positively correlated with both clay and water content, with attenuation increasing with the conductivity of the water and clay content (Davis and Annan, 1989; Nobes et al., 2001; Jol et al., 2002; Giroux and Chouteau, 2010). At the surface, where the soil is dry, good signal strength and relatively strong reflectors are expected. At the top of the capillary fringe rapid signal attenuation is anticipated, with very little signal penetrating to depth, particularly if the soil has a significant moist-clay content or if the water in the pores is saline (or both). In zones that are flushed some attenuation at the top of the capillary fringe is likely, but we expect that the attenuation rate will be

less than over saline groundwater, resulting in slightly stronger reflections at depth. In Figures 5.6a to 5.9a the shallowest response visible on each plot is the strong direct ground-wave, interpreted to be occurring in the dry zone above the top of the capillary fringe. The black line on each GPR plot marks the location of the first reflector and has been interpreted as the top of the capillary fringe. Below this interface the rate of signal attenuation is related to the conductivity of the substrate. Where the groundwater is conductive the GPR signal attenuates rapidly, whereas where the groundwater is fresher the attenuation will be less rapid.

5.6.3 Interpretation

When the Lindsay Island data sections in Figures 5.6 to 5.9 are examined using these expectations of EMI and GPR behaviour as interpretation guidelines we see that from station 0 at the south end of the line to approximately station 10400, both the EMI and GPR data may be interpreted similarly. Both are essentially two-layer, with a variable thickness, dry, resistive surface-layer over a conductive layer extending to depth, interpreted to be response due to saline groundwater. Two smaller flush zones are seen in this section, coinciding with the location of the Lindsay River at station 650 and close proximity to Mullaroo Creek at station 7250. Neither feature is resistive enough to be highlighted in the flush zone location map (Figure 5.16) based on the FDHEM data.

Most of the traverse from station 10400 to the end of the line appears to be flushed, with much of the traverse running immediately adjacent to Mullaroo Creek and then approaching the Murray River. Examination of Figure 5.15 (tree health) and Figure 5.16 (flush zone location) confirms this, as tree health improves along the track as it progresses to the north, and the track skirts the edge of the large flush zone delineated by the FDHEM associated with the Murray River which cuts to the south immediately east of the traverse. The traverse continues slightly to the south, along Mullaroo Creek.

Interpretation of the EMI data sets is consistent with the GPR near the surface, but is more informative at depth, where the EMI signal is not attenuated and is able to show more variation. From station 10400 to 13200 the conductive layer noted earlier (interpreted as saline groundwater) from station 0 to 10400, appears to occur at greater depths, most likely due to partial flushing by the Mullaroo. From station 13200 to the end of the line the FDHEM indicates that the entire section is well flushed. The TEM and FDHEM data sets would be interpreted similarly, except for the zone from 13200 to 15200 where the TEM shows more variability than the FDHEM, highlighting shallow conductive zones of unknown origin in this area.

Examining Figure 5.10, the Potterwalkagee Creek line, using the same interpretive guidelines as those applied to the Lindsay Island line in Figures 5.6 to 5.9, we see that much of the ground covered in this transect appears to be flushed. Figure 5.4 shows that this traverse crosses Potterwalkagee Creek at the south end of the traverse, continuing north between two arms of the creek. This is interpreted as the flushing source for the south end of the traverse. The extent and degree of flushing at the north end of the line appears to strengthen as the traverse approaches the Murray River. Both of the EMI data sets and the GPR can be interpreted similarly.

Examining Figure 5.11, the Walpolla Island line, we see that much of this transect appears to be flushed in the near surface, with conductive ground water present at depth, as indicated in the EMI sections. This interpretation is consistent with the minimal bore data available on this line. The location of the top of the capillary fringe is again interpreted to be indicated by the location of the top of the first reflector, indicated with the black line on the section. For much of this traverse the top of the capillary fringe is more resistive than for the other two traverses. One interpretation is that the sediment composition along this line is different than in other parts of the study area, as this zone is generally conductive on the other two lines. This requires further investigation. Most of the traverse from station 5750 to the north end of the line appears to be flushed, as it approaches the Murray River. Both of the EMI data sets and the GPR can be interpreted similarly.

As discussed earlier, the conductivity and thickness of the surface layer based on the GPR have been calculated based on the method described in Chapter 4. The conductivity of this layer is calculated from the velocity of the ground wave, and the thickness is calculated from the surface layer velocity and the time to the first reflection after the ground wave. As noted in Chapter 4 the surface layer conductivities estimated in this way are generally lower than those shown in the TEM and FDHEM sections. Nevertheless, the thickness and character of the surface layer determined using this method is very similar to the same layer determined by the TEM alone, especially over areas interpreted to be underlain by saline ground water. For example, in Figure 5.6, the zone from station 0 to 10400 has been interpreted to be underlain by saline groundwater (compare Figures 5.6b and 5.6c), as has the entire section shown in Figure 5.7 (compare Figures 5.7b with 5.7c). Further to the north in Figure 5.6, the conductivity contrast between the surface layer and the deeper, flushed, resistive layer is not large enough for the depth to the top of the capillary fringe to be consistently apparent in the EMI sections. The GPR appears to define this layer well.

5.7 Conclusions

The highly salinised floodplains of the River Murray are geophysically challenging areas to work in, as the groundwater is often as saline as sea water, with very little electrical signal penetration. Nevertheless, EMI and GPR surveys are able to provide useful information in this environment, so long as the limits inherent in using EM systems under these conductive conditions are recognised. The data sets are complementary and together have the potential to improve the overall understanding of a study area. One of the main results of this work is that the GPR and ground-based TEM (and the FDHEM to a lesser extent) is interpreted to be providing information about the depth to the top of the capillary fringe. On a local scale, the ability to determine this depth non-invasively (even if only approximately), at relatively high resolution over local floodplain-scale areas, has potential to be of interest to a number of floodplain investigators, particularly those working on floodplain health and tree health. The depth to the top of the capillary fringe and the conductivity of the contained water informs directly on evapotranspiration rates and tree health. Similarly, mapping clay distribution and thickness in the near surface gives researchers information about the connection between surface water and groundwater during and immediately after rainfall/flooding events.

Overall, the FDHEM and TEM data sets provide similar interpretations for each of the survey areas. As expected, the lateral resolution from the ground TEM is significantly better than the FDHEM, while the FDHEM is able to provide information to greater depths. These results set up the typical conundrums for investigators working in these areas. How much resolution and depth is needed? When does the overall larger expense of an AEM survey with its lower per line-kilometre cost become more worthwhile than a ground survey with its relatively larger per line-kilometre cost? Realistically, the extra resolution provided by the ground-based techniques is likely only to be a driver for research-oriented surveys where this incremental improvement in resolution is needed. At this time, the acceptable resolution and extra depth provided by AEM surveys are likely to be the main drivers toward their use.

Overall the ground TEM data collected for this work appears to accurately map the difference between highly salinised groundwater and less salinised flushed zones to at least 8-m depth. Furthermore, the TEM provides information about conductivity variations in the top 5 m that is likely to be indirectly related to variations in mineralogy in that zone. Specifically, in this zone, variation in TEM response appears to be correlated with water content and conductivity in the soil, and not well correlated to soil mineralogy, including clay concentrations (which are usually expected to be positively correlated with conductivity). Nevertheless, where soil clay content is high, the thickness of the capillary fringe is greater than soils with less clay content.

This soil mineralogy variation is often seen in the TEM data as the variable depth to the boundary between the dry resistive surface layer and the top of the capillary fringe, which is moister and therefore often more conductive.

The GPR data appears to be supplying similar information to the TEM about the depth to the top of the capillary fringe. In areas where the groundwater is interpreted to be fresh, the conductivity contrast is often not sufficient for the TEM to be able to discriminate the top of the capillary fringe. The GPR appears to provide this information. Its ability to discriminate between saline and relatively fresh groundwater makes it a useful complement to the other techniques in determining the location and character of flushed zones along the traverses.

One of the important results to come out of this work is that, in the top 5 m, the EM response (both EMI and GPR) is dominated by the conductivity of the capillary water and, therefore, the groundwater. Lithological (textural) variation in the sediments does not appear to contribute noticeably to the EM response, other than in an indirect way, with the thickness of the capillary fringe apparently driven by the relative clay and sand content at that depth. Given that the near-surface response, expressed as either a conductivity response in the EMI or an attenuation step in the GPR, can be influenced by the presence of partially to fully saturated sediment in the capillary fringe zone suggests that the depth to the top of the water table may not, in many situations, have sufficient conductivity contrast to be seen in the EM data sets. Therefore, none of the techniques evaluated for this paper are able to determine the depth to the top of the water table.

Further investigation is needed to confirm that the GPR and TEM are providing real information about the depth to the top of the capillary fringe and mineralogical drivers for conductivity variation (if it exists). Additional bore information with moisture content information would assist the interpretation of the ground geophysical data.

6 THESIS SUMMARY AND CONCLUSIONS

6.1 Review by chapter

Chapter 2: A comparative study of in-river geophysical techniques for defining variations in riverbed salt load as an aid to managing river salinisation

For much of the Murray River, the conductivity of the layer immediately under the base of the river appears to be strongly correlated with whether the river is losing or gaining in that part of the river (Telfer et al., 2005; Tan et al., 2007). As much of the groundwater under the Murray is conductive (up to 5000 mS/m) and has the potential to add salt to the river under gaining conditions, it is important to identify even small gaining zones to assess their contribution to the overall salinity of the Murray. If significant, they are potential targets for the engineered removal of the saline water (salt interception schemes) to prevent saline groundwater entering the river (Forward, 2004).

Each of the three electrical geophysical techniques investigated in Chapter 2 provided useful information about this zone, consistently identifying relatively small losing and gaining stretches of the river. The two ground-based techniques provided better lateral resolution than the FDHEM while the FDHEM was generally able to provide deeper information. The lateral resolution or footprint of the ground-based TEM system varied from approximately 7.5 m at the surface to approximately 45 m at 20-m depth (the approximate depth limit for the TEM system). For the DC-resistivity system the shape of the footprint was elongated along line, with the along-line footprint varying from approximately 17 m in length at the surface to approximately 80 m at 20 m depth (also the approximate depth limit for the resistivity system). For the FDHEM system, the shape of the footprint was also elongated along line, with the along-line footprint largest at the surface, approximately 100 m in length. The FDHEM system was able to image to depths of between approximately 25 m and 60 m, where depth varies inversely with conductivity. The FDHEM system's ability to collect deeper information is useful as this may provide information about the interaction between surface and deeper aquifers in the system. Additionally, FDHEM has the advantage that it may be flown under all river conditions, while the two boat-based systems would not be used under full-flood conditions. Moreover, FDHEM may be flown over floodplains adjacent to the river, and is therefore able to provide contextual information, useful when interpreting river data. The FDHEM system is slightly handicapped as it is unable to measure water depth, which may reduce its usefulness for high-precision applications, such as

the evaluation of the effectiveness of salt interception schemes where relatively exact knowledge of the depth to the base of the river and the depth to deeper conductors is needed.

Chapter 3: The importance of the loss tangent and wavenumber: Implications for velocity and skin depth of low-frequency GPR and high-frequency EMI surveys

In this chapter the concept of the EM transition band was defined. The limits between low-loss and quasi-static behaviour that bound the transition band were also determined. Two methods to define these limits were considered. The more useful, from a practical perspective, is based on EM phase velocity comparisons. Limits on each zone in the frequency range between conditions that are dominated by conduction currents and displacement currents were defined by comparing the results between the low-loss and the full-solution phase velocity equations at the high-frequency end of the spectrum (greater than approximately 30 MHz), and the quasi-static and full-solution phase velocity equations at the low-frequency end of the spectrum (less than approximately 2 MHz). The ratios of the true velocity and the approximated velocity, over a range of conditions, were plotted against the loss tangent over the same range of conditions, highlighting the usefulness of the loss tangent as a parameter for discriminating between conditions that are low-loss, quasi-static or in the transition band. In practical terms, the band limits defined by the 5% error levels are likely to be the most useful to users of this type of information. Based on the 5% error levels, conditions are predominantly low-loss when the loss tangent is less than 0.7. Conditions are predominantly quasi-static when the loss tangent is greater than 9.7. Conditions are in the transition band when the loss tangent is between these values.

This chapter demonstrates that for frequencies that lie in the transition band, it is important to use the full solution of the wavenumber equation when calculating skin-depth or phase velocity. This is not trivial as this equation requires that more is known about the field area than is assumed when using the simpler versions of the same equations. In particular, for the low-loss version of the phase-velocity equation, the only variables are magnetic permeability, and dielectric permittivity; by comparison the full solution equation for phase velocity requires that conductivity information also be included.

Chapter 4: Combined processing and interpretation of ground penetrating radar and high-resolution time domain electromagnetics in a conductive setting

This chapter outlines a procedure for processing GPR data collected under transition-band conditions, based on the results from Chapter 3. This processing approach was applied to

a set of field data so that the results based on low-loss phase velocity processing could be compared with the results based on the full-solution processing scheme, and with the TEM data collected over the same traverse. Results based on the full-solution processing are better than those using the low-loss approximations, when compared with the TEM results. Discrepancies were noted between the observed GPR ground-wave velocity and the ground-wave velocity predicted by the TEM. These observations led to the development of a method whereby surface layer conductivity and thickness are estimated from the GPR data.

Chapter 5: Interpretation of airborne and ground geophysical systems over conductive ground

In this chapter, data for three GPR traverses collected as part of the RMC project were processed using the approach outlined in Chapter 4. A number of subsets of the FDHEM, TEM and GPR surveys were presented together, compared, and interpreted. The ground-based TEM appeared to have better resolution than the FDHEM and while both are similar there were differences in the results that appear to be more than just detail. Consistent with the conclusions in Chapter 2, the FDHEM was able to penetrate deeper than either of the two ground-based systems in this conductive environment. Over conductive parts of the traverses the FDHEM was limited to depths of approximately 25 m, while the TEM was limited to approximately 8 m. No systematic evaluation of the GPR data was made here. The GPR processing plotted results to between approximately 7 and 12-m depth.

Interpretation of the GPR was based on visual assessment of attenuation rates as observed on the depth sections. As attenuation rate is positively correlated with conductivity, areas with low attenuation rates have been interpreted as being relatively resistive, and likely to be characterised by low-salinity groundwater and low-clay content, and areas with high attenuation rates as being relatively conductive, with higher salinity groundwater and potentially more clay. Note that the inverted TEM conductivities observed on these lines range from approximately 25 mS/m (40 ohm-m) to greater than 2000 mS/m (<0.5 ohm-m). When areas are characterised as resistive or conductive, this conductivity range should be kept in mind.

The thickness of the unattenuated surface layer in the GPR correlated well with the resistive surface layer seen in much of the TEM. In the TEM this was observed when the section was essentially two-layer, where the resistive surface layer was interpreted to be the dry surface layer, above the capillary fringe, and the second, conductive layer started near the top of the moist, saline capillary fringe, grading with depth into the saline groundwater. Over the parts of the floodplain where the groundwater was fresher, the conductivity contrast between the surface

layer and the next layer was not sufficient for the top of the capillary fringe to be consistently resolvable by the TEM. In these areas the GPR continued to highlight a change in attenuation rate between the surface layer and the next layer. This was interpreted to be the depth to the top of the capillary fringe in these areas, where the TEM was not able to resolve this contrast.

6.2 Overall

A significant outcome of this research has arisen from examination of the connection between conductive and displacement currents. Most EM geophysicists tend to work largely at one end or the other of the EM frequency spectrum. At the low-frequency end of the spectrum (typically less than 100 kHz), conduction currents dominate response, and the use of quasi-static assumptions to simplify equations is appropriate. Conversely, at the high-frequency end of the spectrum (typically greater than 50 MHz), displacement currents dominate response, and the use of low-loss assumptions to simplify equations is appropriate.

The mathematics, as set out in Maxwell's Equations, and developments in EM geophysics since, have tended to allow the separation of these two worlds, as the mathematics and the physical reality of how energy travels in these realms are different. However, conductive currents exist under all conditions, but are so small under fully low-loss conditions that they are regarded as having negligible contribution. Similarly, displacement currents exist under all conditions, and again, are so small under fully quasi-static conditions that they too effectively vanish. In the transition band both exist, but both have influence and their influence varies, depending on how close to the quasi-static or low-loss ends of the transition band data are being collected.

As both the conductivity and dielectric permittivity of a material are related to the propagation of an electric field in that material, it might appear that these properties should be linked. Nevertheless, they are not obviously tied together, as the mechanisms of energy transfer are not similar. Conductive currents involve the change in location of a charge under the influence of an electric field, like the motion of an electron along a copper wire or a charged ion in a fluid, in both cases when an electric field is introduced. Dielectric permittivity represents much smaller charge movements, involving charge polarisation under an electric field, like a charged ion in a fluid-filled pore, where the motion of the ion is limited physically by the pore walls. Nevertheless, because they are both related to electricity and electrical fields we intuitively think of them together and know that they should be related. Interestingly, water is one factor that links these two conduction mechanisms. The key aspect is that water is a polar molecule, with its chemical geometry leaving one end of the water molecule positively charged, and the other

negatively charged. At low frequencies, this polarization allows water to act as a strong solvent, freeing ions from their non-reactive, solid state, so that they become charge carriers for conductivity currents, in water-filled pore space (Olhoeft, 1985; Annan, 2005a; Santamarina et al., 2005). That the water molecule is polar makes it the primary carrier for displacement currents at GPR frequencies as well. Most dry substances have relative dielectric permittivities that range from 1 to 10, while the relative dielectric permittivity of water is approximately 80 across the GPR frequency band. The presence of even a small amount of water in the pore space of a dry rock significantly increases the relative dielectric permittivity of that material (Olhoeft, 1985; Annan, 2005a).

That water acts as the principal mechanism for electrical conduction in the near surface, and that, in the study area, electrical conductivity is variable by two orders of magnitude, make it less surprising that the results of the field study shown in Chapter 5 informed more about water location and its salinity than about local geology and textural composition of the near surface. In Chapter 5, interpretation is made about relative clay content in the top 2 to 5 m, but based on indirect evidence, and, again, based on the behaviour of water in that zone. Variations in clay content in the top two or three metres appear to affect the height to which capillary action allows water to rise to above the watertable, defining the depth to the capillary fringe (Cresswell and Shand, 2009). Where the capillary fringe is thin and close to the regionally logged watertable the near surface is likely to be dominated by sand with little clay in the matrix. Where this zone is thick, the near surface is likely to have a higher clay content.

Comparisons of the available geological logs with interpretations from GPR and EMI observations at the bore locations show little correlation between shallow logged geology and geophysical response. It is surmised that the lithologically-based EM response is more subtle than the responses expected from the highly variable, conductive properties of the shallow groundwater. Similarly, there does not appear to be any change in the geophysical response that correlates with the depth to the actual water table. Here it is surmised that the EM response begins at a depth at which capillary action has lifted enough water above the water table for there to be a response, and that the electrical response does not measurably change with increased water saturation, as the signal progresses to the watertable.

Five techniques have been evaluated in this thesis for their ability to provide information about the hydrogeology of the Murray River and adjacent floodplains in the near surface. These may be separated into two groups. The first group was comprised of the in-stream techniques, which were assessed through a comparison of data acquired along a common stretch the Murray River. They were an in-stream TEM system, an in-stream DC resistivity system, and a high-

resolution FDHEM system (not strictly an in-stream technique, but able to provide information about the river setting). The second group was made up of techniques that could acquire information over the floodplains adjacent to the Murray River. These included a towed TEM system, a low-frequency GPR system, and the same high-resolution FDHEM system. As with the in-stream techniques, results from these different techniques were compared.

At the start of this thesis a number of aims and questions were presented as the basis for evaluating near-surface geophysical techniques, and their ability to provide information about the river and its floodplains. A number of questions were asked, including: 1) Is the data processing and interpretation consistent, such that the observed response can be correlated to their true locations?; 2) Do the highly conductive conditions under much of the Murray River and its associated floodplains mask the information that workers are interested in?; 3) What is the resolution of the data acquired (lateral and vertical)?; 4) Is the technique employed able to inform us about surface-water – groundwater interactions?; 5) Is the technique employed able to show us where small fresh water lenses occur, in this frequently saline environment?; and 6) Are we able to compare data sets over time to see changes? Some of the main conclusions related to these questions are summarised here.

To objectively answer questions 1, 2 and 3 it would be necessary to design a field test over conductive ground, where the locations of a number of objects, at various depths, were known. This is not practical, and was not done here. Instead, several technologies were used to acquire data over common pieces of river or ground, where shallow lithology and depth to groundwater was reasonably well understood from limited borehole information. The processed results from each survey were then compared. One of the main conclusions of this thesis was that the results from all of the techniques examined would be interpreted similarly over their test areas, with the observed differences attributable to investigation depths and resolution. As implied in question 1, careful attention needs to be given to data processing. This is particularly important for the GPR data, as the conductive floodplain environment is not well suited to wave-propagation based techniques such as GPR. An alternative processing approach presented here represents an improvement over previous methods, producing results that compare well with the coincident EMI data sets. However, these data comparisons also suggest that any of the other techniques evaluated here would provide the same information as the GPR, and are not dependent on other data sets for processing. Nevertheless, the GPR appears to be able to provide information about the depth to the top of the capillary fringe that EMI techniques appear not to provide as consistently.

Questions 4 and 5 relate directly to the hydrogeological information that can be derived from each geophysical data set. For these questions it is important to remember that, in this conductive setting, the conductivity variation of the water in the subsurface has the largest effect on the observed conductivity response, with little contribution from lithological variation. With this in mind, an examination of in-river techniques for the lower Murray River suggests that the correlation between conductive zones in the zone immediately under the river with gaining stretches, and resistive zones with losing stretches, informs us about surface-water – groundwater process issues raised in questions 4 and 5. In considering the various ground-based techniques from this perspective, it is apparent that they too can be used to identify localised fresh groundwater zones in the near surface. As flush zones are created by an interaction between surface-water and groundwater, these techniques are able to assist in the interpretation of these processes.

While question 6 is not explicitly dealt with in this research, it is nevertheless an important criterion for a system used to collect data in this environment. While there is a great deal of work being done to characterise, locate and understand how salt moves in these landscapes and is concentrated under the river and its associated floodplains, there are at least as many researchers and engineers involved in salinity remediation (e.g. Forward, 2004). The ability to measure changes in the shallow sediments under the river and floodplain has the potential to be an important capability.

6.3 Further research

In this section further research opportunities arising from this research are presented, in approximately chapter order.

- One of the limits noted when interpreting the FDHEM data collected over the Murray River (Chapter 2) is that it is not possible to measure the depth of the river during the survey from an airborne platform. It would be useful to be able to measure water depth from the plane while collecting AEM data. Wozencraft and Lilycrop (2002) report on a LIDAR-based system that measures water depth from an airborne platform in relatively clear water. They report that the system's depth limit is 2 to 3 times the visible depth limit in the water, and therefore is limited by water turbidity. As the Murray River is turbid and visibility into the water is limited, water depths measured with this system may be less than 3 m. While initially intriguing, this does not appear to be a viable research path. Vrbancich et al. (2000) outline a method using AEM data to estimate the depth to the bottom of Sydney Harbour. This method may be of limited usefulness on the Murray River as the footprint of the AEM bird is likely to be larger

than the river width in many locations. Also, as noted in Chapter 2, in the freshwater environment of the river, the contrast between the river bottom and river is not always enough for an EMI system to be able to resolve the change. Nevertheless, this method may be worthy of further investigation.

- Further work is needed to investigate the discrepancies between the GPR-derived conductivities and the TEM-derived conductivities.
- Dispersion was mentioned in Chapter 3 as a complicating factor in the evaluation of GPR data. Dispersion is likely to have a large effect on the shape of the 25 MHz GPR waveform as it travels through the earth. These data may benefit by a study which attempts to deconvolve the waveform from the data and then, to possibly model how this particular waveform would change with distance from source and changing ground conditions. The starting point for this is to know, and/or to be able to record, the actual waveform from any GPR system.
- Dispersion effects are not only significant for GPR data, but may be significant for EMI data as well. Under most conditions the low-frequency conductivity may not be much different from the 1000 Hz conductivity. EMI acquisition frequencies are approaching 500 kHz, and are likely to go higher. How different is the 500+ kHz conductivity from the low-frequency limit conductivity? Cole-Cole (1941), Knight and Nur (1987), and Jonscher (1992) for dielectrics and Pelton et al. (1978) for conductivity suggest similar relationships for how properties change with frequency. The research opportunity is to determine whether these properties change enough with frequency that some relatively simple rules need to be established and incorporated when processing and inverting these data.
- Most GPR systems, including the one used for this survey, are limited as they use a single transmitting antenna, with a single receiving antenna at a fixed offset distance. Having a number of receiving antennae at other offsets would allow for more sophisticated processing of these data, while still maintaining the advantage of nearly continuous data acquisition.
- Interpretation of the processed GPR data was based on visual characterisation of attenuation rates as observed in the processed sections. If attenuation rates were properly quantified and plotted on sections, would the results make it easier to more objectively identify areas with relatively higher or lower attenuation rates and compare directly to conductivity?
- Attribute analysis has the potential to add value to GPR data collected in these highly conductive environments. Complex trace analysis is used in seismic and GPR analysis to aid in the interpretation of subtle features in the data sets that may not be otherwise visible when

normally processed (Taner et al., 1979; White, 1991; Barnes, 2007). A number of the simpler attributes are worth evaluating. These include instantaneous amplitude (also known as amplitude envelope or trace envelope), instantaneous phase, cosine phase and instantaneous frequency. For example, the amplitude envelope would highlight the reflection strength of a GPR signal (Barnes, 2007) which might allow the analyst to more easily pick out zones of particularly high or low reflection strength, as well as highlight boundaries between these zones.

- Relative magnetic permeability is usually set to 1 (Reynolds, 1997; Lazaro-Mancilla and Gomez-Trevino, 2000), on the assumption that the magnetic susceptibility is generally low. For the sedimentary environments examined in this thesis this assumption is most likely reasonable. Olhoeft (1998) and Lazaro-Mancilla et al. (2000) examine EM behaviour when magnetic permeability is allowed to vary. Neither offers a mechanism for recognition of magnetic permeability effects in data. How do we recognise when magnetic permeability becomes important in our data, and what are the effects?

APPENDIX A: DISPERSION REVISITED

The subject of dispersion was outlined briefly in Chapter 3, but is expanded more fully in this appendix. There are a number of papers that discuss dispersion. For example, Fuller and Ward (1970) review results of various dispersion studies, and provide a theoretical framework for discussion. Giroux and Chouteau (2010) derive the attenuation and phase terms from the full solution of the wavenumber equation, based on the method of Fuller and Ward. Olhoeft (1979a) and Annan (1996) provide further useful insights into dispersion, specifically applied to high-frequency measurements like GPR, and laboratory determination of both conductivity and dielectric permittivity.

This appendix is divided into three parts. In the first part, the theoretical behaviour of dispersion is examined, and a version of the equation for the full wavenumber solution is derived where dielectric permittivity and conductivity vary with frequency, and have an out-of-phase component. In the second part, attempts by Debye (1929), Cole and Cole (1941), and Pelton et al. (1978) to characterise variation in dielectric permittivity and conductivity by frequency are reviewed. In the final section, results from four previous studies that measured dielectric permittivity over a range of frequencies are plotted together for comparison.

In the following sections, when conditions are stated as being low-loss, it will be assumed that the frequency is greater than 50 MHz. For quasi-static conditions it will be assumed that frequency is less than 100 kHz.

Complex behaviour of the wavenumber

It is interesting to examine solutions for the full wavenumber equation (Equation 3.2) when dielectric permittivity and conductivity are allowed to vary with frequency and are, therefore, complex. To do this we re-state the expression for magnetic permeability, dielectric permittivity and conductivity as complex functions (Olhoeft, 1979a):

$$\mu(\omega) = \mu'(\omega) - i\mu''(\omega) \quad \text{(A.1)}$$

$$\epsilon(\omega) = \epsilon'(\omega) - i\epsilon''(\omega) \quad \text{(A.2)}$$

$$\sigma(\omega) = \sigma'(\omega) + i\sigma''(\omega) \quad \text{(A.3)}$$

where μ is magnetic permeability (H/m), ε is dielectric permittivity (F/m), and σ is electrical conductivity (S/m). The ‘ terms are the real components and the “ terms are the imaginary. As noted earlier, we assume that $\mu = \mu_0$, i.e. that the relative magnetic permeability is

approximately 1, and does not change with frequency. This is not necessarily a reasonable assumption under all conditions (Olhoeft, 1998; Lazaro-Mancilla and Gomez-Trevino, 2000).

Fuller and Ward (1970) derive terms for "effective" dielectric permittivity and "effective" conductivity as functions of frequency, by substituting A.2 and A.3 into Maxwell's Equations, in the frequency domain, and then separating the real and the imaginary terms. All of the real terms are in-phase and associated with effective conduction currents, while the imaginary terms are out-of-phase and associated with effective displacement currents. These are given by

$$\sigma_e(\omega) = \sigma'(\omega) + \omega\varepsilon^{"}(\omega) \quad \text{(A.4)}$$

and,

$$\varepsilon_e(\omega) = \varepsilon'(\omega) + \frac{\sigma"(\omega)}{\omega} \quad \text{(A.5)}$$

where the subscript "e" indicates that the parameter is "effective".

Fuller and Ward (1970) then state that these effective terms are the measured lab or field parameters, and that it is generally not possible to completely separate the true conduction or permittivity term from the effective. They then state that under quasi-static conditions, conduction is the main current carrying mechanism, so displacement currents → 0, and:

$$\sigma_e(\omega) \cong \sigma'(\omega) \quad \text{(A.6)}$$

Under quasi-static conditions, by slightly rearranging the effective permittivity term we get:

$$\sigma"(\omega) \cong \omega * \varepsilon_e(\omega) \quad \text{(A.7)}$$

This approximation suggests that phase response at low frequencies acts like a displacement current.

Under low-loss conditions, displacement is the main conduction mechanism, and conductive currents → 0, thus:

$$\sigma_e(\omega) \cong \omega\varepsilon^{"}(\omega) \quad \text{(A.8)}$$

and,

$$\varepsilon_e(\omega) \cong \varepsilon'(\omega). \quad \text{(A.9)}$$

Equations A.8 and A.9, and the low-loss assumptions provide the basis under which a number of high-frequency laboratory and field devices are able to estimate both dielectric permittivity and conductivity (Campbell, 1990; Wensink, 1993; Seyfried and Murdock, 2004).

To derive a general solution to the wavenumber equation where dielectric permittivity and conductivity are complex, we restate the wavenumber equation (Equation 3.2), inserting the complex expressions for dielectric permittivity and conductivity given in Equations A.2 and A.3:

$$k^2 = \mu\omega(\omega(\epsilon' - i\varepsilon") - i(\sigma' + i\sigma")).$$

Rearranging we get:

$$k^2 = \mu\omega\left(1 - i\frac{\sigma^{'}+\omega\varepsilon^{"}}{\sigma^{"}+\omega\varepsilon^{'}}\right) = \beta - i\alpha \quad \text{(A.10)}$$

where α and β are the attenuation and phase terms (von Hippel, 1954) that need to be solved for, as defined in Chapter 3.

The loss tangent is then defined as (Fuller and Ward, 1970; Olhoeft, 1979a):

$$\tan\theta = \frac{\sigma^{'}+\omega\varepsilon^{"}}{\sigma^{"}+\omega\varepsilon^{'}} \quad \text{(A.11)}$$

Solving Equation A.10 for α and β yields:

$$\alpha = \sqrt{\frac{\omega\mu(\sigma^{"}+\omega\varepsilon\prime)}{2}\sqrt{(1+(\tan\ \theta)^2)} - 1} \quad \text{(A.12)}$$

$$\beta = \sqrt{\frac{\omega\mu(\sigma^{"}+\omega\varepsilon^{'})}{2}\sqrt{(1+(\tan\ \theta)^2)} + 1} \quad \text{(A.13)}$$

As shown in Chapter 3, phase velocity is then defined by $v = \frac{\omega}{\beta}$, and skin depth by $\delta = \frac{1}{\alpha}$.

It is worth noting that at high frequencies (i.e. under low-loss conditions, where it is assumed that σ'' becomes negligible) these equations revert to the form given by von Hippel (1954) for a transversal EM wave. Similarly, when both ε'' and σ'' are very small (i.e. neither the dielectric permittivity nor conductivity vary with frequency), Equation A.11 reduces to Equation 3.3, Equation A.12 reduces to Equation 3.7 and Equation A.13 reduces to Equation 3.8.

As an aside, an additional set of derivations provided by an anonymous reviewer of an earlier version of Chapter 3 are included here. These derivations are reproduced below as the final result is a compact variation on the wavenumber equation where any of the terms may be complex. Note that in this derivation $= \frac{1}{\sqrt{\mu\varepsilon}}$, i.e. c is the low-loss phase velocity (Equation 3.4), and c_0 is the speed of light in a vacuum.

For any dimensional propagation and diffusion, the wavenumber is written as the following square root, as presented as Equation 3.2.

$$k = \sqrt{\omega^2\varepsilon\mu - i\omega\mu\sigma} \quad \text{(A.14)}$$

Now if we want to prepare for high-frequency approximation we can write:

$$k = \frac{\omega}{c}\sqrt{1 - i\frac{\sigma}{\omega\varepsilon}} = \frac{\omega}{c}\left(1 - i\frac{\sigma}{2\omega\varepsilon} + O\left(\frac{\sigma^2}{\omega^2\varepsilon^2}\right)\right) \approx \frac{\omega}{c} - i\frac{1}{2}\sigma Z \quad \text{(A.15)}$$

where the second term is the zeroth and first order terms in a Taylor series expansion for $\sigma \ll \omega\varepsilon$, (low-loss conditions) and the result is the well-known approximation for wave propagation in weakly attenuating media, which is the type of media where GPR works best.

Now if we want to prepare for the low-frequency approximation, we can write

$$k = \sqrt{-i\omega\sigma\mu}\sqrt{1 + i\frac{\omega\varepsilon}{\sigma}} = \sqrt{-i\omega\sigma\mu}\left(1 + i\frac{\omega\varepsilon}{2\sigma} + O\left(\frac{\sigma^2}{\omega^2\varepsilon^2}\right)\right) \approx \sqrt{-i\omega\sigma\mu} \quad \text{(A.16)}$$

which is the low-frequency approximation valid when $\omega\varepsilon \ll \sigma$ (quasi-static conditions). Notice that here we need only the zero order term of the Taylor expansion, because the leading term is a complex square root that has much bigger real and imaginary parts than we would add by including the first order term. If we keep the wave propagation term outside we can still write a general expression given by

$$k = \frac{\omega}{c}\sqrt{1 - i\frac{\sigma}{\omega\varepsilon}} = \frac{\omega}{c}\left[\sqrt{\frac{1}{2}\sqrt{1 + \left(\frac{\sigma}{\omega\varepsilon}\right)^2} + \frac{1}{2}} - i\sqrt{\frac{1}{2}\sqrt{1 + \left(\frac{\sigma}{\omega\varepsilon}\right)^2} - \frac{1}{2}}\right] \quad \text{(A.17)}$$

Whether or not the medium parameters are a function of frequency is irrelevant, because the general description using a complex square root is still valid, and one can always take frequency and the free space velocity out resulting in

$$k = \frac{\omega}{c_0}\sqrt{\varepsilon_r\mu_r - i\frac{\sigma}{\omega\varepsilon_0}} \quad \text{(A.18)}$$

where now all parameters inside the square root can still be complex (implying frequency dependence). In the case of general frequency dependence, it is of course mathematically convenient to make either electric permittivity, or conductivity, complex, not both. All possible frequency dependent damping and relaxation phenomena can be captured in one of the two electric parameters. Many people take permittivity and keep DC conductivity as the frequency independent parameter.

Theory: Dielectric and conductivity variation with frequency

Debye (1929) describes mathematically the dielectric variation of a number of fluids and gases with frequency. Cole and Cole (1941) extend the Debye definition for a larger range of materials. Others have extended these equations further, but most of these are variations of these two models. Both Debye and Cole-Cole may be used to fit many dielectric spectra, at least qualitatively and are referred to frequently in the literature (e.g. Hoekstra and Delaney, 1974; Knight and Nur, 1987; Wensink, 1993). Equation A.19 is the Cole and Cole (1941) equation for variation of dielectric permittivity with frequency.

$$\varepsilon(\omega) = \varepsilon_\infty + \frac{\varepsilon_s - \varepsilon_\infty}{1 + (i\omega\tau)^{1-\alpha}} \quad \text{(A.19)}$$

where ε_∞ is the high frequency limit of the dielectric permittivity of a given material; ε_s is the low frequency limit of the dielectric permittivity for the same material; τ is the relaxation time

for that material, i.e. the reciprocal of the relaxation frequency; and α is the distribution parameter constant (between 0 and 1). Equation A.19 reduces to the Debye relationship when α = 0. When α = 1, the imaginary term disappears, and the dielectric permittivity no longer varies with frequency (Olhoeft, 1979a). As an example, Hoekstra and Delaney (1974) were able to reasonably match the dispersion curves for dielectric permittivity of a number of soils for frequencies between 100 MHz and 26 GHz by combining two closely spaced Cole-Cole type dispersion models.

Approaches such as the Debye and Cole-Cole models allow researchers to visualise how various electrical parameters change with frequency. Since it is necessary to have good estimates of ε_∞, ε_s, τ and α to accurately predict $\varepsilon(\omega)$, these equations are better used to characterise laboratory behaviour of dielectrics or, alternatively, to show approximately how the dielectric permittivity varies with frequency, than to predict how a particular rock or soil behaves in the field. In a field situation, we are likely to only have knowledge of dielectric permittivity at a single frequency or at most a small range of frequencies, and are not able to extrapolate to higher or lower frequency with sufficient accuracy.

Pelton et al. (1978) suggested a similar relationship to the Debye/Cole-Cole relationships to describe how conductivity changes with frequency (frequently called the Cole-Cole model). This relationship can be used to match a large number of responses to various lab and field situations. Again, it is best suited to characterising material behaviour for which conductivity data have been collected over a wide frequency range than to predict conductivity behaviour in a field situation from data collected at a single frequency or at most over a small frequency range.

Over the EM frequency range a number of physical and chemical mechanisms explain the variation of dielectric permittivity with frequency. Von Hippel (1954), Olhoeft (1979a; 1985), Annan (1996), and Knight and Nur (1987) all go into these in some detail, and provide a large number of references. Briefly, there are four polarisation mechanisms that operate over the geophysical frequency band. Electronic polarisation occurs at relatively high frequencies and involves the alignment of charge due to the offset of electrons around a nucleus under the influence of an electric field. Atomic/ionic polarisation occurs at slightly lower frequencies and involves polarisation of atoms which do not share electrons equally. Dipolar polarisation occurs at lower frequencies than electronic polarisation and involves the alignment of molecules, like water, with asymmetrical charge distribution, under the influence of an electric field. The lowest frequency polarisation that we are interested in is Maxwell-Wagner polarisation (Maxwell, 1891; Wagner, 1914), involving the alignment of charges in heterogeneous mixtures of substances with electrically varying properties (Olhoeft, 1979a; Knight and Nur, 1987).

Figure A.1 (modified from Poley et al., 1978) shows schematically the variation of real and imaginary dielectric permittivity with frequency, identifying the various mechanisms that may contribute to the dielectric permittivity in a given frequency range. This figure was prepared using the resonant equation from von Hippel (1954) to approximate the behaviour of the electronic and the atomic polarisations, and the Debye equation (Debye, 1929) to approximate the behaviour of the dipolar and Maxwell-Wagner polarisations. In general, the effects that contribute to the dielectric conductivity are cumulative, with the dielectric permittivity contribution from higher frequency mechanisms adding to those at lower frequencies (von Hippel, 1954). As a result, when the dielectric permittivity is measured at a given frequency, it will not be lower than any value measured at a higher frequency.

Overview of four studies that measure dielectric variation with frequency

In this section the results from four studies that measure dielectric permittivity behaviour over various parts of the EM spectrum are plotted together. Beginning in the early 20th Century, a number of researchers have examined variation in dielectric permittivity and conductivity with frequency (see, for example: Smith-Rose (1933), Hoekstra and Delaney (1974), Olhoeft (1979b), and Knight and Nur (1987)). Some of these studies, while interesting from a research perspective were performed at very high frequencies, and are, therefore, of little practical use to applied researchers (e.g., Hoekstra and Delaney (1974) determined the dielectric permittivity for various soils at frequencies from 100 MHz to 26 GHz). Others test many substances, some of which are not of general interest to near-surface researchers (e.g., dielectric properties of black obsidian at 1 MHz (Olhoeft, 1979b)). This section reviews four studies that measure dielectric permittivity over a range of frequencies that are likely to be of interest to applied researchers of near-surface properties. Figure A.2 summarises the results from four of these studies (Olhoeft, 1979b; 1986; Knight and Nur, 1987; Wensink, 1993).

In Figure A.2, the entries ending with “o” are from Olhoeft (1979b). Olhoeft (1979b) tabulated physical properties for a number of rocks and minerals that he and others analysed. These parameters include dry bulk-density, DC electrical conductivity, relative dielectric permittivity and loss tangent. Dielectric permittivity data were collected at 1 kHz, 10 kHz, 100 kHz and 1 MHz. Results for seven materials found in the near surface are presented here: limestone (results for seven samples were presented in Olhoeft (1979b) and averaged for this figure), sandstone (results for four samples were presented and averaged), shale (results for seven samples were presented and averaged), kaolinite (results for three samples were presented and

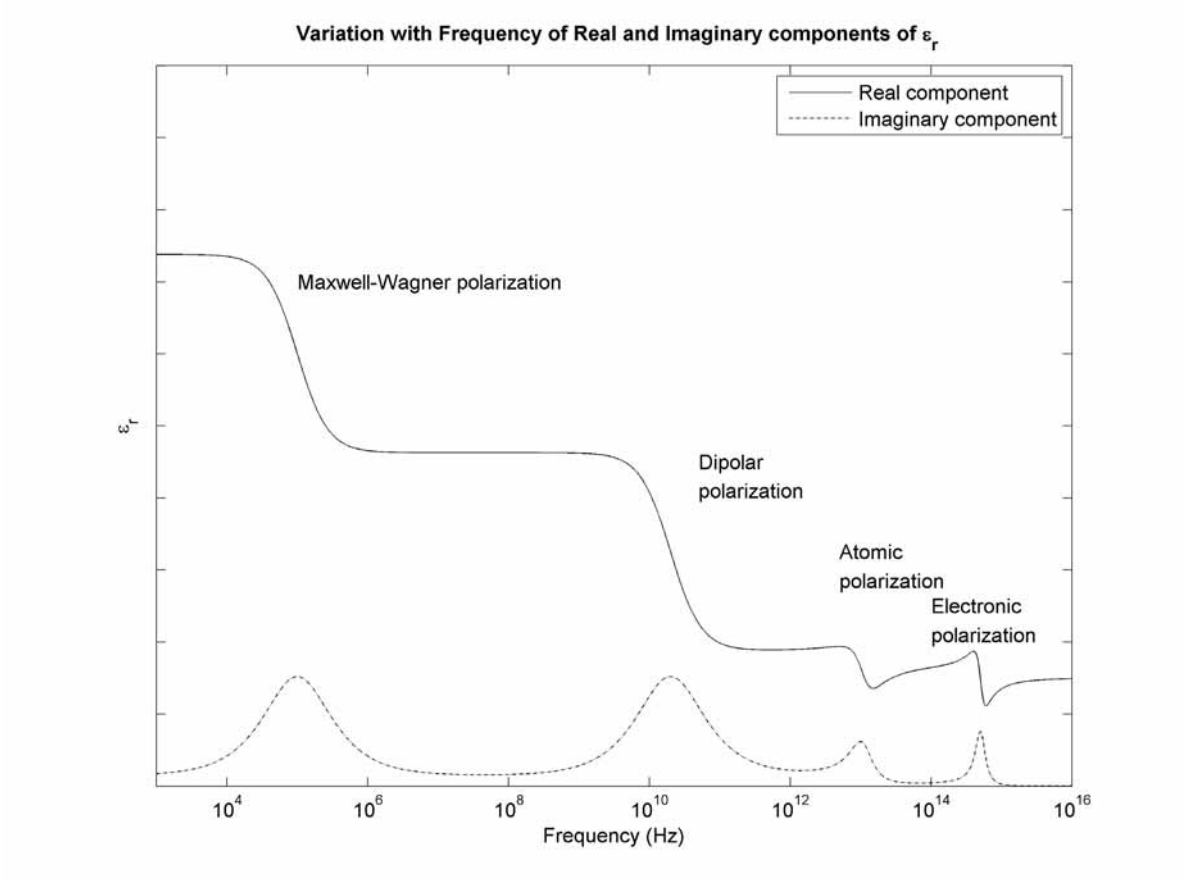

Figure A.1: Schematic view of the variation of permittivity from 10^3 to 10^{16} Hz. Real and imaginary components are both shown. The four main polarisation mechanisms are shown at their approximate location in frequency (after Poley et al., 1978).

averaged), and montmorillonite (results for three samples were presented and averaged). The averaged dielectric permittivity results for each material are plotted in Figure A.2. Note that the relative dielectric permittivity for one shale sample was much higher than for the rest, indicative of variability within shale samples.

Entries in Figure A.2 ending with "o2" are from Olhoeft (1986). In this study, Olhoeft measured the variation in relative dielectric permittivity and conductivity for nine synthetic samples composed of different blends of distilled water, pure silica sand and commercially available, standard clay. These data were collected from approximately 5.6 MHz to nearly 1 GHz and are displayed here from 5.6 MHz to approximately 320 MHz. The results are hand scaled from the published, graphed results, and are therefore approximate. Results for two of samples are shown. The "wet clay" sample, labelled k_3_wetclay_o2, is made up of 79.5% sand, 4.9% clay and 15.6% water, and is shown in Figure 3 of Olhoeft (1986). The DC conductivity for this sample is 63.7 mS/m (15.7 ohm-m). The "wet sand" sample, labelled k_5_wetsand_o2, is made

up of is 83.6% sand and 16.4% water, and is shown in Figure 5 of Olhoeft (1986). The DC conductivity for this sample is 3.7 mS/m (269 ohm-m).

Entries ending with "k", in Figure A.2, are from Knight and Nur (1987). In this study the variation in relative dielectric permittivity and conductivity with frequency was measured for eight sandstones. As with the Olhoeft (1986) study, these results were presented graphically, so the values presented here are approximate. Results for two of the samples are shown from 100 kHz to 3.2 MHz, chosen as they represent much of the range of data presented in that paper. Each sample was saturated to a S_w of 0.36. Sheriff (2002) defines S_w as the fraction of pore volume taken up by formation water. Sample CH61-79 is a tight-gas sandstone with low porosity and high clay content. Conductivities range from approximately 1.2×10^{-3} to 2.2×10^{-3} mS/m (8.3×10^{4} ohm-m to 4.6×10^{4} ohm-m). The St. Peter's (SP) sandstone sample is an orthoquartzite, with low clay content and moderate porosity. Conductivities range from approximately 2×10^{-3} to 4×10^{-3} mS/m (5×10^{5} ohm-m to 2.5×10^{5} ohm-m).

The line labelled k_calc is based on the power law expression given in Knight and Nur (1987): $k' = A\omega^{-\alpha}$. The value for the exponent is given in that paper for sample CH61-79, while *A* is arbitrarily set to 1000 to match the data.

Entries ending with "w" in Figure A.2, are from Wensink (1993). In this study Wensink (1993) measured the variation in dielectric permittivity and conductivity against both frequency (1 MHz to 3 GHz) and soil moisture (dry to 0.746 VWC) for 11 different clay soil samples. Wensink (1993) defines VWC as the relative volume of water in a given volume of sample. Only the results from 1 MHz to 1 GHz are shown in Figure A.2. The results in Wensink (1993) are presented graphically, so again, are approximate as shown here. The analyses for two samples (Samples 2 and 9) are shown here, which were estimated from Wensink (1993), Figures 3 and 5. These two samples were chosen because they included analyses for both wet and dry samples, and represent a large range of the data analysed. Conductivity for Sample 2 (dry) is stated to be less than 7 mS/m (>143 ohm-m) for frequencies less than 2 GHz. Conductivity for Sample 2 (wet - 0.338 VWC) range from less than 100 mS/m (>10 ohm-m) to greater than 300 mS/m (<3.3 ohm-m). Conductivity for Sample 9 (dry) is stated to be less than 5 mS/m (>200 ohm-m)). Conductivity for Sample 9 (wet - 0.370 VWC) range from less than 100 mS/m (>10 ohm-m) to greater than 700 mS/m (<1.4 ohm-m). These samples are labelled k_dryclay_2_w, k_wetclay_2_w, k_dryclay_9_w, and k_wetclay_9_w, respectively.

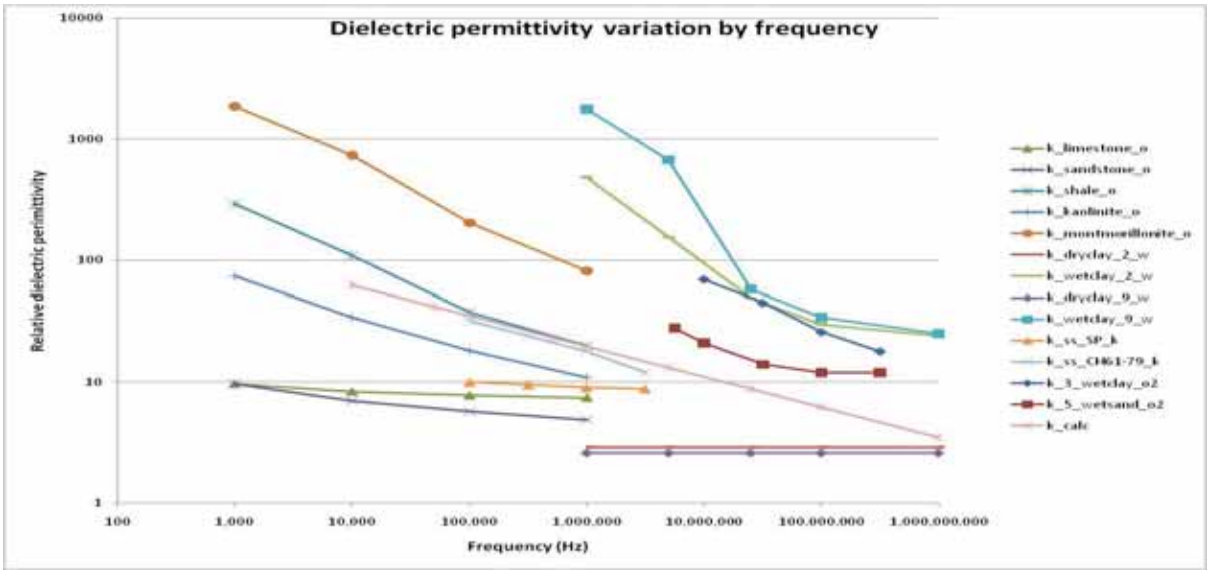

Figure A.2: Dielectric permittivity variation by frequency as measured by various researchers. In the legend, those ending with "o" are from Olhoeft (1979b), those ending with "w" are from Wensink (1993), those ending with "k" are from Knight and Nur (1987) and, those ending with "o2" are from Olhoeft (1986). k_calc is based on the power law expression given in Knight and Nur (1987) and the value for the exponent given in that paper for sample CH61-79.

Fuller and Ward (1970) present a review of three data sets of conductivity and dielectric permittivity, where frequency was varied from 1 Hz to 1 MHz. They divide response into two simple categories: "wet" samples and "dry" samples. They summarise the results for wet samples as: 1) conductivity does not vary greatly over the frequency range, typically less than one order of magnitude; 2) conductivities are generally greater than 100 mS/m (<10 ohm-m); 3) the dielectric constant is much more variable, and is inversely proportional to frequency over the lower half of this frequency range; 4) dielectric constant may be very high at low frequencies (potentially $>10^8$ below 1 Hz); and 5) at high frequencies dielectric permittivity generally is not greater than the value for water (approximately 80).

They summarise the results for dry samples as: 1) conductivity is variable, and is generally inversely proportional to frequency; 2) conductivities are generally less than 10^{-3} mS/m ($>10^6$ ohm-m); 3) dielectric permittivity does not vary greatly over this frequency range; and 4) relative dielectric permittivities are generally less than 10.

For dielectric permittivity, Fuller and Ward's (1970) conclusions about behaviour of wet and dry rocks is mostly consistent with the results summarised in Figure A.2

There are not many papers that present conductivity and phase response spectra below 1 MHz. Fuller and Ward (1970) review the results of four studies performed before 1970; the conclusions from that study are presented in the previous paragraph. Olhoeft (1985) presents results for a number of earth materials, most of which would be characterised as "wet". These results are generally consistent with the conclusions from Fuller and Ward (1970). For most of the materials tested for this paper, the conductivity does not vary greatly from 1Hz to 1 MHz. Olhoeft (1985) presents results from materials that are not consistent with these conclusions, but these samples contain graphite and sulphides, which he characterises as chemically reactive, i.e. most of the response is not related to water content.

Discussion

There are inconsistencies between data sets, as presented in Figure A.2. Some of these inconsistencies may be attributed to how the measurements were made, i.e. variability in samples, saturation and frequency bandwidth of measurement, but this does not always appear to be the case.

As noted above, two of the samples from Wensink (1993) are dry clays with conductivities less than 7 mS/m (>143 ohm-m) below 2 GHz. In Figure A.2 the dielectric response for both samples does not vary greatly with frequency, and is less than 3 over the frequency range 1 MHz to 1 GHz. The average conductivity for Olhoeft's (1979b) montmorillonite

is $3.4x10^{-4}$ mS/m ($3.34x10^{6}$ ohm-m), suggesting that this sample is a dry clay. The averaged dielectric permittivity for montmorillonite is given as 82 at 1 MHz, increasing to 1860 at 1 kHz (Figure A.2 – curve labelled k_montmorillonite_o) (Olhoeft, 1979b). The dielectric response for Olhoeft's (1979b) kaolinite is lower but similar. While the frequency ranges for the Wensink (1993) and the Olhoeft (1979b) studies are not the same, it appears unlikely that the montmorillonite curve is for a "dry clay", as the response from Wensink's (1993) dry clays and Olhoeft's (Olhoeft, 1979b) dry montmorillonite and kaolinite are much different and do not align. The dielectric behaviour of Olhoeft's (1979b) montmorillonite would be easier to associate with the response from the Olhoeft (1986) wet clay (labelled k_3_wetclay_o2) or the wet sand (labelled k_5_wetsand_o2). In fact, the response for the wet clay sample from Olhoeft (1986) (k_3_wetclay_o2), containing only 4.9% clay, is similar to the wet Wensink (1993) samples. These comparisons suggest that either pure, dry montmorillonite is far more polarisable than the dry clays tested by Wensink (1993), or, more likely, that the conductivity values provided by Olhoeft (1979b) for montmorillonite are for the dried samples, and that the permittivity measurements were made with at least some moisture in the samples. The dielectric permittivity values for wet clays at 1 MHz, provided by Wensink (1993) are among the highest noted in the literature. It is worth noting that montmorillonite is a member of the smectite family of clays, has a high cation exchange capacity (Schaetzl and Anderson, 2005; Eggleton, 2009), and is expected to be polarisable. Kaolinite has a lower cation exchange capacity than montmorillonite (Eggleton, 2009), which is consistent with its lesser response in Figure A.2.

Another more fundamental problem may arise from the likelihood that some of these data were not collected under low-loss conditions. If this is the case then the conductivities and permittivities provided for those samples are "effective" (Fuller and Ward, 1970) and are contaminated by information from the imaginary components of the other parameter (see Equations A.4 and A.5 – the effective dielectric permittivity includes an out-of-phase conductivity term and vice versa). To evaluate this, the loss tangents need to be examined. One of the main conclusions of Chapter 3 is that the loss tangent is a strong indicator of where in the EM frequency band a set of data has been collected. Using the 5% error margins adopted in that chapter, when the loss tangent is less than 0.7 the system is operating under low-loss conditions. Calculating the loss tangent is not straightforward for the data presented in Wensink (1993), as there is some confusion in the naming of parameters, and in how parameters were calculated. Examination of the data in Wensink (1993) suggests that the conductivities range from less than 20 mS/m (>50 ohm-m) at frequencies below approximately 10 MHz) to greater than 500 mS/m (<2 ohm-m) at approximately 3 GHz. Annan (2005a) gives a range of values for wet clays of

between 2 and 2000 mS/m (500 to 0.5 ohm-m). In Table A.1 the loss tangent has been calculated based on three values for conductivity to cover much of this range: 500 ms/m (2 ohm-m), 100 mS/m (10 ohm-m) and 20 mS/m (50 ohm-m). Permittivity values from Wensink (1993) are used as no other information is available, even though these may have been calculated using low-loss approximations. At 500 mS/m most of the data as quoted would not be low-loss and would therefore be incorrect, while at 20 mS/m, nearly all of the data would be low-loss and would be correct. These results are not conclusive, but certainly suggest that it is important to consider whether low-loss approximations are appropriate when performing such measurements.

Table A.1: Evaluation of loss tangent for Wensink (1993)

Frequency (MHz)	Resistivity (ohm-m)	Conductivity (mS/m)	Loss tangent
1	2	500	19
5	2	500	12
25	2	500	7.3
100	2	500	3.0
1000	2	500	0.37
1	10	100	3.7
5	10	100	2.3
25	10	100	1.5
100	10	100	0.60
1000	10	100	0.07
1	50	20	0.74
5	50	20	0.46
25	50	20	0.29
100	50	20	0.12
1000	50	20	0.01

When a similar analysis is performed on the wet clay observations from Olhoeft (1986), the loss tangent ranges from approximately 2.91 at 5.6 MHz to 0.23 at 316 MHZ. While the equations used to calculated dielectric permittivity are not given in Olhoeft (1986), this study may also be presenting dielectric permittivity data that, if based on the low-loss equations for dielectric permittivity, are likely to affected by the imaginary conductivity component.

It is worthwhile comparing the curves in Figure A.2 for the Knight and Nur (1987) sample CH61-79 with the calculated results based on the power law relationship given in that paper, using the exponent provided for that sample. The curve shown in Figure A.2 is calculated using the expression $k' = A\omega^{-\alpha}$, where k' is the real component of the relative dielectric permittivity, and A and α are constants that depend on the sample, and the level of saturation (Knight and

Nur, 1987). While Knight and Nur (1987) provide an α value for each sample tested, they do not do the same for A, and furthermore, do not indicate how such values were determined. For the k_calc curve shown in Figure A.2 α was set to 0.251 (as provided in Table 3 (Knight and Nur, 1987)) and A was set, by inspection, to 1000. Comparison with the curve labelled CH61-79 suggests that it may be possible to approximately estimate dielectric permittivity variation with frequency and then incorporate that information into inversions and other processing to evaluate its effect on data results.

Obviously, the review shown here is not large enough a sample to characterise rock types. Nevertheless, with information from other studies it may be possible to establish ranges of power law exponents by rock type, so that predictions of dielectric permittivity may be made, by rock type, over a range of frequencies.

REFERENCES

al Hagrey, S. A., and C. Muller, 2000, GPR study of pore water content and salinity in sand: Geophysical Prospecting, **48**, 63-85.

Allen, D. A., 2007, Electrical conductivity imaging of aquifers connected to watercourses - A thesis focused on the Murray Darling Basin, Australia: PhD thesis, University of Technology Sydney.

Allen, D. A., and N. P. Merrick, 2003, A floating electrode array for continuous geoelectrical imaging: ASEG 16th Geophysical Conference and Exhibition: ASEG, Extended Abstracts, accessed 23 June 2010; http://www.publish.csiro.au/paper/ASEG2003ab001.htm.

Allen, D. A., and N. Merrick, 2007, Robust 1D inversion of large towed geo-electric array datasets used for hydrogeological studies: Exploration Geophysics, **10**, no. 1, 50-59.

Amidu, S. A., and J. A. Dunbar, 2007, An evaluation of the electrical-resistivity method for water-reservoir salinity studies: Geophysics, **73**, no. 4, G39-G49.

Annan, A. P., 1996, Transmission dispersion and GPR: Journal of Environmental and Engineering Geophysics, **1**, no. 2, 125-136.

Annan, A. P., 2005a, Ground-penetrating radar, *in* D. Butler, ed., Near-Surface Geophysics, Volume 1: Concepts and Fundamentals: Society of Exploration Geophysicists, 71- 87.

Annan, A. P., 2005b, GPR methods for hydrogeological studies, *in* Y. Rubin and S. S. Hubbard, eds., Hydrogeophysics: Springer, 185-213.

Aquaterra, 2010, Mallee Groundwater Monitoring 2010, Mallee Catchment Management Authority, accessed 16 December 2010; http://www.malleecma.vic.gov.au/resources/reports/2010_mallee_gw_monitoringv-entire.pdf.

Auken, E., L. Pellerin, N. B. Christensen, and K. Sorensen, 2006, A survey of current trends in near-surface electrical and electromagnetic methods: Geophysics, **71**, no. 5, G249-G260, accessed 23 June 2010; http://link.aip.org/link/?GPY/71/G249/1.

Auken, E., A. V. Christiansen, B. H. Jackson, N. Foged, and K. I. Sørensen, 2005, Piecewise 1D laterally constrained inversion of resistivity data: Geophysical Prospecting, **53**, 497-506.

Barnes, A. E., 2007, A tutorial on complex seismic trace analysis: Geophysics, **72**, no. 6, W33-W43.

Barrett, B. E., G. Heinson, M. A. Hatch, and A. Telfer, 2005, River sediment salt-load detection using a water-borne transient electromagnetic system: Journal of Applied Geophysics, **58**, 29-44.

Barrett, B. E., T. Murray, R. Clark, and K. Matsuoka, 2008, Distribution and character of water in a surge-type glacier revealed by multifrequency and multipolarization ground-penetrating radar: Journal of Geophysical Research, **113**, no. F04011, 1-12.

Bastani, M., and L. B. Pedersen, 2001, Estimation of magnetotelluric transfer functions from radio transmitters: Geophysics, **66**, no. 4, 1038-1051.

Beamish, D., 2003, Airborne EM footprints: Geophysical Prospecting, **51**, no. 1, 49-60.

Beamish, D., 2004, Airborne EM skin depths: Geophysical Prospecting, **52**, no. 5, 439-449.

Blindow, N., 2009, Ground penetrating radar, *in* R. Kirsch, ed., Groundwater Geophysics: A Tool for Hydrogeology: Springer Verlag, 227-252.

Brodie, R., and M. Sambridge, 2006, A holistic approach to inversion of frequency-domain airborne EM data: Geophysics, **71**, no. 6, G301-G312.

Brosten, T. R., J. H. Bradford, J. P. McNamara, M. N. Gooseff, J. P. Zarnetske, W. B. Bowden, and M. E. Johnston, 2009, Multi-offset GPR methods for hyporheic zone investigations: Near Surface Geophysics, 247-257.

Brown, C. M., and A. E. Stephenson, 1991, Geology of the Murray Basin, southeastern Australia: Australian Government Publishing Service.

Butler, K. E., 2009, Trends in waterborne electrical and EM induction methods for high resolution sub-bottom imaging: Near Surface Geophysics, **7**, 241-246.

Cagniard, L., 1953, Basic theory of the magneto-telluric method of geophysical prospecting: Geophysics, **18**, no. 3, 605-635.

Campbell, J. E., 1990, Dielectric properties and influence of conductivity in soils at one to fifty megahertz: Soil Science Society of America Journal, **54**, 332-341.

Christiansen, A. V., and E. Auken, 2010, A global measure for depth of investigation in EM and DC modeling: ASEG 21st Geophysical Conference and Exhibition: ASEG, Extended Abstracts, accessed 9 March 2011; http://www.publish.csiro.au/nid/267/paper/ASEG2010ab266.htm.

Christiansen, A. V., E. Auken, and K. Sorensen, 2009, The transient electromagnetic method, *in* R. Kirsch, ed., Groundwater Geophysics: A Tool for Hydrogeology: Springer Verlag, 179-226.

Clarke, J. D. A., D. Gibson, and H. Apps, 2010, The use of LiDAR in applied interpretive landform mapping for natural resource management, Murray River alluvial plain, Australia: International Journal of Remote Sensing, **31**, no. 23, 6275-6296.

Cole, K. S., and R. H. Cole, 1941, Dispersion and absorption in dielectrics: I. Alternating current characteristics: Journal of Chemical Physics, **9**, 341-351.

Cresswell, R. G., and P. Shand, 2009, Regolith and Water, *in* K. M. Scott and C. F. Pain, eds., Regolith Science: CSIRO Publishing, 251-280.

Davis, J. L., and A. P. Annan, 1989, Ground-penetrating radar for high-resolution mapping of soil and rock stratigraphy: Geophysical Prospecting, **37**, 531-551.

Debye, P., 1929, Polar Molecules: Chemical Catalog Company.

Department of Sustainability and Environment, 2010, Victorian Water Resources Data Warehouse, http://www.vicwaterdata.net/vicwaterdata/data_warehouse_content.aspx?option=4, accessed 23 June 2010.

Eggleton, R. A., 2009, Regolith mineralogy, *in* K. M. Scott and C. F. Pain, eds., Regolith Science: CSIRO Publishing, 45-72.

Elmore, A. J., J. F. Mustard, S. J. Manning, and D. B. Lobell, 2000, Quantifying vegetation change in semiarid environments: Precision and accuracy of spectral mixture analysis

and the normalized difference vegetation index: Remote Sensing of Environment, **73**, 87-102.

Ezzy, T. R., A. J. O'Rourke, G. J. Huftile, and M. E. Cox, 2003, Applying ground penetrating radar (GPR) to improve hydrogeological understanding and groundwater modelling within a coastal plain setting: in Tecnologia de la Intrusion de Agua de Mar en Acuifreos Costeros: Paises Mediterraneos, edited, IGME.

Fetter, C. W., 2001, Applied Hydrogeology: Prentice Hall, Inc.

Fitzpatrick, A., T. J. Munday, V. Berens, and K. Cahill, 2007a, An examination of frequency domain and time domain HEM Systems for defining spatial processes of salinisation across ecologically important floodplain areas: lower Murray River, South Australia: Symposium on the Application of Geophysics to Engineering and Environmental Problems 2007: The Environmental and Engineering Geophysics Society, Extended Abstracts, 1179-1186.

Fitzpatrick, A., T. Munday, V. Berens, M. Hatch, and A. Telfer, 2007b, Mapping salt-loads of the Murray River, Australia, using airborne and in-river electromagnetic methods: Symposium on the Application of Geophysics to Engineering and Environmental Problems 2007: The Environmental and Engineering Geophysics Society, Extended Abstracts, 410-417.

Forward, P. D., 2004, South Australia's River Murray salt interception schemes: History, performance and future directions: Engineering Salinity Solutions: 1st National Engineering Salinity Conference 2004: Institute of Engineers, Australia, 325-330.

Franke, J., and V. Utsi, 2009, Advances in long-range GPR systems and their applications to mineral exploration, geotechnical and static correction problems: First Break, **27**, 85-93.

Fullagar, P. K., D. W. Livelybrooks, P. Zhang, A. J. Calvert, and Y. Wu, 2000, Radio tomography and borehole radar delineation of the McConnell nickel sulfide deposit, Sudbury, Ontario, Canada: Geophysics, **65**, no. 6, 1920-1930.

Fuller, B. D., and S. H. Ward, 1970, Linear system description of the electrical parameters of rocks: IEEE Transactions on Geoscience Electronics, **GE-8**, no. 1, 7-18.

Giroux, B., and M. Chouteau, 2010, Quantitative analysis of water-content estimation errors using ground-penetrating radar data and a low-loss approximation: Geophysics, **75**, no. 4, WA241-WA249.

Goldman, M., H. Gvirtzman, and S. Hurwitz, 2004, Mapping saline groundwater beneath the Sea of Galilee and its vicinity using time domain electromagnetic (TDEM) geophysical technique: Israeli Journal of Earth Sciences, **53**, 287-297.

Goldman, M., H. Hurwitz, H. Gvirtzman, B. Rabinovich, and Y. Rotstein, 1995, Application of the marine time domain electromagnetic method in lakes: the Sea of Galilee, Israel: European Journal of Environmental and Engineering Geophysics, **1**, 125-138.

Grandjean, G., J. C. Gourry, and A. Bitri, 2000, Evaluation of GPR techniques for civil-engineering applications: study on a test site: Journal of Applied Geophysics, **45**, 141-156.

Hatch, M., B. Hopkins, and G. White, 2003, Geophysical investigation of River Murray salinity: a case study using fast-sampling TEM: ASEG 16th Geophysical Conference and Exhibition: Australian Society of Exploration Geophysicists.

Hatch, M., B. Barrett, D. Bennetts, G. Heinson, A. Telfer, and C. Roberts, 2002, Improved near surface mapping in groundwater studies: application of fast-sampling time-domain EM surveying methods: Preview, **96**, no. 96, 25-29.

Hatch, M. A., T. J. Munday, and G. Heinson, 2010, A comparative study of in-river geophysical techniques for defining variations in riverbed salt load as an aid to managing river salinization Geophysics, **75**, no. 4, WA135-147.

Hoekstra, P., and A. Delaney, 1974, Dielectric properties of soils at UHF and Microwave frequencies: Journal of Geophysical Research, **79**, no. 11, 1699-1708.

Huang, H., and D. Fraser, 2001, Mapping of the resistivity, susceptibility and permittivity of the earth using a helicopter-borne electromagnetic system: Geophysics, **66**, no. 1, 148-157.

Huang, H., and D. Fraser, 2002, Dielectric permittivity and resistivity mapping using high-frequency helicopter-borne EM data: Geophysics, **67**, no. 3, 727-738.

Hurwitz, S., M. Goldman, M. Ezersky, and H. Gvirtzman, 1999, Geophysical (time domain electromagnetic model) delineation of a shallow brine beneath a freshwater lake, the Sea of Galilee, Israel: Water Resources Research, **35**, no. 12, 3631-3638.

Johnson, D., E. Cherkaev, C. Furse, and A. Tripp, 2001, Cross-borehole delineation of a conductive ore deposit in a resistive host—experimental design: Geophysics, **66**, no. 1, 824-835.

Jol, H. M., D. C. Lawton, and D. G. Smith, 2002, Ground penetrating radar: 2-D and 3-D subsurface imaging of a coastal barrier spit, Long Beach, WA, USA: Geomorphology, **53**, 165-181.

Jones, A. G., 1983, On the equivalence of the "Niblett" and "Bostick" transformations in the magnetotelluric method: Journal of Geophysics, **53**, 72-73.

Jonscher, A. K., 1992, The universal dielectric response and its physical significance: IEEE Transactions on Electrical Insulation, **27**, no. 3, 407-423.

Kalscheuer, T., L. B. Pedersen, and W. Siripunvaraporn, 2008, Radiomagnetotelluric two-dimensional forward and inverse modelling accounting for displacement currents: Geophysics Journal International, **175**, 486-514.

Keller, G. V., 1991, Rock and mineral properties, *in* M. N. Nabighian, ed., Electromagnetic Methods in Applied Geophysics: Society of Exploration Geophysicists, 13-51.

Kelly, B. F. J., D. Allen, K. Ye, and T. Dahlin, 2009, Continuous electrical imaging for mapping aquifer recharge along reaches of the Namoi River in Australia: Near Surface Geophysics, **7**, no. 4, 259-270.

Knight, R. J., and A. Nur, 1987, The dielectric constant of sandstones, 60 kHz to 4 MHz: Geophysics, **52**, no. 5, 644-654.

Lawrie, K., J. Clarke, K. P. Tan, C. Pain, R. Brodie, D. Edwards, H. Apps, V. Wong, and K. Cullen, 2008, An airborne electromagnetic survey used to address salinity and land management issues in the River Murray corridor, SE Australia: 2nd International Salinity Forum, 49-50.

Lazaro-Mancilla, O., and E. Gomez-Trevino, 2000, Ground penetrating radar inversion in 1-D: an approach for the estimation of electrical conductivity, dielectric permittivity and magnetic permeability: Journal of Applied Geophysics, **43**, 199-213.

Loke, M. H., 2001, Electrical imaging surveys for environmental and engineering studies, accessed 23 June 2010; http://www.terrajp.co.jp/lokenote.pdf.

Mahrer, K. D., 1995, Review of the radio frequency (RIM) method and its utilization in near-surface investigations: Leading Edge, **14**, 249-256.

Maxwell, J. C., 1891, A treatise on electricity and magnetism: Dover Publications.

McNeill, J. D., 1980, Technical Note TN-6, Electromagnetic terrain conductivity measurement at low induction numbers, Geonics Limited.

Mellett, J. S., 1995, Ground penetrating radar application in engineering, environmental management, and geology: Journal of Applied Geophysics, **33**, 157-166.

Munday, T. J., I. Overton, and A. Fitzpatrick, 2008, Managing and protecting the local ecology and biodiversity of the Lower Murray River floodplains in SE Australia using biophysical data derived from airborne EM survey data: 2nd International Salinity Forum.

Munday, T. J., A. J. Hill, T. Wilson, B. Hopkins, A. L. Telfer, G. J. White, and A. A. Green, 2005, Combining geology and geophysics to develop a hydrogeologic framework for salt interception in the Loxton Sands Aquifer, central Murray Basin, Australia: Australian Journal of Water Resources, **9**, no. 2, 163-168.

Murray Darling Basin Commission, 2002, Murray-Darling Basin Mapping Basin-in-a-Box Whole of Basin map series, Georeality, CD-ROM.

Murray Darling Basin Commission, 2003, Preliminary investigations into observed river red gum decline along the River Murray below Euston: Technical Report 03/03, Murray Darling Basin Commission.

Nabighian, M. N., and J. C. Macnae, 1991, TEM prospecting methods, *in* M. N. Nabighian, ed., Electromagnetic Methods in Applied Geophysics: Society of Exploration Geophysicists, 427-489.

Nobes, D. C., 1999, The directional dependence of the ground penetrating radar response on the accumulation zones of temperate Alpine glaciers: First Break, **17**, no. 7, 249-258.

Nobes, D. C., R. J. Ferguson, and G. J. Brierley, 2001, Ground-penetrating radar and sedimentological analysis of Holocene floodplains: insight from the Turos valley, New South Wales: Australian Journal of Earth Sciences, **48**, 347-355.

NSW Water Information, 2010, NSW Daily River Reports, http://waterinfo.nsw.gov.au/water.shtml?ppbm=DAILY_REPORTS&dr&3&drkd_url, accessed 23 June 2010.

Olhoeft, G. R., 1979a, Electrical Properties, *in* G. R. Hunt, G. R. Johnson, G. R. Olhoeft, D. E. Watson and K. E. Watson, eds., Initial Report of the Petrophysics Laboratory: U.S. Geological Survey Circular 789, 1-26.

Olhoeft, G. R., 1979b, Tables of room temperature electrical properties for selected rocks and minerals with dielectric permittivity statistics: Open File Report 79-993, U.S. Geological Survey, Denver, CO, USA.

Olhoeft, G. R., 1985, Low-frequency electrical properties: Geophysics, **50**, no. 12, 2492-2503.

Olhoeft, G. R., 1986, Electrical properties from 10^{-3} to 10^{+9} Hz - physics and chemistry: Second International Symposium on the Physics of Porous Media American Institute of Physics, 154.

Olhoeft, G. R., 1998, Electrical, magnetic and geometric properties that determine ground penetrating radar performance: Proceedings of the Seventh International Conference on Ground Penetrating Radar, 1-4.

Overton, I. C., I. D. Jolly, P. G. Slavich, M. M. Lewis, and G. R. Walker, 2006, Modelling vegetation health from the interaction of saline groundwater and flooding on the Chowilla floodplain, South Australia: Australian Journal of Botany, **54**, 207-220.

Paine, J. G., E. W. Collins, H. S. Nance, and K. L. Neimann, 2006, Streambed induction logs: An airborne approach to identifying salinity sources and quantifying salinity loads: Symposium on the Application of Geophysics to Engineering and Environmental Problems 2006: The Environmental and Engineering Geophysics Society, Extended Abstracts, 96-104.

Paine, J. G., E. W. Collins, H. S. Nance, and K. L. Niemann, 2009, Combining airborne electromagnetic induction and hydrochemistry to quantify salinity contributions to a large basin stream, Colorado River, Texas, USA: Near Surface Geophysics, **7**, no. 4, 271-282.

Paterson, N. R., and V. Ronka, 1971, Five years of surveying with the very low frequency-electro magnetics method: Geoexploration, **9**, 7-26.

Pellerin, L., V. Labson, and M. C. Pfeifer, 1995, VETEM - A very early time electromagnetic system - the first year: Proceedings of the Symposium on the Application of Geophysics to Engineering and Environmental Problems: The Environmental and Engineering Geophysics Society, Extended Abstracts.

Pelton, W. H., S. H. Ward, P. G. Hallof, W. R. Sill, and P. H. Nelson, 1978, Mineral discrimination and removal of inductive coupling with multifrequency IP: Geophysics, **43**, no. 3, 588-609.

Poley, J. P., J. J. Nooteboom, and P. J. de Waal, 1978, Use of v.h.f. dielectric measurements for borehole formation analysis: Log Analyst, **19**, 18-30.

Reid, J., A. Fitzpatrick, and K. Godber, 2010, An overview of the SkyTEM airborne EM system with Australian examples: Preview, no. 145, 26-37.

Reid, J. E., and A. Howlett, 2001, Application of the EM-31 terrain conductivity meter in highly-conductive regimes: Exploration Geophysics, **32**, no. 4, 219-224.

Reynolds, J. M., 1997, An introduction to applied and environmental geophysics: John Wiley and Sons Ltd.

Robert, A., 1998, Dielectric permittivity of concrete between 50 Mhz and 1 Ghz and GPR measurements for building materials evaluation: Journal of Applied Geophysics, **40**, 89-94.

Roy, A., and A. Apparao, 1971, Depth of investigation in direct current methods: Geophysics, **36**, no. 5, 610-625.

Santamarina, J. C., V. A. Rinaldi, D. Fratta, and K. A. Klein, 2005, A survey of elastic and electromagnetic properties of near-surface soils, *in* D. Butler, ed., Near-Surface

Geophysics, Volume 1: Concepts and Fundamentals: Society of Exploration Geophysicists, 71- 87.

Sassen, D. S., M. E. Evertt, and C. L. Munster, 2009, Ecohydrogeophysics at the Edwards Aquifer: insights from polarimetric ground-penetrating radar: Near Surface Geophysics, **7**, 427-438.

Schaetzl, R., and S. Anderson, 2005, Soils: genesis and geomorphology: Cambridge University Press.

Scharma, P. V., 1997, Environmental and Engineering Geophysics: Cambridge University Press.

Seyfried, M. S., and M. D. Murdock, 2004, Measurement of soil water content with a 50-MHz dielectric sensor: Soil Science Society of America Journal, **68**, 394-403.

Sheriff, R. E., 2002, Encyclopedic Dictionary of Applied Geophysics: Society of Exploration Geophysicists.

Siemon, B., A. V. Christiansen, and E. Auken, 2009, A review of helicopter-borne electromagnetic methods for groundwater exploration: Near Surface Geophysics, **7**, no. 5-6, 629-646.

Smith-Rose, R. L., 1933, The electrical properties of soil for alternating currents at radio frequencies: Proceedings of the Royal Society of London. Series A, Containing Papers of a Mathematical and Physical Character, **140**, no. 841, 359-377.

Snyder, D. D., S. MacInnes, M. J. Raymond, and K. L. Zonge, 2002, Continuous resistivity profiling in shallow marine and fresh water environments: Symposium on the Application of Geophysics to Engineering and Environmental Problems 2002: The Environmental and Engineering Geophysics Society, Extended Abstracts, GSL4-GSL4.

Sørensen, K. I., E. Auken, N. B. Christensen, and L. Pellerin, 2005, An integrated approach for hydrogeological investigations: New technology and a case history, *in* D. Butler, ed., Near-Surface Geophysics, Volume 2: Applications and Case Histories: Society of Exploration Geophysicists, 71- 87.

Spies, B. R., 1989, Depth of investigation in electromagnetic sounding methods: Geophysics, **54**, no. 7, 872-888.

Spies, B. R., and D. E. Eggers, 1986, The use and misuse of apparent resistivity in electromagnetic methods: Geophysics, **51**, no. 7, 1462-1471, accessed 23 June 2010; http://link.aip.org/link/?GPY/51/1462/1.

Spies, B. R., and P. Woodgate, 2004, Technical Report: Salinity mapping methods in the Australian context, Programs Committee of the Natural Resource Management Ministerial Council, accessed 23 June 2010; http://lwa.gov.au/products/er040732.

Stewart, D. C., W. L. Anderson, T. P. Grover, and V. F. Labson, 1994, Shallow subsurface mapping by electromagnetic sounding in the 300 kHz to 30 MHz range: Model studies and prototype system assessment: Geophysics, **59**, no. 8, 1201-1210.

Stolarczyk, L., G. Rogers, and P. Hatherly, 1988, Comparison of radio imaging method (RIM) electromagnetic wave tomography with in-mine geological mapping in the Liddel, Bulli and Wongawilli coal seams: Australian Society of Exploration Geophysicists / Society of Exploration Geophysicists Conference: Australian Society of Exploration Geophysicists, Extended Abstracts.

Stratton, J. A., 1941, Electromagnetic theory: McGraw-Hill Book Co.

Tallini, M., D. Gasbarri, D. Ranalli, and M. Scozzafava, 2006, Investigating epikarst using low-frequency GPR: example from the Gran Sasso range (Central Italy): Bulletin of Engineering Geology and the Environment, **65**, 435-443.

Tan, K. P., V. Berens, M. Hatch, and K. Lawrie, 2007, Determining the suitability of In-Stream NanoTEM for delineating zones of salt accession to the River Murray: A review of survey results from Loxton, South Australia: Cooperative Research Centre for Landscape Environments and Mineral Exploration Open File Report 192, Cooperative Research Centre for Landscape Environments and Mineral Exploration, accessed 23 June 2010; http://crcleme.org.au/Pubs/OPEN%20FILE%20REPORTS/OFR%20192/OFR%20192.pdf .

Taner, M. T., F. Koehler, and R. E. Sheriff, 1979, Complex seismic trace analysis: Geophysics, **44**, no. 6, 1041-1063.

Taurisano, A., S. Tronstad, O. Brandt, and J. Kohler, 2006, On the use of ground penetrating radar for detecting and reducing crevasse-hazard in Droning Maud Land, Antarctica: Cold Regions Science and Technology, **45**, 166-177.

Telfer, A., V. Berens, M. Hatch, and C. Palfreyman, 2005, Instream NanoTEM: providing increased resolution to stream salinisation and floodplain processes along the River Murray, southeast Australia: Australian Journal of Water Resources, **9**, no. 2, 155-161.

Telfer, A. L., M. Hatch, C. Palfreyman, and V. Berens, 2004, Instream NanoTEM survey of the River Murray 2004: Blanchetown to Mallee Cliffs: AWE 42417B, Murray River Darling Basin Commission and Mallee Catchment Management Authority.

Telford, W. M., L. P. Geldart, R. E. Sheriff, and D. A. Keys, 1976, Applied Geophysics: Cambridge University Press.

Thomson, S., J. Young, and N. Sheard, 1992, Base metal applications of the radio imaging method. Current status and case studies: Exploration Geophysics, **23**, 367-372.

Thorne, R., G. Hoxley, and H. Chaplin, 1990, Nyah to the South Australian border hydrogeological project.

Tsoflias, G. P., and M. W. Becker, 2008, Ground-penetrating-radar response to fracture-fluid salinity: Why lower frequencies are favorable for resolving salinity changes: Geophysics, **73**, no. 5, J25-J30.

Victorian Water Resources Data Warehouse, 2011a, Bore B136355, http://www.vicwaterdata.net/vicwaterdata/data_warehouse_content.aspx?option=4&url=DNRE&sitecode=B136355, accessed 27 October, 2011.

Victorian Water Resources Data Warehouse, 2011b, Bore B7928, http://www.vicwaterdata.net/vicwaterdata/data_house_content.aspx?option=4&url=DNRE&sitecode=B7928, accessed 27 October, 2011.

Viezzoli, A., E. Auken, and T. Munday, 2009, Spatially constrained inversion for quasi 3D modelling of airborne electromagnetic data - an application for environmental assessment in the Lower Murray Region of South Australia: Exploration Geophysics, **40**, no. 2, 173-183.

Viezzoli, A., A. V. Christiansen, E. Auken, and K. I. Sørensen, 2008, Quasi-3D modeling of airborne TEM data by spatially constrained inversion: Geophysics, **73**, no. 3, F105-F113.

Viezzoli, A., T. Munday, E. Auken, and A. V. Christiansen, 2010, Accurate quasi 3D versus practical full 3D inversion of AEM data - the Bookpurnong case study: Preview, **149**, 23-31.

von Hippel, A. R., 1954, Dielectrics Materials and Applications: MIT Press.

Vrbancich, J., M. Hallett, and G. Hodges, 2000, Airborne electromagnetic bathymetry of Sydney Harbour: Exploration Geophysics, **31**, 179-186.

Wagner, K. W., 1914, Erklarung der dielecktrischen Nachwirkungsworgange auf Grund Maxwellscher vorstellungen: Archiv. Eleckrotechnik, **2**, 371.

Ward, S. H., 1967, Electromagnetic theory for geophysical applications, *in* D. A. Hansen, W. E. Heinrichs, R. C. Holmer, R. E. MacDougal, G. R. Rogers, J. S. Dumner and S. H. Ward, eds., Mining Geophysics, Vol. 2: Society of Exploration Geophysicists, 10-196.

Ward, S. H., and G. W. Hohmann, 1991, Electromagnetic theory for geophysical applications, *in* M. N. Nabighian, ed., Electromagnetic Methods in Applied Geophysics: Society of Exploration Geophysicists, 131-311.

Wensink, W. A., 1993, Dielectric properties of wet soils in the frequency range 1-3000MHz: Geophysical Prospecting, **41**, 671-696.

White, R. E., 1991, Properties of instantaneous seismic attributes: Leading Edge, **10**, no. 7, 26-32.

Wozencraft, J. M., and W. J. Lilycrop, 2002, Total shallow-water survey through airborne hydrography, Joint Airborne Lidar Bathymetry Technical Center of Expertise, US Army Corps of Engineers.

Yin, C., and G. Hodges, 2005, Influence of displacement currents on the response of helicopter electromagnetic systems: Geophysics, **70**, no. 4, G95-G100 http://link.aip.org/link/?GPY/70/G95/1.

Zeng, Z., L. Huang, S. Liu, F. Liu, and J. Sun, 2008, The very low-frequency step-frequency GPR system and its application to active fault detection: Near Surface Geophysics, **6**, 167-172.